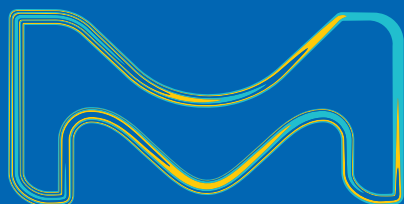


# Material Matters™

VOLUME 14 • NUMBER 3



## Advanced Tools for Drug Delivery Research

MICROFLUIDIC-ASSISTED  
MANUFACTURING of materials for  
nanomedicine

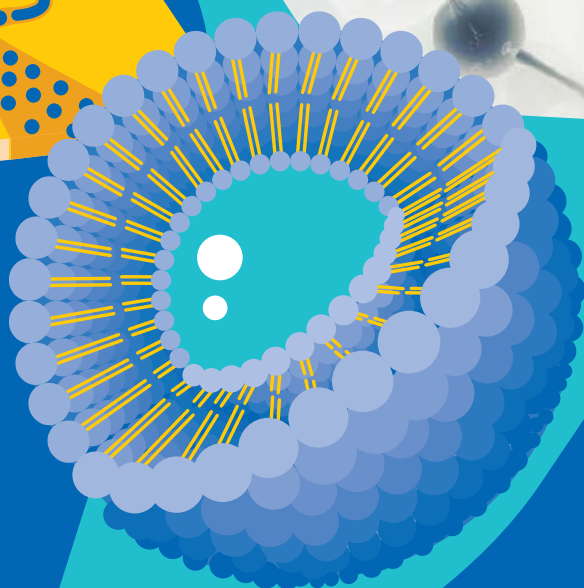
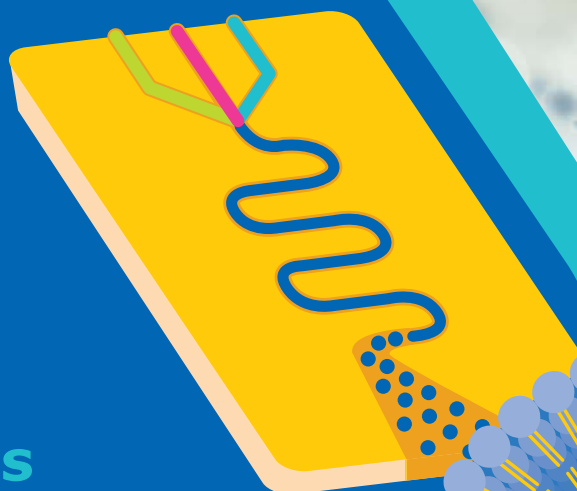
THREE-DIMENSIONAL BIOPRINTING for  
Tissue and Disease Modeling

NANOPARTICLE-BASED DRUG AND GENE  
DELIVERY for Tumor Targeting

SMART OLIGONUCLEOTIDE DELIVERY by  
Multifunctional Block Copolymers

APPLICATIONS OF GLUCOSE POLYMERS in  
the Synthesis of Diagnostic and Drug  
Delivery Nanoparticles

The life science business of Merck KGaA,  
Darmstadt, Germany operates as  
MilliporeSigma in the U.S. and Canada.



## Introduction



**Hanying Luo, Ph.D.**  
Global Product  
Manager –  
Biomedical Materials

Welcome to the third issue of *Material Matters*™ for 2019, focusing on novel materials and techniques for facilitating the development of drug delivery systems and *in vitro* drug testing. This issue highlights the advancements in materials and nanoformulation approaches to address the challenges in nano drug delivery research.

Nanoparticle-based drug delivery systems have shown significant promise for the delivery of therapeutic agents to specific sites in a controlled manner; however, the reproducible formulation of nano-encapsulated therapeutics remains a challenge. In our first article, Professor **Nicola Tirelli (Istituto Italiano di Tecnologia, Italy)** highlights the microfluidic-assisted method for fabricating well-defined and reproducible nanoparticles for drug delivery research.

In the second article, Professor **Shrike Zhang (Harvard Medical School, USA)** discusses advances in 3D-bioprinted tissue models for *in vitro* drug testing, reviews bioink selections, and provides application examples of 3D bioprinting in tissue model biofabrication.

Nanoparticles have been investigated as tumor-targeting drug delivery systems utilizing the enhanced permeability and retention (EPR) effect. In the third article, Professor **Yoshiki Katayama (Kyushu University, Japan)** discusses recent advances in drug delivery systems and strategies that exploit the EPR effect, with a special focus on stimuli-responsive systems based on novel materials.

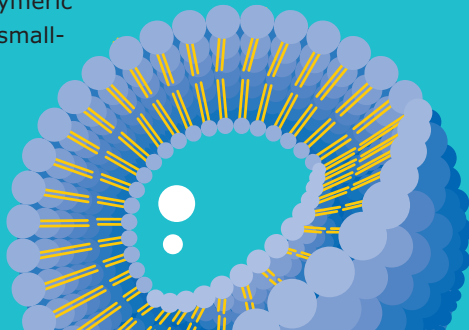
Cationic polymers readily form complexes with nucleic acids and are the most widely used non-viral gene delivery vectors. In the fourth article, **Kanjiro Miyata (The University of Tokyo, Japan)** provides insights on the rational design of polymeric materials for “smart” oligonucleotide delivery.

In the fifth article, **Dmitri Simberg (University of Colorado Anschutz Medical Campus, USA)** reviews the use of dextran and cyclodextrin for the synthesis of nanoparticles used in drug delivery applications. The review examines the role of dextran in forming nanoparticles with doxorubicin and in the formation and stability of iron oxide nanoparticles, as well as cyclodextrin as a starting material for nanoparticle synthesis.

In this issue, each article is accompanied by a list of polymers and related products available from the Sigma-Aldrich portfolio available from MilliporeSigma/Merck. Please visit [SigmaAldrich.com/matsci](https://www.sigmaaldrich.com/matsci) for additional product offerings and information. As always, please do “bother” us with new product suggestions and your feedback at [SigmaAldrich.com/technicalservice](https://www.sigmaaldrich.com/technicalservice).

### About the Cover

Nanoparticle drug delivery systems are emerging as a useful tool for achieving controlled and targeted delivery of drug molecules and thereby enhancing therapeutic effect. The cover art for this issue depicts microfluidic-assisted nanoformulation, one method for fabricating liposomes and polymeric nanoparticles for the delivery of small-molecule and biological drugs.



Merck KGaA, Darmstadt, Germany  
Frankfurter Strasse 250  
64293 Darmstadt, Germany  
Phone +49 6151 72 0

#### To Place Orders / Customer Service

Contact your local office or visit  
[SigmaAldrich.com/order](https://www.sigmaaldrich.com/order)

#### Technical Service

Contact your local office or visit  
[SigmaAldrich.com/techinfo](https://www.sigmaaldrich.com/techinfo)

#### General Correspondence

Materials Science  
[materialsscience@sial.com](mailto:materialsscience@sial.com)

#### Subscriptions

Request your FREE subscription to *Material Matters*™ at [SigmaAldrich.com/mm](https://www.sigmaaldrich.com/mm)

The entire *Material Matters*™ archive is available at [SigmaAldrich.com/mm](https://www.sigmaaldrich.com/mm)

*Material Matters*™ (ISSN 1933-9631) is a publication of Merck KGaA, Darmstadt, Germany

Copyright © 2019 Merck KGaA, Darmstadt, Germany and/or its affiliates. All rights reserved. MilliporeSigma, the vibrant M, Sigma-Aldrich and Material Matters are trademarks of Merck KGaA, Darmstadt, Germany or its affiliates. All other trademarks are the property of their respective owners. Detailed information on trademarks is available via publicly accessible resources. More information on our branded products and services on [MilliporeSigma.com](https://www.milliporesigma.com)

## Table of Contents

### Articles

Microfluidic-Assisted Manufacturing of Materials for Nanomedicine	83
Three-Dimensional Bioprinting for Tissue and Disease Modeling	93
Nanoparticle-Based Drug and Gene Delivery for Tumor Targeting	102
Smart Oligonucleotide Delivery by Multifunctional Block Copolymers	110
Applications of Glucose Polymers in the Synthesis of Diagnostic and Drug Delivery Nanoparticles	117

### Featured Products

Biodegradable Polymers A selection of Poly(lactide), Poly(lactide-co-glycolide), Poly(L-lactide-co-D,L-lactide), and Poly(L-lactide-co-ε-caprolactone)	90
Biodegradable Diblock Copolymers A selection of PEG-block-co-polymers	90
Functionalized Biodegradable Diblock Copolymers A selection of PEG-block-poly(caprolactone)	91
Chitosan A list of chitosan materials for nanomedicine	91
Bioinks A selection of bioinks and bioink precursors for 3D bioprinting	100
Natural Polymers for 3D Bioprinting A selection of functionalized gelatin, gelatin, and collagen	100
Synthetic Polymers for 3D Bioprinting A selection of Poly(hydroxyethyl methacrylate) and PEG	101
Polyethyleneimine A selection of branched, linear, and PEI derivatives	108
Poly(ethylene glycol) A selection of functionalized PEGs	115
Building Blocks for Poly(L-lysine) Modification A selection of building blocks for PLL	116
Glucose Polymers A selection of Dextran, Maltodextrin, and β-Cyclodextrin Polymers	121
Building Blocks A selection of building blocks for drug delivery	121

## Your Material Matters



*Bryce P. Nelson*

Bryce P. Nelson, Ph.D.  
Materials Science Initiative Lead

We welcome fresh product ideas. Do you have a material or compound you wish to see featured in our Materials Science line? If it is needed to accelerate your research, it matters. Send your suggestion to [matsci@sial.com](mailto:matsci@sial.com) for consideration.

Professor Jeffrey Bode at ETH-Zürich recommended the addition of potassium acyltrifluoroborate functionalized poly(ethylene glycol)s (PEG KATs) (Cat. Nos. **901645**, **901644**, **901641**, **901635**, and **901637**) to our catalog for protein modification and conjugation.

PEGylation of therapeutic proteins offers advantages for extending *in-vivo* half-life and improving protein solubility. Scientists currently rely heavily on a few conjugation techniques for PEGylation, including the modification of cysteine residues and non-specific attachment to lysines. The potassium acyltrifluoroborate (KAT) functional group enables an alternative protein conjugation strategy that operates at low concentrations in aqueous buffers.<sup>1,2</sup> PEGylation of peptides and proteins using PEG-KATs occurs in a chemoselective fashion in the presence of unprotected amino acid side chains, in which hydroxyamines undergo rapid amide-forming ligations with KATs and result in rapid PEG conjugation.<sup>3-5</sup> In addition to protein modification, bi- and tetra-functional PEG KATs are readily used in the preparation of biocompatible hydrogels.<sup>6-8</sup> Novel PEG-based hydrogels can be prepared via chemoselective amide ligation using a 4-arm PEG-KAT reagent (Cat. No. **901637**), and the resulting gels are suitable for the encapsulation of cells with high viability, demonstrating the biocompatibility of the KAT ligation.<sup>7</sup>

### References

- (1) Dumas, A. M.; Bode, J. W. *Org. Lett.* **2012**, *14*, 2138-2141.
- (2) Dumas, A. M.; Molander, G. A.; Bode, J. W. *Angew. Chem. Int. Ed.* **2012**, *51*, 5683-5686.
- (3) Noda, H.; Erős, G.; Bode, J. W. *J. Am. Chem. Soc.* **2014**, *136*, 5611-5614.
- (4) White, C. J.; Bode, J. W. *ACS Cent. Sci.* **2018**, *4*, 197-206.
- (5) Boross, G. N.; Schauenburg, D.; Bode, J. W. *Helv. Chim. Acta* **2018**, *10.1002/hlca.201800214*.
- (6) Gu, Y.; Schauenburg, D.; Bode, J. W.; Johnson, J. A. *J. Am. Chem. Soc.* **2018**, *140*, 14033-14037.
- (7) Mazunin, D.; Broguiere, N.; Zenobi-Wong, M.; Bode, J. W. *ACS Biomater. Sci. Eng.* **2015**, *1*, 456-462.
- (8) Schauenburg, D.; Osuna Gálvez, A.; Bode, J. W. *J. Mater. Chem. B* **2018**, *6*, 4775-4782.

Name	PEG Average M <sub>n</sub>	Cat. No.
Methoxy poly(ethylene glycol) KAT	5,000	<b>901644-500MG</b>
	10,000	<b>901642-500MG</b>
	20,000	<b>901645-500MG</b>
4-arm-PEG10K-KAT	10,000	<b>901637-500MG</b>
Poly(ethylene glycol) bis (2-pyridyl) KAT	10,000	<b>901635-500MG</b>

# IMPROVE DELIVERY

## A Step-by-Step Guide

Low drug solubility and stability often reduce the effectiveness of an otherwise promising therapeutic candidate. In this comprehensive guide, you'll discover how polymers can provide the drug delivery solutions you need for controlled release, targeting, and solubility enhancement.

Request your copy online at:

[SigmaAldrich.com/ddtechnique](http://SigmaAldrich.com/ddtechnique)

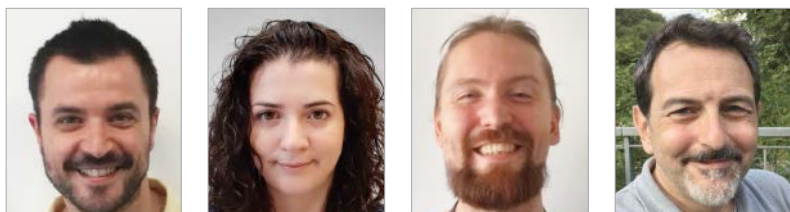


The life science business of Merck KGaA, Darmstadt, Germany operates as MilliporeSigma in the U.S. and Canada.

**Sigma-Aldrich®**  
Lab & Production Materials



# Microfluidic-Assisted Manufacturing of Materials for Nanomedicine



Mike Geven,<sup>1</sup> Nora Francini,<sup>1</sup> Roberto Donno,<sup>1</sup> Nicola Tirelli<sup>1,2\*</sup>

<sup>1</sup>Laboratory of Polymers and Biomaterials, Fondazione Istituto Italiano di Tecnologia, 16163, Genova, Italy.

<sup>2</sup>Division of Pharmacy and Optometry, School of Health Sciences, Faculty of Biology, Medicine and Health, The University of Manchester, M13 9PT, Manchester, UK.

\*Email: Nicola.tirelli@iit.it

## Introduction

This paper is about various preparative processes for nanomaterials designed to carry and deliver drugs, known as nanocarriers. Nanocarriers can affect both the pharmacokinetics (biodistribution, elimination, metabolism) and the pharmacodynamics (interactions with biological targets) of a drug, allowing to a) increase its dose well above its water solubility, b) change its concentration in body compartments, possibly and preferentially addressing it to target organs, c) reduce its elimination rate and protect it from degradation [pharmacokinetic factors], d) present it to cells and/or e) deliver it to cell compartments in a more efficacious fashion [pharmacodynamic factors]. Thanks to the potential access to a broader therapeutic spectrum, a number of nanomedicine-based formulations are now in clinical use (**Table 1**), having been approved by the United States Food and Drug Administration (FDA) and the European Medicines Agency (EMA). On the other hand, the development of nanomedicine has significant hurdles to overcome, most importantly in the precise description and reproducibility of both physico-chemical (preparative processes) and biological (therapeutic performance) aspects. This is due to most nanomedicines not being 'molecularly defined': they comprise different chemical species, often with multiple phase boundaries, making classical molecular analysis not applicable. For example, the very concept of molarity (or molecular weight) is not applicable to nanoparticles.

As a practical example of the hurdles encountered in nanomedicine development, we can consider what it takes to evaluate a 'nanosimilar' (the generic equivalent of a nanomedicine);<sup>1</sup> its therapeutic equivalence to a pre-existing nanomedicine can be expected only having established a) its pharmaceutical equivalence, i.e. the new product has similar physico-chemical descriptors, typically referred to as critical quality attributes (CQAs), and b) its bioequivalence, i.e. the active principle is made available at the same rate and same extent in the same sites. However, failure in (a) (=poorly reproducible CQAs) implies failure in (b) (=poorly reproducible pharmacokinetics), and therefore precisely described and reproducible CQAs are a necessary requisite for therapeutic efficacy. Of note, they are necessary but not sufficient; for example, poor bioequivalence may occur also when pharmaceutical equivalence appears to be achieved (see the generic PEGylated liposomal Lipodox compared to Doxil<sup>2</sup>).

For nanomedicines, the most important CQAs are size and size distribution, in addition to the often related parameters of surface charge and drug loading;<sup>3</sup> this is not surprising since size (number), size distribution, and surface area are considered the critical descriptors of a nanomaterial, as per its EU commission definition.<sup>4</sup> The first target of any pharmaceutical nanomanufacturing process is therefore to precisely and reproducibly control the size/size distribution of the nanomedicines.

**Table 1.** EMA- and FDA-approved nanomedicines.<sup>a</sup>

	Active princ.; brand name	Material	Therapeutic indications	EMA	FDA
Nanoparticles	<i>Nab-paclitaxel</i> ; Abraxane®	Albumin	Breast, non-small-cell lung, and pancreatic c.	2008	2005
	<i>Glatiramer acetate</i> ; Copaxone®, Synthon®	Poly(amino acid)	Multiple sclerosis	2017	1996
	<i>Leuprolide acetate</i> ; Eligard®	PLGA	Prostate c.	=	2002
	<i>Denileukin diftitox</i> Ontak®	Interleukin-2 + diphth. toxin	T-cell lymphoma	=	1999
	<i>Ferumoxytol</i> ; Rienso®, Feraheme®	Iron oxide/dextran	Iron def. anemia in chronic kidney disease	2012 <sup>b</sup>	2009
	<i>Ferric carboxymaltose</i> ; Ferinject®, Injectafer®	Iron oxide/carboxymaltose	Iron deficiency	2007	2012
	<i>Iron(III) isomaltoside</i> Monofer®	Iron(III)isomaltoside-1000	Iron deficiency	2009	2009
Liposomes	<i>Doxorub. hydrochl.</i> ; Caelyx®, Doxil®	PEGylated lipos.	Breast, ovar c., mult. myel., Kaposi's sarc.	1996	1995
	<i>Doxorub. hydrochl.</i> ; Myocet®	Non-PEGylated lipos.	Metast. breast c.	2000	
	<i>Amphoter. B</i> ; AmBisome®	Non-PEGylated lipos.	Fungal infection	2006	1997
	<i>Daunorubicin</i> ; DaunoXome®	Non-PEGylated lipos.	Adv. HIV-rel. Kaposi's sarc.	2012	1996
	<i>Cytarabine</i> ; DepoCyte®	Non-PEGylated lipos.	Lymphom. mening.	2001	1996
	<i>Mifamurtide</i> ; Mepact®	Non-PEGylated lipos.	Osteosarcoma	2009	=
	<i>Morphine</i> ; DepoDur®	Non-PEGylated lipos.	Pain	2006	2004
	<i>Vincristine</i> ; Marqibo®	Non-PEGylated lipos.	Ac. Lymphoc. blood clots	=	2012
	<i>Irinotecan</i> ; Onivyde®	PEGylated lipos.	Pancreatic c.	=	2015
	<i>AmphotericinB</i> ; Abelcet®	Non-PEGylated lipos.	Fungal infection	=	1995
	<i>Poractantalpha</i> ; Curosurf®	Non-PEGylated lipos.	Stress disorders	=	1999
	<i>Verteporfin</i> ; Visudyne®	Liposomal porphyrin	Age-related mac. degen.	2000	2000
	Emuls.	<i>Cyclosporine</i> Sandimmun Neoral®	Glycerides/triglycerides	Organ transpl., endog. uveitis, nephrot. syndr., rh. arthr., psoriasis, atopic derm.	1993 <sup>b</sup>
<i>Estradiol</i> ; Estrasorb®		Soybean oil/surfactants	Menopause	=	2003
Nanocryst.	Xeplion®, Invega Sustenna®	Paliperidone palmitate	Schizophrenia	2011	2009
	Zypadhera®	Olanzapine pamoate	Schizophrenia	2008	=
	<i>Aprepitant</i> ; Emend®	Aprepitant	Nausea and vomiting	2003	2003
	<i>Fenofibrate</i> ; Tricor® Lipanthyl® Lipidil®	Fenofibrate	Hyperlipidemia	1977 <sup>b</sup>	2004
	<i>Sirolimus</i> ; Rapamune®	Sirolimus	Graft rej., kidn. transp.	2001	1999

<sup>a</sup> In this table we do not report nanomedicines of a molecular nature, such as protein/polymer conjugates. This group of nanomedicines is predominantly comprised of PEGylated proteins (PegIntron®, Pegasys®, Neulasta®, Oncaspar®, Mircera®, Cimzia®, Somavert®, Adagen®, Macugen®, Krystexxa®, Plegridy®, Adynovate®) and also Zevalin® (a radionuclide-conjugated antibody). They differ from those reported in the table because they are well-defined individual molecular entities in solution, where those reported are multi-molecular (e.g. drug and coating agent in nanocrystals) and multi-phase (e.g. oil and water in emulsions) formulations.

<sup>b</sup> Ferumoxytol – currently withdrawn. Sandimmun Neoral – date of the registration in Germany. Fenofibrate – date of first commercialization.

## Nanoparticle Manufacturing

Herein we discuss nanomanufacturing in aqueous dispersion, specifically focusing on the bottom-up (through aggregation or agglomeration) production of nanoparticles; with this word we refer to nanomaterials with a predominantly elastic mechanical behaviour (solid-like, thereby including nanocrystals in this class), as opposed to nanodroplets, emulsions, self-assembled aggregates (micelles, vesicles) etc. that are mostly viscous in nature. From a processing point of view, this separation

is important because the slow/arrested dynamics of elastic materials (high Deborah numbers) means that their morphology, size, and composition, i.e. their CQAs most often end up being determined by kinetic factors such as how the precursors are mixed (the fluidodynamics of the system), rather than thermodynamics. In view of the criticality of kinetic factors, flow-based and in particular, microfluidic-assisted processes have specific advantages, but also some important caveats.

## Flow vs Batch Nanomanufacturing Processes

Pioneered in the late 2000s,<sup>5</sup> flow-based processes have become increasingly popular to produce formulations for drug delivery. Largely irrespective of the nature of the process, continuous flow conditions offer clear advantages over traditional batch processes: a) easy scalability; the quantity of product scales directly with time, but does not require different reactors; b) reproducibility; fixed geometries allow for a precise control of mixing conditions, which in turn provides particles with a lower size dispersity,<sup>6</sup> and sometimes also a better drug loading;<sup>7</sup> c) fine tuning of particle properties (size) through process parameters such as the flow regimen, which allows for tailor-made materials.<sup>5</sup>

Due to the small channel dimensions (< 1 mm), microfluidic set-ups allow evaluation and optimization of the conditions for continuous flow processes, to embed advanced quality control tools (e.g. in-line dynamic light scattering (DLS) or off-line field flow fractionation (FFF)<sup>6</sup>), at a lab scale and at very reasonable cost; they can also be used for scaled-up productions, although the real industrial scalability requires careful considerations about the nature, dimensions, and production costs of the appropriate chips.<sup>8</sup>

### The Problem of Mixing

Microfluidic-assisted nanomanufacturing also has an important trait: the small lateral dimension of the channels causes the flow to be essentially laminar. In quantitative terms, at a constant flow rate the Reynolds number ( $Re = \frac{Vd}{\nu}$ ; where  $V$  is the flow rate,  $d$  the diameter of the channel,  $\rho$  the density of the fluid,  $\nu$  its viscosity) scales with  $d^1$ ,  $Re$  almost inevitably assumes values orders of magnitude lower than the minimum necessary to achieve turbulence ( $Re \gg 10^3$ ).  $Re$  cannot be boosted by a large increase in flow rate, because this would significantly increase the driving pressure, which scales both with  $V$  and  $d^2$ .

This leads to the problem. With no lateral convection in a laminar flow, mixing is only based on diffusion, with mixing times typically scaling as  $\tau_{mix} \sim d^2/D$  ( $d$  is the width of the fluid stream;  $D$  is the diffusion coefficient, inversely related to size, **Figure 1**). In short, the mixing is slow, especially for polymers. For example, a 1 kDa poly(ethylene glycol) (PEG) ( $D \sim 3 \times 10^{-10} m^2/s$ ) (solution in water would cover 100  $\mu m$  in 30 seconds. In order to achieve mixing at 1 mL/min, a capillary would need to be at least 15 cm long.

The slow mixing is often a problem because it may lead to less desired but more thermodynamically stable products; e.g. microparticles (lower interfacial energy) instead of nanoparticles as a result of a slower precipitation process.

### Laminar flow: Mixing only via lateral diffusion

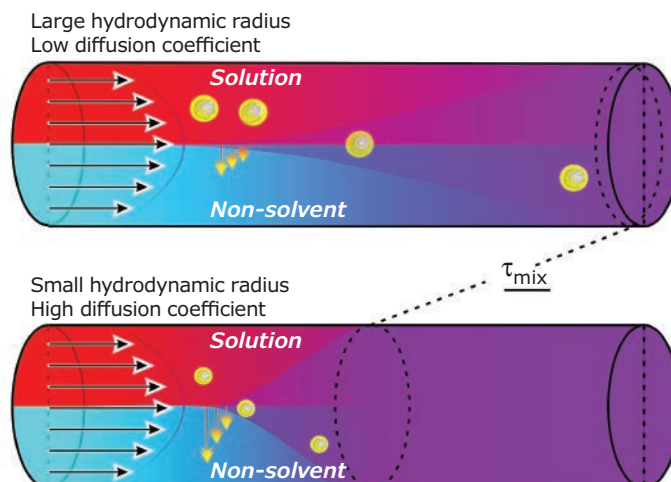


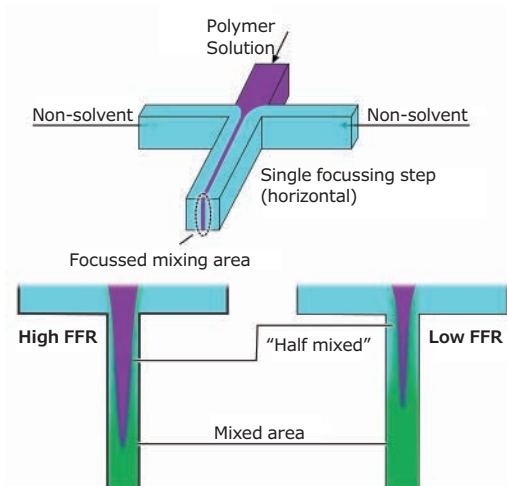
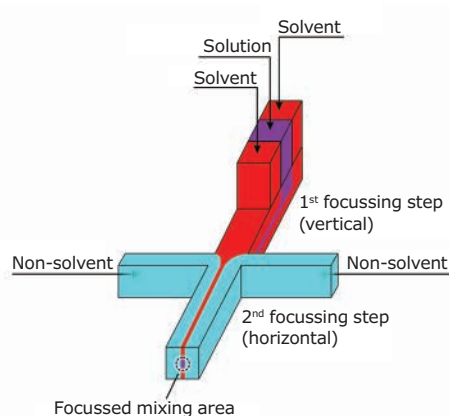
**Figure 1.** Two fluids moving parallel in a laminar flow mix laterally only through diffusion, which is increasingly slow as the size of the object increases.

### Solutions Developed to Accelerate Mixing

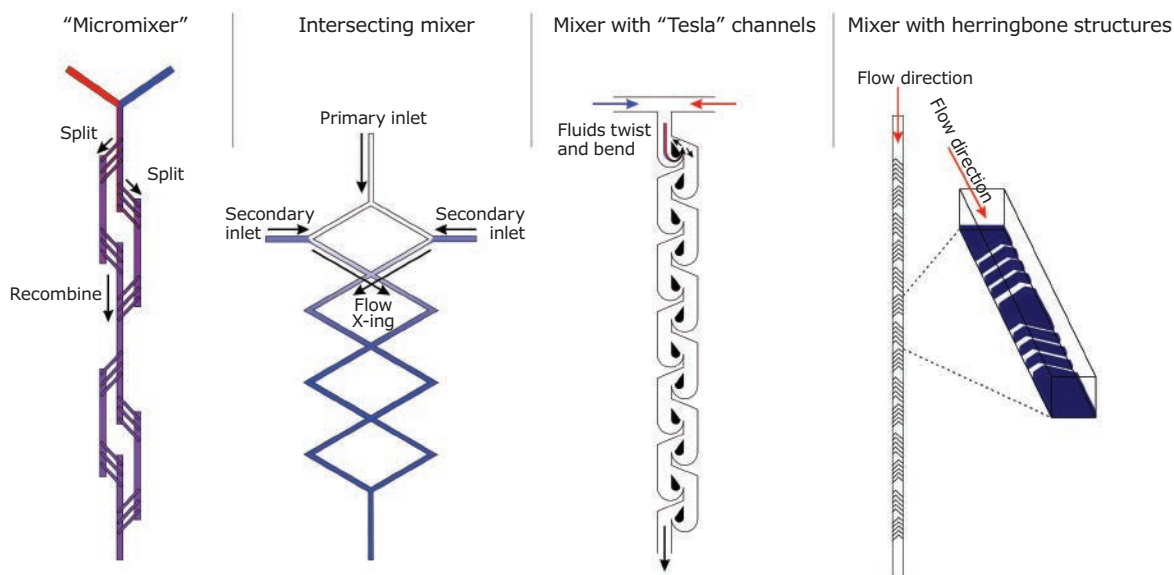
Often solvents and materials are selected to maximize reciprocal diffusion coefficients and often to minimize viscosity. More commonly, the geometrical features and/or the nature of the flow are engineered either acting on the area where the different fluids meet (the confluence point), or on the area immediately after (the mixing region of the chip). An example of the former approach is hydrodynamic flow focusing (HFF), which is based on the control over the width of a central flow that carries the material of interest and is squeezed by lateral flows (**Figure 2, left**).

For the latter approach, the general aim is to transition from a laminar to a chaotic flow regimen. Although curvilinear channels can already provide some results, static or 'passive' (micro)mixers<sup>10</sup> (**Figure 3**) typically have paths with complex shapes and obstacles. The chaotic character of the flow can be further increased with heterogeneities in the flow itself, e.g. with small amounts of high molecular weight polymers that alter viscosity at a microscopic level,<sup>9</sup> or through the use of patterned surfaces.<sup>11</sup> The mixing efficiency of static mixers is typically compared through the Peclet number ( $Pe$  is the length of the channel), which actually provides the ratio between mass transport through convection (chaotic flow), and that due to diffusion (laminar flow).

More complex approaches are based on 'active' mixers, where chaotic features are introduced via external fields through e.g. cavitation.<sup>12</sup>

**HFF: Hydrodynamic Flow Focusing****3D HFF**

**Figure 2.** In 2D HFF, two lateral flows squeeze a central polymer solution increasingly with their relative speed (flow rate ratio). The polymer solution spans through the height of the channel until fully mixed, but in the 3D version (right) further focusing confines it centrally.

**Towards chaotic flow: Passive mixers**

**Figure 3.** Schematic structures of the most common passive mixers. The general aim is the creation of vortices, twists, or transversal flows in order to facilitate mixing orthogonal to the flow direction. Since these structures are introduced after the junction zone, these approaches are compatible with HFF.



## Examples of Microfluidic-Assisted Nanomanufacturing

### Nanomanufacturing Via Phase Separation

The gold standard materials are hydrophobic polyesters such as poly(lactic-co-glycolic acid) (PLGA) or poly( $\epsilon$ -caprolactone) (PCL), either combined with surfactants or blocks of macroamphiphiles (amphiphilic block copolymers) containing PEG as hydrophilic component (Table 2, top section). Of note, macroamphiphiles can yield smaller colloids than hydrophobe/surfactant combinations, because immediately after nucleation the particles already feature a hydrophilic surface that stabilize them; however, they may yield heterogeneous morphologies (micelles, polymersomes, worm-like or filomicelles)<sup>13</sup> due to the small energy differences between these self-assembled structures.

Phase separation follows the mixing in a (polar) organic solution of a polymer with a non-solvent, most often water (Figure 4). The conditions of thermodynamic insolubility (the spinodal decomposition) depend primarily on non-solvent content and temperature, but the actual rate at which particles nucleate are mostly affected by polymer concentration, amount of non-solvent in excess to the critical composition and diffusion coefficients of solvent, non-solvent and polymer (all affected by the medium viscosity).

In short, on the top of a thermodynamic basis, nucleation strongly depends on the mass transfer between the two phases during mixing. After nucleation, aggregation continues along two directions: 1) the addition of polymer chains onto growing particles, whose rate depends on concentration and diffusion coefficients of both, but also on the nature of the nanoparticle surface; 2) the coalescence of growing particles, which is facilitated by incomplete migration of the organic solvent into water and plasticizes the polymer; the coalescence rate again depends on the mass transfer of the solvent, and on the particle concentration and diffusivity. Importantly, this description applies to (nano)precipitation and to a certain extent to emulsion/vesicle formation, but point 2 does not generally apply to equilibrium processes, such as micellar self-assembly.

The most common parameters used to control mixing and thereby particle dimension are a) the total flow rate (TFR), and b) the flow rate ratio (FRR), i.e. the ratio between the velocities of the polymer solution and water, which also indicates the overall organic solvent/water composition. Reportedly, FRR has a higher influence on the final particle size; the lower the FRR (see also Figure 2, left), the more rapidly the critical nucleation concentration is attained, which leads to an accelerated particle formation (although the nucleation rate is not necessarily

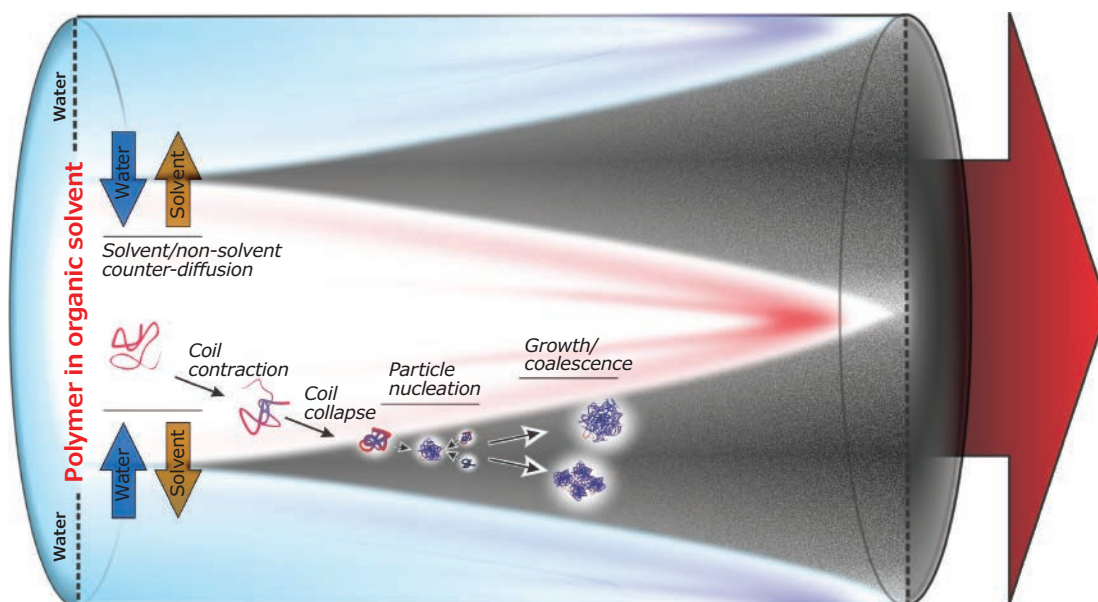


**Figure 4.** Different steps of phase separation (nanoprecipitation) in a flow-focused geometry. There are multiple levels of kinetic control: **A)** the mass transfer of solvent and non-solvent molecules through the phase boundary, leading to contraction and then collapse of macromolecular coils in the polymer-rich phase; **B)** the diffusion of collapsed polymer coils (globules) and their collisions eventually leading to particle nucleation; **C)** the increase in particle size due to anelastic collision and merging (coalescence) of particles (less likely with decreasing solvent content), or the incorporation of further individual macromolecules. The final average size of the particles and their average size distribution will therefore exhibit a complex dependence on the diffusion coefficients of the various species, on the overall flow rate and flow rate ratio, and on the polymer concentration.

**Table 2.** Overview of microfluidic-assisted nanoformulations.

	Technique	Junction/ mixer	Polymer a	Active principleb	Size (nm)	Solvent/ Non solventc	Ref
Phase-separation	HFF	X-shaped / linear	PLGA/PLGA-PEG	docetaxel	20-40	ACN/H <sub>2</sub> O	5
	HFF	X-shaped/ sinusoidal	PLGA/Pluronic F127	paclitaxel	100-200	Acetone/ H <sub>2</sub> O	6
	HFF	X-shaped/ linear	PLGA	ribavirin	20-250	[ACN, acetone DMSO]/ H <sub>2</sub> O	7
	HFF	Y-shaped / sinusoidal	PCL-PEO	paclitaxel	50-1000	DMF/ H <sub>2</sub> O	13
	HFF	Y-shaped / herringbone	PLGA/PVA	N-acetylcysteine	100-1000	[ACN, acetone or DMSO]/ H <sub>2</sub> O	14
	HFF	Y-shaped/ staggered herringbone	PLGA/PLGA-PEG	curcumin	50-200	Acetone/ H <sub>2</sub> O	15
	3D-HFF	Multi inlets; + X-shaped junction/ linear	PLGA/PLGA-PEG	docetaxel	30-200	ACN/ H <sub>2</sub> O	16
	HFF	X-shaped/ linear	PLGA-PEG	-	30-150	ACN/ H <sub>2</sub> O	17
	HFF	Cross-shaped/ linear	HMC	paclitaxel	50-220	pH 5.5/ pH 9 in water	18
	HFF	Y- vs. X-shaped/ Split & recomb. vs. sinusoid.	PLCL-PEG (linear & branched)	paclitaxel	30-160	Acetone/ H <sub>2</sub> O	19
Cross-linking	Co-flow	Y-junction (2-inlets)/ various geometries	PEI + nucleic acids	pDNA, mRNA, siRNA	200 -400	5% glucose	20
	Co-flow	Y-junction (2-inlets)/ not specified	Chitosan+ pDNA	Quantum dots, pDNA	Not specified	Aqueous (pH 6.5)	21
	HFF	Cross-shaped/ linear	Alginate + Ca <sup>2+</sup>	BSA	60-250	1mM CaCl <sub>2</sub>	22
	Coaxial + turbul.	Various geometries and mixing patterns	Alginate + Ca <sup>2+</sup>	Polymyxin B	65-250	10 mM Tris-HCl + CaCl <sub>2</sub>	23
	Co-flow	2 sequential inlets & micronozzles/linear	Ca Alginate + PLL	-	380-520	Aqueous	24
	HFF	X-shaped junction/ linear	cHANPs + divinyl sulfone	Gd-DTPA	70 -2000	Aqueous/ Acetone or ethanol	25

<sup>a</sup> Nomenclature: PLGA: poly(lactide-co-glycolide), PCL: poly(caprolactone), HMC: hydrophobically modified chitosan, PEG: poly(ethylene glycol), PEI: poly(ethylene imine), PLL: poly(L-lysine), cHANPs: crosslinked hyaluronic acid nanoparticles. <sup>b</sup> BSA: bovine serum albumin. Gd-DTPA: gadolinium diethylenetriamine penta-acetic acid. <sup>c</sup> ACN: acetonitrile, H<sub>2</sub>O: water, DMSO: dimethyl sulphoxide, DMF: N,N-dimethylformamide.

affected) with a resulting reduction in average size<sup>5,6,14,18</sup> and width of the size distribution. Further, the faster kinetics reduce the chance of extra-particle crystallization of drugs, allowing for higher encapsulation efficiencies.<sup>14,18</sup> TFR appears to have a less noticeable effect on particle size; yet, when mixing is favored by a higher overall flow (e.g. in HFF) or by a (semi) chaotic flow,<sup>7,14,15</sup> higher TFR leads to a lower particle size. TFR reportedly may also affect polymer crystallinity and above all the morphology of self-assembled block copolymers (from spheres at low TFR, to filomicelles and lamellae at higher TFR).<sup>13</sup> The influence of TFR on drug encapsulation is less clear, with reports of opposite effects depending on the microfluidics system, drug and polymer used.<sup>13-15</sup>

Two other control factors are the polymer molecular weight (MW) and the viscosity of its solution; the latter in turn depends on molecular weight itself, concentration, and architecture of the polymer. A higher MW of hydrophobes (whole polymers or

blocks in amphiphiles) is often suggested to increase particle size,<sup>16,17</sup> although sometimes no influence is reported.<sup>6</sup> The main underlying phenomenon is likely the lower solubility with increasing macromolecular size (= coil collapse happening faster during solvent exchange), but mixing conditions may complicate its influence: with a very rapid mixing, a higher MW may also increase the nucleation rate, possibly leading to more numerous but smaller particles. The effect of hydrophobicity may be similar in nature: more hydrophobic chitosans produce smaller particles<sup>18</sup> possibly because of higher nucleation rate.

For what attains to viscosity, an increase in particle size may be seen, but only when viscosity is significantly increased,<sup>14</sup> which may also be beneficial for the encapsulation efficiency;<sup>16</sup> however, high viscosity may be detrimental for mixing above all at the channel walls, leading to macroscopic aggregation and/or deposits.

## Nanomanufacturing Via Cross-Linking

The formation of a physically or chemically bound network can be used to generate nanoparticles if two interacting partners, typically dissolved in the same solvent, are appropriately mixed (Table 2, bottom section). Typically, neither coil transitions (e.g. collapse), nor particle coalescence occur significantly, and the main process determinants are the mass transfer between the two phases, the nucleation rate and the mechanism of particle growth. The most common approach utilizes polyelectrolyte complexation (polyanions such as alginate or nucleic acids, + polycations such as poly(ethylene imine) (PEI), poly(L-lysine) (PLL), chitosan or even calcium) as a cross-linking event. This is more popular than chemical cross-linking due to a better control over particle growth: using one reagent in excess, it is possible to obtain charged (self-repellant) particles grown mostly by addition of individual chains rather than through agglomeration. The nucleation rate typically depends on both the cation/anion concentration and their balance (also affected by pH), the ionic strength and the size of the two partners.

A major issue is the homogeneity and compactness of the nanoparticle bulk, which is often expressed through its mesh size. In this regard, the substantial irreversibility of the polyelectrolyte complexation makes the processes essentially kinetically controlled. For example, networks obtained by cross-linking alginate with a more avid and less diffusive polymeric cation are less homogeneous than those cross-linked by calcium ions; however, a higher nucleation rate (e.g. through disruption of laminar flow)<sup>23</sup> may yield more compact nanoparticles. Generally microfluidics provide more controlled mesh size and better bulk compaction<sup>22</sup> than batch processes, as evidenced by the higher surface charge (hence higher stability)<sup>24</sup> and lower cytotoxicity (less free polymer in solution).<sup>20</sup>

Importantly, in these approaches electrostatic interactions are most often used also to load bioactive components, which allows for encapsulation efficiencies much higher than in phase separation-based processes, which utilize partition and/or entrapment (typically efficiencies ranging 70-100% in one case vs. up to 20-30% in the other). As a result of a more firm loading, the release from polyelectrolyte complexes is seldom diffusional, and therefore typically features hardly any burst and a long duration.<sup>22,23</sup> More commonly, degradative events or a weakening of the electrostatic complexation are required to obtain significant drug delivery.

## Conclusions and Outlook

Microfluidics can assist nanomanufacturing through different mechanisms, most popularly through phase segregation (nanoprecipitation, self-assembly), but also polyelectrolyte complexation. The advantages over more conventional batch processes are in the reproducibility, tunability and at least partial scalability of the processes, which lends well to the development of personalized medicines.

Currently, the main areas for development are in a) the fluidodynamics of chaotic mixing, which promise a better control over size and loading, but where a detailed mechanistic understanding of aggregation is still lacking; b) the industrial scalability, since larger channels may lead to different flow regimes, and parallelization is often costly.

## References

- 1) Muhlebach, S. *Adv. Drug Deliv. Rev.* **2018**, *131*, 122-131.
- 2) Smith, J. A.; Mathew, L.; Burney, M.; Nyshadham, P.; Coleman, R. L. *Gynecol. Oncol.* **2016**, *141* (2), 357-363.
- 3) Bastogne, T. *Nanomedicine* **2017**, *13* (7), 2151-2157.
- 4) Commission, E. *Off. J. Eur. Union* **2011**, *275*, 38-40.
- 5) Karnik, R.; Gu, F.; Basto, P.; Cannizzaro, C.; Dean, L.; Kyei-Manu, W.; Langer, R.; Farokhzad, O. C. *Nano Lett.* **2008**, *8* (9), 2906-2912.
- 6) Donno, R.; Gennari, A.; Lallana, E.; De La Rosa, J. M. R.; d'Arcy, R.; Treacher, K.; Hill, K.; Ashford, M.; Tirelli, N. *Int. J. Pharm.* **2017**, *534* (1-2), 97-107.
- 7) Bramosanti, M.; Chronopoulou, L.; Grillo, F.; Valletta, A.; Palocci, C. *Colloid Surf. A* **2017**, *532*, 369-376.
- 8) Lim, J. M.; Swami, A.; Gilson, L. M.; Chopra, S.; Choi, S.; Wu, J.; Langer, R.; Karnik, R.; Farokhzad, O. C. *ACS Nano* **2014**, *8* (6), 6056-6065.
- 9) Burghelena, T.; Segre, E.; Bar-Joseph, I.; Groisman, A.; Steinberg, V. *Phys. Rev. E* **2004**, *69* (6), 8.
- 10) Lee, C. Y.; Wang, W. T.; Liu, C. C.; Fu, L. M. *Chem. Eng. J.* **2016**, *288*, 146-160.
- 11) Ou, J.; Moss, G. R.; Rothstein, J. P. *Phys. Rev. E* **2007**, *76* (1), 10.
- 12) Wang, S. S.; Jiao, Z. J.; Huang, X. Y.; Yang, C.; Nguyen, N. T. *Microfluid. Nanofluidics* **2009**, *6* (6), 847-852.
- 13) Bains, A.; Cao, Y. M.; Moffitt, M. G. *Macromol. Rapid Comm.* **2015**, *36* (22), 2000-2005.
- 14) Chiesa, E.; Dorati, R.; Modena, T.; Conti, B.; Genta, I. *Int. J. Pharm.* **2018**, *536* (1), 165-177.
- 15) Morikawa, Y.; Tagami, T.; Hoshikawa, A.; Ozeki, T. *Biol. Pharm. Bull.* **2018**, *41* (6), 899-907.
- 16) Valencia, P. M.; Pridgen, E. M.; Rhee, M.; Langer, R.; Farokhzad, O. C.; Karnik, R. *ACS Nano* **2013**, *7* (12), 10671-10680.
- 17) Baby, T.; Liu, Y.; Middelberg, A. P. J.; Zhao, C.-X. *Chem. Eng. Sci.* **2017**, *169*, 128-139.
- 18) Majedi, F. S.; Hasani-Sadrabadi, M. M.; Hojjati Emami, S.; Shokrgozar, M. A.; VanDersarl, J. J.; Dashtimoghadam, E.; Bertsch, A.; Renaud, P. *Lab Chip* **2013**, *13* (2), 204-207.
- 19) Lallana, E.; Donno, R.; Magri, D.; Barker, K.; Nazir, Z.; Treacher, K.; Lawrence, M. J.; Ashford, M.; Tirelli, N. *Int. J. Pharm.* **2018**, *548* (1), 530-539.
- 20) Debus, H.; Beck-Broichsitter, M.; Kissel, T. *Lab Chip* **2012**, *12* (14), 2498-2498.
- 21) Ho, Y.-P.; Chen, H. H.; Leong, K. W.; Wang, T.-H. *J. Vis. Exp.* **2009**, (30), 1432.
- 22) Bazban-Shotorbani, S.; Dashtimoghadam, E.; Karkhaneh, A.; Hasani-Sadrabadi, M. M.; Jacob, K. I. *Langmuir* **2016**, *32* (19), 4996-5003.
- 23) Borro, B. C.; Bohr, A.; Bucciarelli, S.; Boetker, J. P.; Foged, C.; Rantanen, J.; Malmsten, M. *J. Colloid Interface Sci.* **2019**, *538*, 559-568.
- 24) Kim, K.; Kang, D.-H.; Kim, M.-S.; Kim, K.-S.; Park, K.-M.; Hong, S.-C.; Chang, P.-S.; Jung, H.-S. *Colloids Surf.* **2015**, *471*, 86-92.
- 25) Russo, M.; Bevilacqua, P.; Netti, P. A.; Torino, E., *A Sci. Rep.* **2016**, *6*, 37906.

## Biodegradable Polymers

### Poly(lactide)

Name	Viscosity (dL/g)	Cat. No.
Resomer® L 207 S, Poly(L-lactide)	1.5-2.0	769940-25G 769940-5G
Resomer® L 209 S, Poly(L-lactide)	2.6-3.2	769932-5G 769932-25G
Resomer® L 210 S, Poly(L-lactide)	3.3-4.3	769924-25G 769924-5G
Resomer® R 207 S, Poly(D,L-lactide)	1.3-1.7	769843-5G 769843-1G
Resomer® R 205 S, Poly(D,L-lactide)	0.55-0.75	769835-1G 769835-5G

### Poly(lactide-co-glycolide)

Name	Lactide:Glycolide	Viscosity (dL/g)	Cat. No.
Resomer® RG 752 S, Poly(D,L-lactide-co-glycolide)	75:25	0.16-0.24	769827-1G 769827-5G
Resomer® RG 753 H, Poly(D,L-lactide-co-glycolide)	75:25	0.32-0.44	769819-1G 769819-5G
Resomer® RG 753 S, Poly(D,L-lactide-co-glycolide)	75:25	0.32-0.44	769800-1G 769800-5G
Resomer® RG 755 S, Poly(D,L-lactide-co-glycolide)	75:25	0.50-0.70	769797-5G 769797-1G
Resomer® RG 750 S, Poly(D,L-lactide-co-glycolide)	75:25	0.8-1.2	769770-5G 769770-1G
Resomer® RG 757 S, Poly(D,L-lactide-co-glycolide)	75:25	0.9-1.3	769789-5G 769789-1G
Resomer® LG 824 S, Poly(L-lactide-co-glycolide)	82:12	1.7-2.6	769894-25G 769894-5G
Resomer® LG 855 S, Poly(L-lactide-co-glycolide)	85:15	2.5-3.5	769886-5G 769886-25G
Resomer® LG 857 S, Poly(L-lactide-co-glycolide)	85:15	5.0-7.0	769878-5G 769878-25G
Poly(L-lactide-co-glycolide)	10:90	1.4-2.0	901021-5G

### Poly(L-lactide-co-D,L-lactide)

Name	Lactide:Lactide	Viscosity (dL/g)	Cat. No.
Resomer® LR 706 S, Poly(L-lactide-co-D,L-lactide)	70:30	3.3-4.2	769908-5G 769908-25G
Resomer® LR 708, Poly(L-lactide-co-D,L-lactide)	70:30	5.7-6.5	769959-25G 769959-5G
Poly(L-lactide-co-D,L-lactide)	70:30	2.0-3.0	901023-5G
Resomer® LR 704 S, Poly(L-lactide-co-D,L-lactide)	70:30	2.0-2.8	769916-5G 769916-25G

### Poly(L-lactide-co-ε-caprolactone)

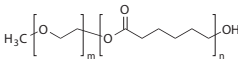
Name	Lactide:Caprolactone	Viscosity (dL/g)	Cat. No.
Poly(L-lactide-co-caprolactone)	90:10	1.4-2.0	906840-5G
Resomer® LC 703 S, Poly(L-lactide-co-ε-caprolactone)	70:30	1.3-1.8	769851-25G 769851-5G

## Biodegradable Diblock Copolymers

### Poly(ethylene glycol)-*block*-poly(lactide-co-glycolide)

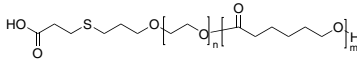
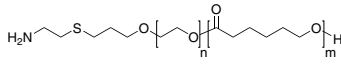
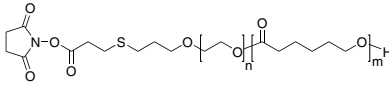
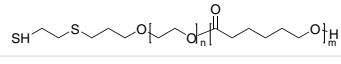
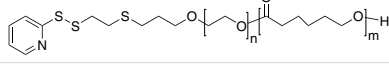
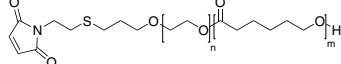
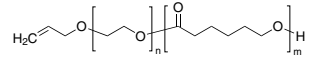
Name	Structure	Molecular Weight	Cat. No.
Poly(ethylene glycol) methyl ether- <i>block</i> -poly(lactide-co-glycolide)		PEG average $M_n$ 5,000 PLGA $M_n$ 7,000 average $M_n$ 12,000 (total)	765139-1G
		PEG average $M_n$ 5,000 PLGA $M_n$ 55,000 average $M_n$ 60,000 (total)	764752-1G
		PEG average $M_n$ 2,000 PLGA average $M_n$ 11,500 average $M_n$ 13,500 (total)	764760-1G
		PEG $M_n$ 2,000 PLGA $M_n$ 4,500 average $M_n$ 6,500 (total)	764825-1G

## Poly(ethylene glycol)-*block*-poly(caprolactone)

Name	Structure	Molecular Weight	Cat. No.
Poly(ethylene glycol)- <i>block</i> -poly( $\epsilon$ -caprolactone) methyl ether		PCL average $M_n \sim 5,000$ PEG average $M_n \sim 5,000$ average $M_n \sim 10,000$ (total)	570303-250MG 570303-1G
		PCL average $M_n \sim 13,000$ PEG average $M_n \sim 5,000$ average $M_n \sim 18,000$ (total)	570311-250MG 570311-1G
		PCL average $M_n \sim 32,000$ PEG average $M_n \sim 5,000$ average $M_n \sim 37,000$ (total)	570338-250MG 570338-1G

## Functionalized Biodegradable Diblock Copolymers

### Poly(ethylene glycol)-*block*-poly(caprolactone)

Name	Structure	Molecular Weight	Cat. No.
Carboxylic acid-poly(ethylene glycol)- <i>b</i> -poly( $\epsilon$ -caprolactone)		PCL average $M_n 5,000$ PEG average $M_n 5,000$	901702-500MG
Amine-poly(ethylene glycol)- <i>b</i> -poly( $\epsilon$ -caprolactone)		PCL average $M_n 5,000$ PEG average $M_n 5,000$	904740-500MG
<i>N</i> -Hydroxysuccinimide ester-poly(ethylene glycol)- <i>b</i> -poly( $\epsilon$ -caprolactone)		PCL average $M_n 5,000$ PEG average $M_n 5,000$	901841-500MG
Thiol-poly(ethylene glycol)- <i>b</i> -poly( $\epsilon$ -caprolactone)		PCL average $M_n 5,000$ PEG average $M_n 5,000$	901708-500MG
Pyridyl disulfide-poly(ethylene glycol)- <i>b</i> -poly( $\epsilon$ -caprolactone)		PCL average $M_n 5,000$ PEG average $M_n 5,000$	901910-500MG
Maleimide-poly(ethylene glycol)- <i>b</i> -poly( $\epsilon$ -caprolactone)		PCL average $M_n 5,000$ PEG average $M_n 5,000$	902381-500MG
Allyl-poly(ethylene glycol)- <i>b</i> -poly( $\epsilon$ -caprolactone)		PCL average $M_n 5,000$ PEG average $M_n 5,000$	901844-1G

## Chitosan

Name	Average $M_w$	Degree Of Deacetylation	Cat. No.
Chitosan	50,000-190,000 Da	75-85%	448869-50G 448869-250G
Chitosan	-	75-85%	448877-50G 448877-250G
Chitosan	310000-375000 Da	>75%	419419-50G 419419-250G
Chitosan	190000-375000 Da	$\geq 75\%$	417963-25G 417963-100G
Chitosan	100 kDa	$\geq 95\%$	900344-2G
Chitosan	5,000 Da	$\geq 80\%$	900345-2G
Chitosan	50 kDa	$\geq 80\%$	900341-2G



# EVERYTHING BUT THE KITCHEN SINK

## Comprehensive biodegradable polymers for drug delivery

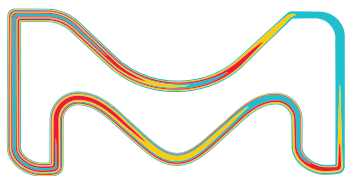
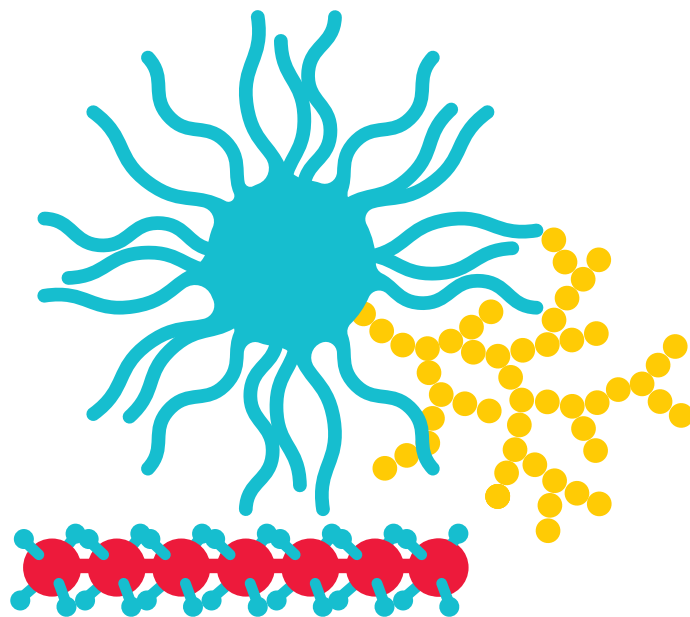
Biodegradable polymers contain polymer chains that are hydrolytically or enzymatically cleavable, resulting in biocompatible or nontoxic by-products. They are widely used in drug delivery research to achieve controlled and targeted delivery of therapeutic agents (e.g. APIs, genetic material, peptides, vaccines, and antibiotics).

### We now offer the following classes of high-purity biodegradable polymers:

- Poly (lactide-co-glycolide) copolymers (PLGA)
- Poly(lactic acid) (PLA)
- Poly(caprolactone) (PCL)
- Amphiphilic block copolymers
- End-functionalized biodegradable polymers

For more information, please visit:

[SigmaAldrich.com/resomer](https://www.sigmaaldrich.com/resomer)



The life science  
business of Merck  
KGaA, Darmstadt,  
Germany operates as  
MilliporeSigma in the  
U.S. and Canada.

**Sigma-Aldrich®**  
Lab & Production Materials

# Three-Dimensional Bioprinting for Tissue and Disease Modeling



Dr. S. Maharjan,<sup>1,2</sup> Ms. D. Bonilla,<sup>1,3</sup> Prof. Y. S. Zhang<sup>1\*</sup>

<sup>1</sup>Division of Engineering in Medicine, Brigham and Women's Hospital, Department of Medicine, Harvard Medical School, Cambridge, MA 02139, USA

<sup>2</sup>Research Institute for Bioscience and Biotechnology, Lalitpur 44600, Nepal

<sup>3</sup>Escuela de Ingeniería y Ciencias, Tecnológico de Monterrey, Ave. Eugenio Garza Sada 2501, Monterrey, NL 64849, México

\*E-mail: yszhang@research.bwh.harvard.edu

## Introduction

Three-dimensional (3D) bioprinting is developing rapidly, and offers enormous potential for the fabrication of living tissue constructs.<sup>1,2</sup> In the most common form, bioprinting uses a computer-assisted motorized device for the layer-by-layer deposition of biocompatible materials, viable cells, growth factors, proteins, nucleic acids, drugs, and supporting components into precise geometries to create functionally and structurally biomimetic tissue constructs.

In recent years, 3D bioprinting has significantly advanced the field of tissue and disease modeling to facilitate drug development and therapeutic screening. In general, bioprinting is based on one of a few main technological approaches such as: extrusion, inkjet, laser-assisted, or stereolithographic.<sup>3</sup> Extrusion-based bioprinting utilizes mechanical or pneumatic forces to dispense a bioink through a nozzle to form a continuous filament. Currently the most commonly used bioprinting method, extrusion-based bioprinting is comparatively slow and has lower resolution, but can fabricate constructs from high-viscosity bioinks with reasonable cell viability. Inkjet bioprinting employs thermal, piezo, or acoustic forces to deposit a bioink in the form of droplets, offering fast fabrication speeds but low cell densities. While extrusion bioprinting can typically work with high viscosity bioinks, inkjet bioprinting requires bioinks with low viscosities. Laser-assisted bioprinting is a nozzle-free technique that uses laser pulses to deposit bioink from the donor slide onto the receiver substrate. Although this allows deposition of

highly viscous and densely cellularized bioinks, it is limited by the lower cell survival rate. Finally, stereolithographic bioprinting utilizes precisely controlled patterns of light to photopolymerize photosensitive polymers on a vertically movable collecting platform in a layer-by-layer process, thus forming 3D constructs of the desired structure. Stereolithographic bioprinting offers higher resolution, rapid fabrication, and higher cell viability than other methods.

Despite the different approaches, most bioprinting processes consist of a similar series of steps: (i) construction of the 3D model using computer-aided design software, (ii) development/selection of the bioink, usually a combination of one or more compatible biomaterials and viable cells, depending on the modality and specific tissue to be bioprinted, (iii) robotically programmed bioprinting with in-printing and/or post-printing physical and/or chemical crosslinking, and (iv) maturation of the bioprinted tissue construct. Generally, the matured bioprinted tissue constructs are specifically designed for applications in tissue engineering and regenerative medicine.<sup>2</sup> More recently, the fabrication of functional tissue models using 3D bioprinting approaches have been used in disease modeling, drug development, and screening of personalized therapeutics.<sup>4</sup> Herein we briefly review bioink selections and provide representative examples relating to the applications of 3D bioprinting in tissue model biofabrication (**Figure 1**).



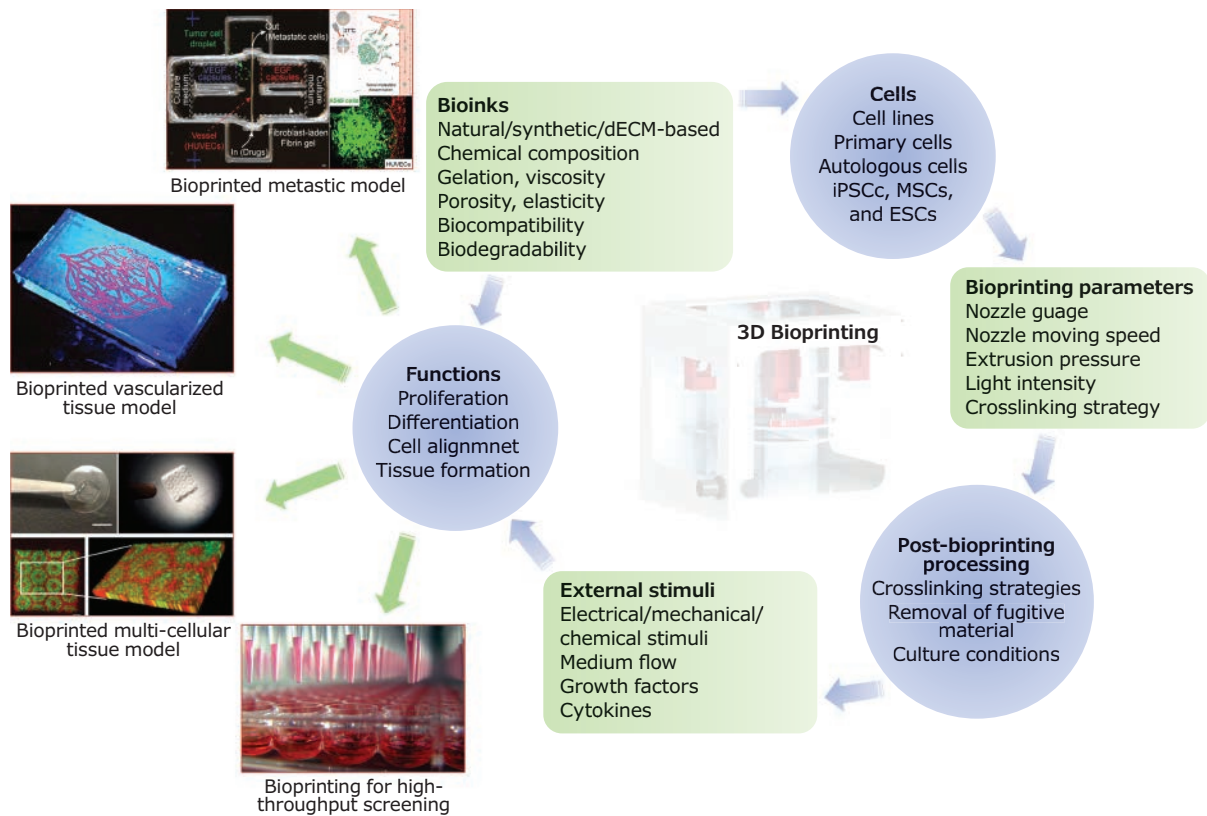


**Figure 1.** The essential components and applications of 3D bioprinting. Bioinks, bioprinting parameters, and post-bioprinting processing all impact viability and functionality of cells, which in turn affect subsequent cellular events, such as proliferation, differentiation, and tissue formation. hiPSCs: Human induced pluripotent stem cells, MSCs: Mesenchymal stem cells and ESCs: Embryonic stem cells. The bioprinted metastatic model and perfusable vascularized tissue were reproduced with permission from references 27 and 28, copyright 2019 and 2017 Wiley. The bioprinted liver model was reproduced with permission from reference 18, copyright 2016 United States National Academy of Sciences.

## Bioink Development and Choice of Biomaterials

Bioinks are one of the most important components of 3D bioprinting. A bioink is essentially a hydrogel biomaterial, containing one or more cell types, nutrients, and growth factors in varying amounts, that mimics the extracellular matrix (ECM) of the tissue and supports the growth of the embedded cells.<sup>5</sup> Designing biologically relevant bioinks is one of the critical challenges for fabrication of 3D-bioprinted tissue constructs. The bioink should not only provide structural, physical, and mechanical support to the embedded cells, but also supply them with the essential biological and chemical cues for cell survival, proliferation, and differentiation required for tissue morphogenesis and homeostasis. The selection of proper biomaterial (or combination of biomaterials) for a bioink is a key step for successful bioprinting of tissues, and it depends on several factors such as the bioprinting modality to be used, the tissue of interest, and any post-printing processes that are required. In general, an ideal bioink should (i) have good printability; (ii) be curable with a cell-friendly method, (iii) have suitable mechanical strength to maintain the structural integrity of tissue of interest, (iv) be biocompatible and biodegradable without eliciting any toxicity or immunological reactions, (v) mimic the *in vivo* microenvironment to support and promote cellular activities such as adhesion, migration, proliferation, and differentiation of living cells (Figure 2A–B).

To date, numerous hydrogel biomaterials have been used for the formulation of bioinks for 3D bioprinting of tissues (Figure 2C). These include, for example, naturally-derived biomaterials based on collagen, gelatin, alginate, fibrin, hyaluronic acid, silk proteins, chitosan, and decellularized ECM (dECM), as well as synthetic biomaterials such as poly(ethylene glycol) (PEG), poly(hydroxyethyl methacrylate), and polyvinyl alcohol.<sup>4</sup> Natural sources are a favorable subset of biomaterials because of their biocompatibility, tunable degradation, and intrinsic resemblance to native ECM. However, weak mechanical strength and inconsistency in compositions and properties between production batches are common drawbacks.<sup>6</sup> On the other hand, synthetic biomaterials are highly defined and reproducible with tunable compositions. In addition, they are often biologically inert, being both nontoxic and nonimmunogenic. The mechanical properties, degradation rate, and composition of synthetic biomaterials can be easily controlled. However, synthetic materials often lack adequate sites for cell adhesion and do not exhibit the complexity of native ECM.<sup>7</sup> Therefore, synthetic materials are often combined with natural biomaterials to overcome these limitations, and to engineer tissue-like microenvironments that mimic both the chemical and physical characteristics of native ECM. For example, 4-arm PEG-tetraacrylate (PEGTA)-gelatin methacryloyl (GelMA) and 8-arm PEG-octoacrylate (PETOA)-GelMA composite bioinks were developed for 3D bioprinting of biomimetic vascular tissues.<sup>8,9</sup> The addition of PEG derivatives

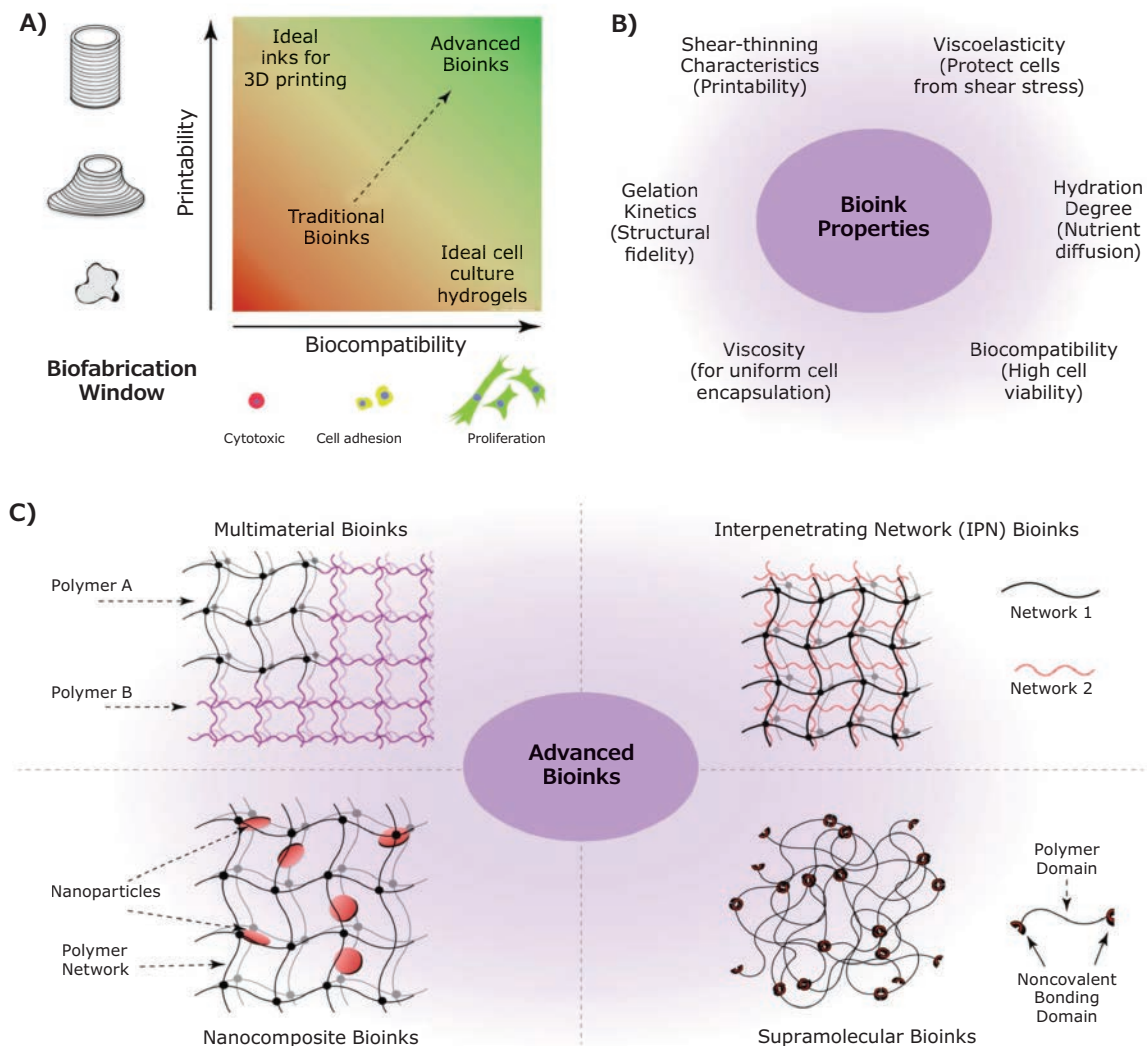


**Figure 2.** Bioprinting and Bioprinted Tissue/Disease Models. **A)** Rational approach for designing bioinks requires considering both printability and biocompatibility. **B)** Properties of an ideal bioink. **C)** Classification of advanced bioinks into four major groups. Reproduced with permission from reference 5, copyright 2016 Springer Nature.

to GelMA provides adequate rheological and other mechanical properties that facilitate the bioprinting of complex multilayer hollow structures.

However, these composite hydrogels still may not possess sufficient biomimetic physicochemical properties to deliver tissue-specific functions. As a result, dECM-derived hydrogels have been increasingly used as bioinks. The decellularization process uses a combination of mechanical, chemical, and enzymatic treatments to remove all cellular components, yielding a collagenous matrix that keeps many of the structural ECM components and soluble factors intact. Studies have shown that dECM preserves the biochemical composition of the native ECM tissue from which it is derived, which proves important for maintaining phenotypes and functionality of the cells when forming biologically relevant tissues. For example, bioprinted renal constructs using kidney dECM-derived bioink exhibited physiologically relevant features of the native renal tissue.<sup>10</sup> Similarly, 3D bioprinting of the dECM-based bioinks derived

from pepsin-solubilized heart, adipose, and cartilage tissues exhibited high cell viability and functionality of the bioprinted rat myoblasts, human adipose-derived stem cells, and human mesenchymal stem cells in the respective tissue constructs.<sup>11</sup>

### Bioprinted Tissue/Disease Models and Their Applications in Probing Drug Effects

Bioprinted tissue constructs with spatially controlled architectures represent important *in vitro* tools for tissue and disease modeling, with relevant applications in toxicology. These models allow study of the biochemical, genetic, and histological consequences of specific drugs thus providing pharmacokinetic, pharmacodynamic, and toxicity information. In this section, we examine some applications of 3D-bioprinted tissue and disease models in studying tissue-specific functions, drug-metabolizing activities, and drug responses. The representative bioprinted tissue models used for drug screening applications are listed in **Table 1**.

**Table 1.** Representative bioprinted tissue models for drug screening applications.

3D-bioprinted tissue models	Bioprinting modality	Bioink(s)	Cell Type(s)	Compounds tested	Ref
Cardiac tissue	Extrusion	Fibrinogen, gelatin, aprotinin, glycerol, hyaluronic acid	Rat primary cardiomyocytes	Epinephrine, carbachol	12
Endothelialized cardiac tissue	Extrusion	Alginate, GelMA	Neonatal rat cardiomyocytes, HUVECs	Doxorubicin	13
Renal proximal tubule	Extrusion	Pluronic F127, thrombin; gelatin, fibrinogen, transglutaminase	Human primary proximal tubule epithelial cells, human neonatal dermal fibroblasts	Cyclosporine A	15
Vascularized renal proximal tubule	Extrusion	Pluronic F127, thrombin; gelatin, fibrinogen, transglutaminase, PEO.	Human primary proximal tubule epithelial cells, human primary glomerular microvascular endothelial cells	Albumin, inulin, glucose, dapagliflozin	16
Liver tissue	Stereolithography	GelMA, glycidal methacrylate-hyaluronic acid	hiPSC-derived hepatic cells, HUVECs, human adipose-derived stem cells	Rifampicin	18
	Extrusion	NovoGel 2.0	Human primary parenchymal cells, HUVECs, human primary hepatic stellate cells	Trovafloxacin, levofloxacin	19
	Extrusion	GelMA	HepG2/C3A human hepatocellular carcinoma cell line	Acetaminophen	21
Intestinal tissue	Extrusion	NovoGel	Human primary intestinal epithelial cells, human primary intestinal myofibroblasts, Caco-2 human intestinal epithelial cell line	Indomethacin, rhodamine 123, lucifer yellow, mitoxantrone, digoxin, propranolol, topotecan	22
<b>Tumor models</b>					
Glioma	Extrusion	Alginate, gelatin, fibrinogen	SU3 human glioma stem cell line, U87 human glioma cell line	Temozolomide	23
Cervical cancer	Extrusion	Alginate, gelatin, fibrinogen	HeLa human cervical epithelial carcinoma cell line	Paclitaxel	24
Glioma	Extrusion	GelMA, gelatin	RAW264.7 mouse macrophage cell line, GL261 mouse glioblastoma cells	Carmustine, AS1517499, BLZ945	25
Ovarian cancer	Droplet	Matrigel	OVCAR-5 human ovarian cancer cell line, MRC-5 human lung fibroblasts		26
Vascularized lung cancer	Droplet	PLGA; fibrin	A549 human lung cancer cell line, HUVECs	Immunotoxin EGF4KDEL, CD22KDEL	27

### Cardiac Tissue Models

Bioprinting has the potential to generate physiologically relevant, 3D contractile cardiac tissues for drug testing applications. For example, rat primary cardiomyocytes encapsulated in a fibrin-based bioink containing fibrinogen, gelatin, aprotinin, glycerol, and hyaluronic acid were bioprinted to create cardiac tissue constructs with spontaneous and synchronous contractions in *in vitro* culture.<sup>12</sup> These constructs were evaluated for physiological responses to known cardiotoxic drugs including epinephrine and carbachol. Epinephrine (200 nM) increased the beating frequency from 80 to 110 beats per minute, while carbachol (10  $\mu$ M) was found to decrease the beating frequency to 40 beats per minute. As blood vessels play an important role in transporting nutrients, oxygen, and drugs in and out of tissues including the

heart, another recent example demonstrated fabrication of 3D endothelialized microfibrinous scaffolds by extrusion bioprinting of human umbilical vein endothelial cells (HUVECs)-loaded alginate/GelMA blend bioink (Figure 3A–B). This was further seeded with neonatal rat cardiomyocytes or iPSC-derived cardiomyocytes, thus generating endothelialized myocardial tissues capable of spontaneous and synchronous contractions (Figure 3C).<sup>13</sup> This tissue model was later integrated in a microfluidic bioreactor and used to study the toxicity of an anti-cancer drug, doxorubicin, in a dose- and time-dependent manner. When exposed to doxorubicin for 6 days, the beating rate of cardiomyocytes decreased with simultaneous reduction in the secretion of von Willebrand factor (vWF) by the HUVECs (Figure 3D–E).



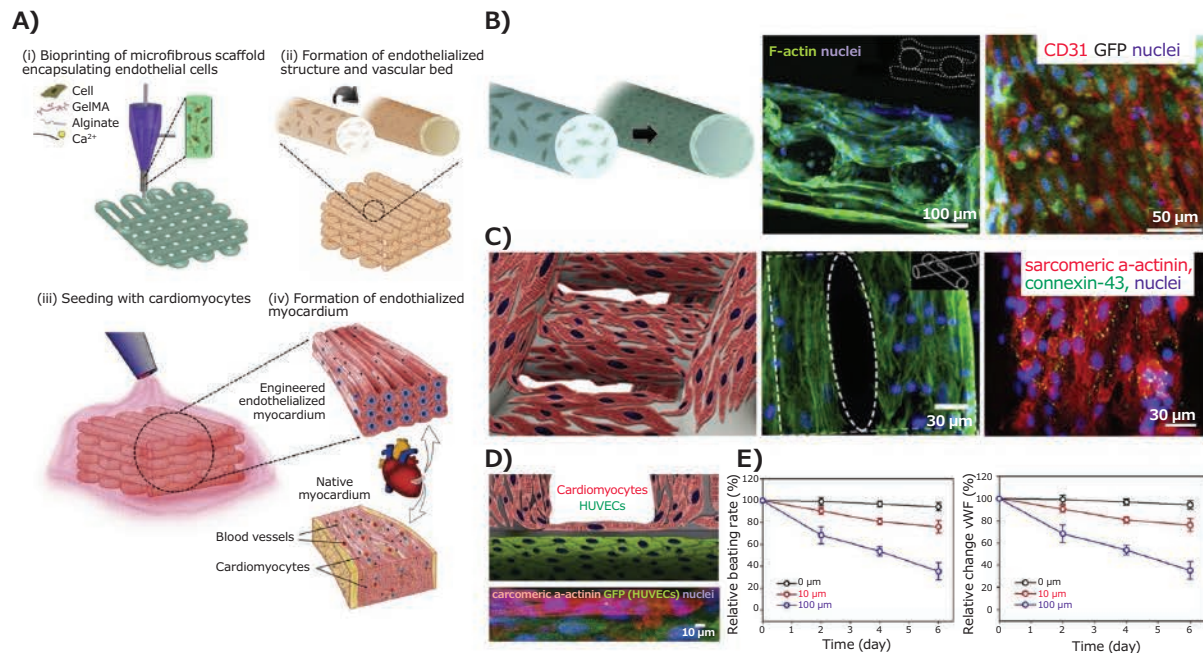


**Figure 3.** Application of 3D-bioprinted tissue models in drug testing — 3D-bioprinted endothelialized myocardium model. **A)** Schematics showing the procedure of fabricating endothelialized myocardium tissue model. **B)** Schematic showing the assembly of HUVECs in the bioprinted microfibrils into a confluent layer of endothelium on the peripheries, as well as confocal fluorescence images showing the cross-sectional view of a three-layer scaffold, and tight junction formation between the HUVECs. **C)** Schematic showing a scaffold seeded with neonatal rat cardiomyocytes, F-actin staining showing the distribution of cardiomyocytes on the surface of the microfibrils, and immunofluorescence staining of sarcomeric  $\alpha$ -actinin and connexin-43 expressions. **D)** Schematic and high-resolution confocal fluorescence micrograph showing an endothelialized myocardial tissue. **E)** Relative beating of the endothelialized myocardial tissues and the levels of vWF expression by the endothelial cells, upon treatment with different dosages of doxorubicin. Reproduced with permission from reference 13, copyright 2016 Elsevier.

## Kidney Tissue Models

Human kidneys filter approximately 180 L of plasma each day, reabsorbing water and solutes through renal tubules, and removing waste from the blood,<sup>14</sup> making them susceptible to damage by drugs and toxins. Bioprinting is a promising method for fabricating kidney tissues or components (such as renal tubules) that exhibit renal filtration, reabsorption, and secretory functions. Homan et al. bioprinted renal proximal tubules using extrusion bioprinting, in which a sacrificial bioink made of Pluronic F127 and thrombin was first printed on a gelatin-fibrinogen-transglutaminase ECM. This was followed by removal of the Pluronic F127, creating a hollow tubule within the crosslinked ECM (**Figure 4A–B**).<sup>15</sup> Proximal tubule epithelial cells were then seeded within the tubule and allowed to grow to maturity under continuous medium perfusion through the lumen (**Figure 4C**). The perfusable proximal tubules exhibited an epithelial-like morphology, which was disrupted when treated with cyclosporine A in a dose-dependent manner (**Figure 4D**). The same group later reported<sup>16</sup> bioprinting of a 3D vascularized proximal tubule model, composed of two adjacent proximal tubule and vascular conduits embedded in an ECM, using their original ECM and fugitive bioink with slight modifications (**Figure 4E**). The proximal and vascular channels were seeded with proximal tubule epithelial cells and glomerular microvascular endothelial cells, respectively (**Figure 4F**). Biomacromolecule

uptake was studied using fluorescently labeled albumin and inulin, and albumin was found to be reabsorbed selectively. Further, epithelium-endothelium crosstalk was studied by circulating high-glucose (400 mg glucose/dL) medium with or without dapagliflozin and normal glucose (100 mg glucose/dL) medium through the proximal tubule and monitoring both glucose reabsorption and endothelial cell dysfunction.

## Liver Tissue Models

Hepatotoxicity remains the primary reason for late-stage failures of many drugs,<sup>17</sup> making liver drug toxicity studies crucial for drug development. To this end, 3D bioprinting has been used to create liver tissue models that reliably reproduce drugs metabolism, as well as glucose and lipid metabolisms. An example of this is when digital light processing-based stereolithographic bioprinting was employed to develop a 3D hepatic lobule model with patterned human induced pluripotent stem cell (hiPSC)-derived hepatic cells, HUVECs, and the adipose-derived stem cells in a physiologically-relevant architecture using GelMA and glycidyl methacrylate-hyaluronic acid.<sup>18</sup> The authors investigated the expression of different hepatic marker genes and enzymes involved in drug metabolism in hiPSC-derived hepatic progenitor cells (hiPSC-HPCs) in the bioprinted 3D hepatic model, and found that among the five cytochromes P450 (CYP1A2, CYP2B6, CYP2C9, CYP2C19, and

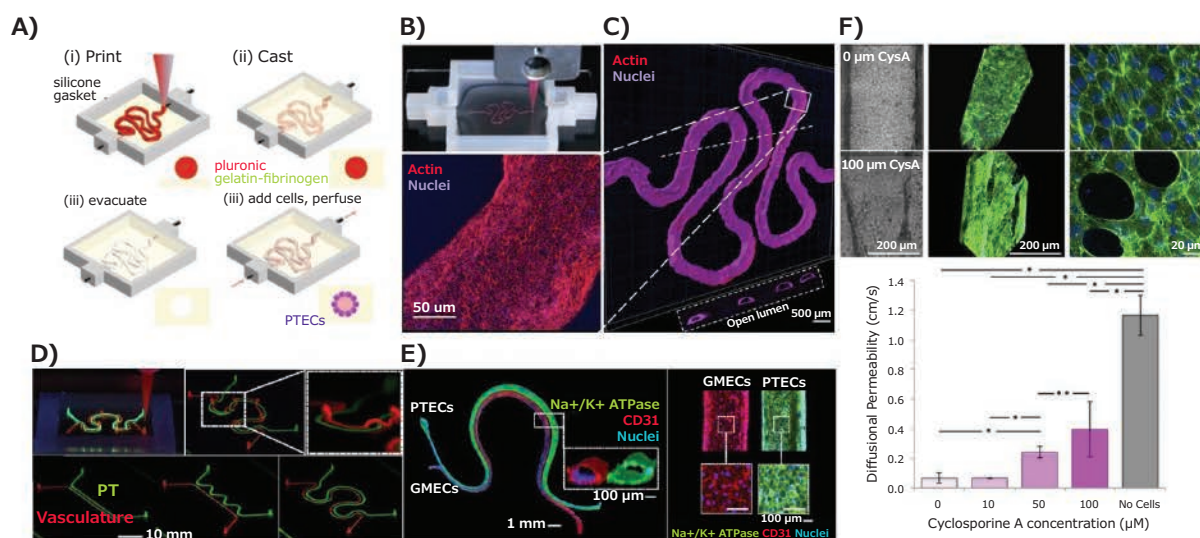


**Figure 4.** Application of 3D-bioprinted tissue models in drug testing — 3D-bioprinted convoluted renal proximal tubule model. **A)** Schematics of different steps in the fabrication of 3D renal proximal tubule. **B)** Photograph showing the bioprinting process of a proximal tubule (Pluronic F127 fugitive template). **C)** Confocal projection and 3D rendering images of the bioprinted convoluted proximal tubule populated with a confluent layer of proximal tubule epithelial cells. **D)** Cyclosporine A-induced disruption of the epithelial barrier function by quantifying the diffusional permeability of fluorescein isothiocyanate (FITC)-dextran (70 kDa). **E)** Simple and complex bioprinted vascularized proximal tubule (3D VasPT) models. **F)** Confocal images of the 3D VasPT containing epithelial cells in the proximal tubule and endothelial cells in the vessel. Reproduced under the Creative Commons Attribution License 4.0. Reprinted with permission from references 15 and 16, copyright 2016 Nature and 2019 United States National Academy of Sciences.

CYP3A4), the expressions of the most common CYP, CYP3A4, were significantly higher in hiPSC-HPCs. Approximately half of the drugs used today are estimated to be metabolized by CYP3A4,<sup>18</sup> making this a promising model system. They further evaluated the effect of rifampicin, an antibiotic with potential hepatotoxicity, and showed that rifampicin significantly increased the expressions of CYP3A4, CYP2C9, and CYP2C19 in hiPSC-HPCs in the 3D-bioprinted hepatic model when compared to untreated controls. In another study by Nguyen et al.,<sup>19</sup> a liver tissue model was fabricated by the microextrusion method using primary human parenchymal cells (100% hepatocyte cellular paste, generated via compaction) and non-parenchymal cells (HUVECs and hepatic stellate cells in NovoGel hydrogel). Their responses to the known hepatotoxicant trovafloxacin were studied in comparison to levofloxacin, revealing that trovafloxacin induced significant toxicity at clinically relevant doses ( $\leq 4 \mu\text{M}$ ) in a dose-dependent manner. Similarly, an extrusion-bioprinted liver model using HepG2 cell-laden Matrigel was used in a microfluidic system to analyze the metabolism of amifostine, an anti-radiation prodrug.<sup>20</sup> Moreover, 3D bioprinting of human HepG2/C3A spheroids was achieved within the GelMA bioink directly in a bioreactor (Figure 5A–B).<sup>21</sup> The liver-on-a-chip platforms with bioprinted hepatic spheroids were cultured under medium perfusion and analyzed for albumin, alpha-1 antitrypsin (A1AT), transferrin, and ceruloplasmin secretions as well as for expressions of cytokeratin 18, multi-drug resistance-associated protein 2 (MRP-2), and tight junction protein ZO-1 in hepatocytes within the bioprinted constructs (Figure 5C). The toxicity of acetaminophen (APAP) was further evaluated (Figure 5D), demonstrating application of the model for drug toxicity testing.

## Intestinal Tissue Models

The intestine is one of the main organs in which drugs are reabsorbed. Recently, a bi-layered intestinal tissue model was generated by extrusion bioprinting of an interstitial layer using adult human intestinal myofibroblasts, and an epithelial layer using adult human intestinal epithelial cells suspended in a thermo-responsive NovoGel.<sup>22</sup> The intestinal tissue constructs demonstrated a polarized epithelium with the expression of tight junction proteins such as E-cadherin, ZO-1, and functional CYP450 enzymes. Permeability studies were performed using Lucifer yellow, mitoxantrone, digoxin, propranolol, and topotecan. In addition, the toxicity of indomethacin, a nonsteroidal anti-inflammatory drug, was studied, and it was found that barrier function decreased in the bioprinted intestinal tissue in a dose-dependent manner.

## Tumor Models

In addition to normal tissues, bioprinting has shown promise in the fabrication of tumor tissue models that better replicate the native tumor microenvironment, which is critical for tumor cell proliferation, metastatic dissemination, and responses to pharmaceutical agents. An extrusion-based 3D bioprinted glioma model was established using a glioma stem cell-laden porous alginate/gelatin/fibrinogen bioink.<sup>23</sup> The drug-sensitivity studies using this glioma CysA model showed increased resistance to temozolomide when compared to monolayer cultures at concentrations of 400–1600  $\mu\text{g mL}^{-1}$ . More recently, a two-step extrusion bioprinting of mini-brains was reported in which the larger brain tissue was first bioprinted with an empty cavity using mouse macrophage cells, then the cavity was filled with

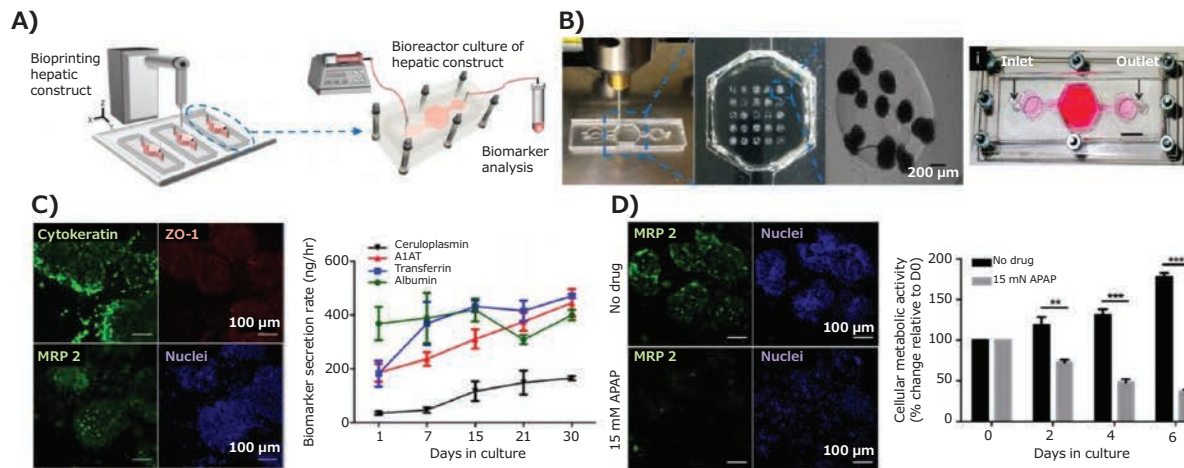


**Figure 5.** 3D-bioprinted liver model. **A)** Schematic of the hepatic bioreactor culture platform integrated with a bioprinter and biomarker analysis module. **B)** Bioprinting of GelMA hydrogel-based hepatic constructs directly within the bioreactor as a dot array, and topview of the assembled bioreactor (scale bar: 1 mm). **C)** Confocal images showing the bioprinted HepG2/C3A spheroids stained for cytokeratin 18, ZO-1, MRP-2, and nuclei, and the rate of secretion of hepatic biomarkers, albumin, A1AT, and ceruloplasmin, by HepG2/C3A spheroids. **D)** Confocal images showing MRP2 expressions and measured metabolic activity of the hepatic spheroids subjecting to APAP-induced hepatotoxicity in a dose-dependent manner. Reproduced with permission from reference 21, copyright 2016 IOP publishing.

mouse glioblastoma cells, with both cells encapsulated in the GelMA/gelatin blend bioink.<sup>24</sup> The glioblastoma cells actively recruited macrophages, polarizing them into a glioblastoma-associated macrophage-specific phenotype. The effects of carmustine, a common chemotherapy for glioblastoma, and two immunomodulatory drugs, AS1517499 (a Stat6 inhibitor) and BLZ945 (an inhibitor of colony stimulating factor 1 receptor (Csf-1r)) were investigated. Moreover, a 3D cervical cancer tumor model was bioprinted using HeLa cells encapsulated in gelatin/alginate/fibrinogen, which showed increased chemoresistance to paclitaxel when compared to planar cultures.<sup>25</sup> In another study, a 3D ovarian cancer model was generated by microvalve cell deposition (i.e., inkjet bioprinting) using OVCAR-5 human ovarian cancer cells and MRC-5 fibroblasts micropatterned on Matrigel.<sup>26</sup> OVCAR-5 and MRC-5 cells were ejected simultaneously using dual ejector heads in a spatially controlled microenvironment, in a high-throughput and reproducible manner. OVCAR-5 cells overlaid on Matrigel spontaneously formed multicellular acini of ~100–500 μm<sup>2</sup> in size and gradually increased heterogeneity over the 15-day culture period.

In addition, Meng et al.<sup>27</sup> reported a 3D-bioprinted vascularized tumor model that mimics metastatic dissemination by integrating lung tumor cells (A549 cells), HUVECs-lined vascular conduits, and biochemical signals from 3D-bioprinted core/shell capsules. Growth factor-loaded GelMA hydrogel was chosen as the core, and gold nanorods-functionalized poly(lactic-co-glycolic acid) (PLGA) films as shells, while a fibroblast-laden, fibrin hydrogel matrix served as the main component of the tumor stroma. Tumor cell invasion into the surrounding matrix and intravasation into the vasculature were studied using epidermal growth factor and vascular endothelial growth factor gradients, which were dynamically released from the capsules. In addition, potency and targeting of two immunotoxin ligand-directed toxins, EGF4KDEL and CD22KDEL, were studied.

## Conclusions

The use of 3D-bioprinted tissue models for *in vitro* drug testing advanced significantly in recent years, and these tissue models show promise for enhanced reproducibility, which will reduce the cost of drug discovery and development through automated bioprinting operations. Another benefit lies in the potential of these bioprinted tissue models to reduce the use of animals for drug testing by both academic labs and pharmaceutical companies. Still, many challenges remain, such as the need for increased speed and resolution, availability of tissue and/or patient-specific cells, and the need for proper vascularization of the tissue models. In addition, limited biomaterials are available for use at this time. Thus, there is a pressing need for novel bioink formulations to improve the fabrication of functional tissue constructs and facilitate their applications in drug testing.

## References

- (1) Stanton, M. M.; Samitier, J.; Sánchez, S. *Lab Chip* **2015**, *15* (15), 3111–3115.
- (2) Murphy, S. V.; Atala, A. *Nat Biotechnol.* **2014**, *32*, 773.
- (3) Heinrich, M. A.; Liu, W.; Jimenez, A.; Yang, J.; Akpek, A.; Liu, X.; Pi, Q.; Mu, X.; Hu, N.; Schiffelers, R. M.; Prakash, J.; Xie, J.; Zhang, Y. S. *Small* **2019**, *15* (23), 1805510.
- (4) Ma, X.; Liu, J.; Zhu, W.; Tang, M.; Lawrence, N.; Yu, C.; Gou, M.; Chen, S. *Adv. Drug Deliv. Rev.* **2018**, *132*, 235–251.
- (5) Chimene, D.; Lennox, K. K.; Kaunas, R. R.; Gaharwar, A. K. *Ann Biomed Eng.* **2016**, *44* (6), 2090–2102.
- (6) Keane, T. J.; Badyal, S. F. *Semin Pediatr Surg.* **2014**, *23* (3), 112–118.
- (7) Zhu, J. *Biomaterials* **2010**, *31* (17), 4639–4656.
- (8) Jia, W.; Gungor-Ozkerim, P. S.; Zhang, Y. S.; Yue, K.; Zhu, K.; Liu, W.; Pi, Q.; Byambaa, B.; Dokmeci, M. R.; Shin, S. R. *Biomaterials* **2016**, *106*, 58–68.
- (9) Pi, Q.; Maharjan, S.; Yan, X.; Liu, X.; Singh, B.; van Genderen, A. M.; Robledo-Padilla, F.; Parra-Saldivar, R.; Hu, N.; Jia, W.; Xu, C.; Kang, J.; Hassan, S.; Cheng, H.; Hou, X.; Khademhosseini, A.; Zhang, Y. S. *Adv. Mater.* **2018**, *30* (43), 1706913.
- (10) Ali, M.; Yoo, J. J.; Zahran, F.; Atala, A.; Lee, S. J. *Adv Healthc Mater.* **2019**, *8* (7), 1800992.
- (11) Pati, F.; Jang, J.; Ha, D.-H.; Kim, S. W.; Rhie, J.-W.; Shim, J.-H.; Kim, D.-H.; Cho, D.-W. *Nat. Commun.* **2014**, *5*, 3935.
- (12) Wang, Z.; Lee, S. J.; Cheng, H.-J.; Yoo, J. J.; Atala, A. *Acta Biomater.* **2018**, *70*, 48–56.



- (13) Zhang, Y. S.; Arneri, A.; Bersini, S.; Shin, S.-R.; Zhu, K.; Goli-Malekabadi, Z.; Aleman, J.; Colosi, C.; Busignani, F.; Dell'Erba, V.; Bishop, C.; Shupe, T.; Demarchi, D.; Moretti, M.; Rasponi, M.; Dokmeci, M. R.; Atala, A.; Khademhosseini, A. *Biomaterials* **2016**, *110*, 45–59.
- (14) Lote, C. J. *Principles of Renal Physiology*, **2012**, Springer, New York.
- (15) Homan, K. A.; Kolesky, D. B.; Skylar-Scott, M. A.; Herrmann, J.; Obuobi, H.; Moisan, A.; Lewis, J. A. *Sci Rep.* **2016**, *6*, 34845.
- (16) Lin, N. Y.; Homan, K. A.; Robinson, S. S.; Kolesky, D. B.; Duarte, N.; Moisan, A.; Lewis, J. A. *Proc. Natl. Acad. Sci.* **2019**, *116* (12), 5399–5404.
- (17) Kullak-Ublick, G. A.; Andrade, R. J.; Merz, M.; End, P.; Benesic, A.; Gerbes, A. L.; Aithal, G. P. *Gut.* **2017**, *66* (6), 1154–1164.
- (18) Ma, X.; Qu, X.; Zhu, W.; Li, Y.-S.; Yuan, S.; Zhang, H.; Liu, J.; Wang, P.; Lai, C. S. E.; Zanella, F. *Proc. Natl. Acad. Sci.* **2016**, *113* (8), 2206–2211.
- (19) Nguyen, D. G.; Funk, J.; Robbins, J. B.; Crogan-Grundy, C.; Presnell, S. C.; Singer, T.; Roth, A. B. *PLoS One.* **2016**, *11* (7), e0158674.
- (20) Snyder, J.; Hamid, Q.; Wang, C.; Chang, R.; Emami, K.; Wu, H.; Sun, W. *Biofabrication* **2011**, *3* (3), 034112.
- (21) Bhise, N. S.; Manoharan, V.; Massa, S.; Tamayol, A.; Ghaderi, M.; Miscuglio, M.; Lang, Q.; Zhang, Y. S.; Shin, S. R.; Calzone, G. *Biofabrication* **2016**, *8* (1), 014101.
- (22) Madden, L. R.; Nguyen, T. V.; Garcia-Mojica, S.; Shah, V.; Le, A. V.; Peier, A.; Visconti, R.; Parker, E. M.; Presnell, S. C.; Nguyen, D. G.; Retting, K. N. *iScience* **2018**, *2*, 156–167.
- (23) Dai, X.; Ma, C.; Lan, Q.; Xu, T. *Biofabrication* **2016**, *8* (4), 045005.
- (24) Zhao, Y.; Yao, R.; Ouyang, L.; Ding, H.; Zhang, T.; Zhang, K.; Cheng, S.; Sun, W. *Biofabrication* **2014**, *6* (3), 035001.
- (25) Heinrich, M. A.; Bansal, R.; Lammers, T.; Zhang, Y. S.; Michel Schiffelers, R.; Prakash, J. *Adv. Mater.* **2019**, *31* (14), 1806590.
- (26) Xu, F.; Celli, J.; Rizvi, I.; Moon, S.; Hasan, T.; Demirci, U. *Biotechnol. J.* **2011**, *6* (2), 204–212.
- (27) Meng, F.; Meyer, C. M.; Joung, D.; Vallera, D. A.; McAlpine, M. C.; Panoskaltis-Mortari, A. *Adv. Mater.* **2019**, *31* (10), 1806899.
- (28) Richards, D.; Jia, J.; Yost, M.; Markwald, R.; Mei, Y. *Ann Biomed Eng.* **2017**, *45* (1), 132–147.

## Bioinks

### TissueFab™

Name	Bioburden (cfu/mL)	pH	Cat. No.
TissueFab™ - GelMA-UV bioink	<5	6.0 - 9.0	905429-1EA
TissueFab™ - GelMA-Vis	<5	6.0 - 9.0	906891-1EA
TissueFab™ - Sacrificial bioink	<5	6.0 - 9.0	906905-1EA
TissueFab™ - GelAlg-Vis	<5	6.0 - 9.0	906913-1EA
TissueFab™ - GelAlg-UV bioink	<5	6.0 - 9.0	905410-1EA

### Alginate Bioinks

Name	Endotoxin (EU/mL)	pH	Cat. No.
Alginate-RGD bioink	<25	6.5 - 7	901950-1EA
Cellulose-Alginate bioink	<25	6.5 - 7	901960-1EA
Cellulose-Alginate-RGD bioink	<25	6.5 - 7	901966-1EA
Cellulose-Alginate-Calcium Phosphate bioink	<25	6.5 - 7	901958-1EA
Alginate bioink	<25	6.5 - 7	901953-1EA

### Decellularized ECM Bioink Precursor

Description	Chemical Composition	Cat. No.
from porcine skin, suitable for 3D bioprinting applications	GAG 0.4-0.8 µg/mL Collagen 90-125 µg/mg	906867-1EA
from porcine cartilage, suitable for 3D bioprinting applications	GAG 2.0-6.0 µg/mL Collagen 60-120 µg/mL	906875-1EA
from porcine bone, suitable for 3D bioprinting applications	GAG 1.5-5.0 µg/mg Collagen 60-120 µg/mg	906883-1EA

## Natural Polymers for 3D Bioprinting

### Functionalized Gelatin

#### Gelatin Methacryloyl (GelMA)

Name	Gel Strength (Bloom)	Degree Of Substitution	Cat. No.
Gelatin methacryloyl	300 g	80%	900496-1G
	300 g	60%	900622-1G
	300 g	40%	900629-1G
	90-110 g	60%	900628-1G
	170-195 g	60%	900741-1G
Allyl-modified gelatin	300 g	70%	901553-1G
Thiol-modified gelatin	-	70%	904643-1G

## Gelatin

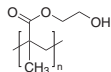
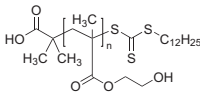
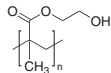
Name	Gel Strength (Bloom)	Endotoxin	Cat. No.
Low endotoxin gelatin from porcine skin	100 g	<10 EU/g	901757-5G 901757-1G
	260-300 g	<10 EU/g	901756-1G 901756-5G

## Collagen

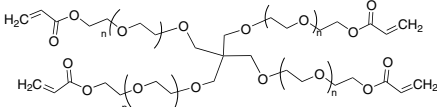
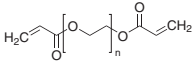
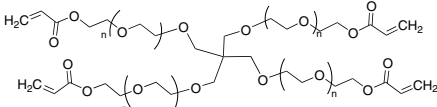
Name	Form	Endotoxin	Cat. No.
Bovine tendon	powder	<10 EU/g	900722-1EA
Bovine tendon	powder	<20 EU/g	900723-1EA
Bovine fibrillar	solution	<0.25 EU/mL	900721-1EA

## Synthetic Polymers for 3D Bioprinting

### Poly(hydroxyethyl methacrylate)

Name	Structure	Molecular Weight	Cat. No.
Poly(2-hydroxyethyl methacrylate)		average $M_v$ 20,000	529265-5G 529265-25G
		average $M_v$ 1,000,000	529257-1G 529257-10G
Poly(hydroxyethyl methacrylate), DDMAT terminated		average $M_n$ 7,000	772542-1G
Poly(2-hydroxyethyl methacrylate)		average $M_v$ 300,000	192066-10G 192066-25G

### Poly(ethylene glycol)

Name	Structure	Molecular Weight	Cat. No.
4arm-PEG20K-Acrylate		average $M_n$ 20,000	JKA7034-1G
8-arm PEG5K-Acrylate (tripentaerythritol core)	$R \left[ \text{O} \left( \text{CH}_2 \right)_n \text{O} \left( \text{CH}_2 \right)_m \text{O} \right]_8$ R = Tripentaerythritol core structure	average $M_n$ 5,000	JKA10055-1G
8-arm PEG5K-Acrylate (hexaglycerol core)	$R \left[ \text{O} \left( \text{CH}_2 \right)_n \text{O} \left( \text{CH}_2 \right)_m \text{O} \right]_8$ R = Hexaglycerol core structure	average $M_n$ 5,000	JKA8062-1G
8-arm PEG5K-Methacrylate (hexaglycerol core)	$R \left[ \text{O} \left( \text{CH}_2 \right)_n \text{O} \left( \text{CH}_2 \right)_m \text{O} \right]_8$ R = Hexaglycerol core structure	average $M_n$ 5,000	JKA8063-1G
8-arm PEG5K-Methacrylate (tripentaerythritol core)	$R \left[ \text{O} \left( \text{CH}_2 \right)_n \text{O} \left( \text{CH}_2 \right)_m \text{O} \right]_8$ R = Tripentaerythritol core structure	average $M_n$ 5,000	JKA10056-1G
8-arm PEG10K-Methacrylate (hexaglycerol core)	$R \left[ \text{O} \left( \text{CH}_2 \right)_n \text{O} \left( \text{CH}_2 \right)_m \text{O} \right]_8$ R = Hexaglycerol core structure	average $M_n$ 10,000	JKA8064-1G
8-arm PEG10K-Methacrylate (tripentaerythritol core)	$R \left[ \text{O} \left( \text{CH}_2 \right)_n \text{O} \left( \text{CH}_2 \right)_m \text{O} \right]_8$ R = Tripentaerythritol core structure	average $M_n$ 10,000	JKA10057-1G
Poly(ethylene glycol) diacrylate		average $M_n$ 2,000	701971-1G
		PEG average $M_n$ 20,000 ( $n \sim 450$ ) average $M_n$ 20,000	767549-1G
4arm-PEG10K-Acrylate		average $M_n$ 10,000	JKA7068-1G



# Nanoparticle-Based Drug and Gene Delivery for Tumor Targeting



Takeshi Mori, Akihiro Kishimura, and Yoshiki Katayama\*

Department of Chemistry and Biochemistry, Faculty of Engineering, Kyushu University, Japan  
\*E-mail: ykatatcm@mail.cstm.kyushu-u.ac.jp



## Introduction

Cancer is a leading cause of death worldwide. If detected early, surgical resection can be a highly effective treatment. But for metastatic cancers or tumors in difficult-to-resect sites, chemotherapy remains the most promising option. However, the response rate of tumors to chemotherapy can be as low as 10–20%, and limited by low delivery efficiency<sup>1</sup> and there are severe side effects caused by drug delivery to other sites, even for targeted therapies. In this sense, better tumor-targeting drug or gene delivery strategies are needed to deliver significant improvements for patients.

In 1986, Maeda et al. discovered tumor neovasculature shows enhanced leakage, or extravasation of serum albumin or other molecules.<sup>2</sup> Driven by incomplete endothelium formation and poor development of lymphatics, macromolecules of more than 40 kDa leak from the blood vessel and selectively accumulate in tumor sites. This phenomenon, known as enhanced permeability and retention (EPR) effect, allows for a number of versatile strategies to create tumor-selective drug delivery systems,<sup>3</sup> and nanoparticles have been investigated as tumor-targeting drug delivery systems utilizing this effect. Nanosized anticancer drugs are large enough to escape renal clearance and avoid penetration of the tight endothelial junctions of normal blood vessels, yet small enough to extravasate in leaky tumor vasculatures and selectively accumulate in tumor tissues, making them ideal for EPR-based selective anticancer therapy.<sup>4</sup> This paper discusses recent advances in these systems and strategies.

## Augmentation of the EPR Effect

The EPR effect is one of the most effective ways to target a tumor site, and effective accumulation of nanoparticles at tumor sites is commonly observed in murine model systems. However, only 1% of human clinical studies have demonstrated effective use of the EPR effect by nanoparticle delivery systems.<sup>5</sup> In fact, the poor progression of the lymph system in many tumors causes high interstitial fluid pressure which suppresses extravasation. As a result, selective delivery of a drug to the tumor site by the EPR effect using nanoparticle systems is hindered. To resolve this issue, other strategies have been developed to augment EPR effect, thereby allowing selective accumulation of therapeutic agents at tumor sites.

As previously discussed, an effective delivery system approach to enable extravasation is to overcome the high interstitial fluid pressure at the tumor site. In normal tissues this pressure is usually 3–10 mm Hg, but can be as high as 40–60 mm Hg in tumor tissue.<sup>6</sup> Salnikov et al. used Prostaglandin E1 for fluid pressure control, and reported a 40% enhancement of 5-FU accumulation at tumor sites (**Figure 1A**).<sup>7</sup> Another strategy is to increase systolic blood pressure, and Maeda et al. reported angiotensin-induced hypertension chemotherapy, which led to increased nanoparticle accumulation in tumors (**Figure 1B**).<sup>8</sup> However, selectively controlling blood flow in tumor vasculature is challenging, and such methods can induce systemic adverse effects such as a cardiovascular event.<sup>9</sup> Nanoparticles that offer controlled release of vasodilators (medications that dilate blood vessels) are a promising resolution. For example, spontaneous

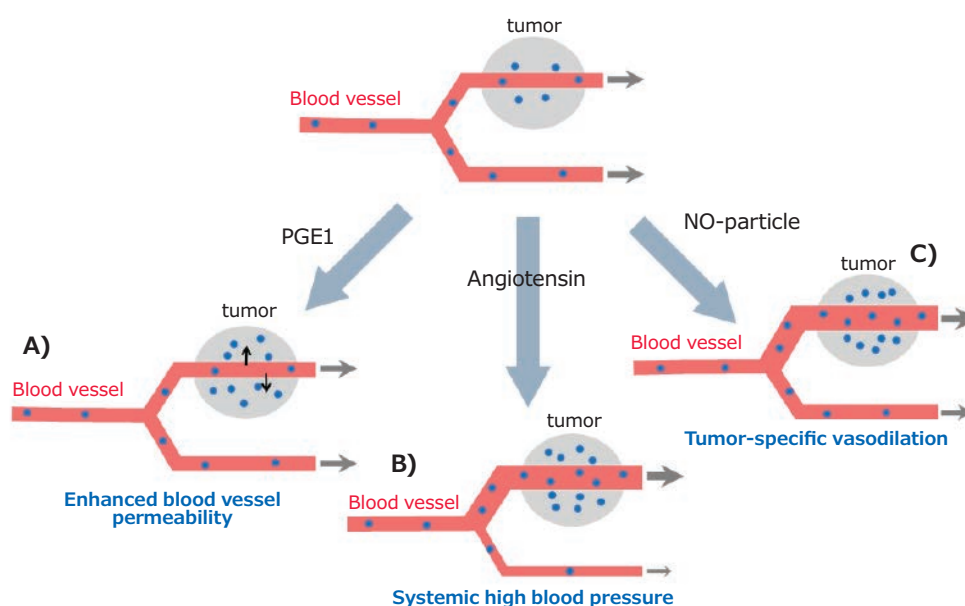


**Figure 1.** Strategies of Enhancement in EPR effect. **A)** PEG1 administration causes amplification of blood vessel permeability. **B)** Angiotensin administration cause systemic high blood pressure, but cancer neovasculature has poor response to angiotensin. **C)** NO-releasing carriers causes cancer neovasculature-specific vasodilation.

nitric oxide (NO) releaser (NOC-18) encapsulated liposomes have been investigated for enhancing the EPR effect.<sup>10</sup> After liposomes are absorbed by tumor sites by the EPR effect, NOC-18 gradually releases NO which, in turn, induces vasodilation, thereby achieving selective vasodilation in cancer neovasculatures. This resulted in enhanced accumulation of drug accumulation selectively at tumor sites (**Figure 1C**). Similarly, researchers used S-nitrosothiol-incorporated serum albumin as the macromolecular vasodilator<sup>11</sup> to achieve localized vasodilation and two to five fold enhanced particle accumulation at tumor sites.

### Stimuli-Responsive Systems for Nanoparticle-Based Delivery

Although EPR-enhanced systems improve the pharmacological distribution of a therapeutic drug or gene while also decreasing the effective dosage required, sometimes there can also be higher accumulation in the liver or other organs. To address this issue, stimuli responsive drug release systems that occur selectively in the target tumor tissue are being investigated. Such systems aim to increase the drug concentration ratio between the target site and other normal organs and tissues.

Several different stimuli-responsive carriers have been developed for improved drug release specifically in tumor sites. Since solid tumors form a characteristic microenvironment that is quite different from normal tissue, many of these systems use tumor microenvironment factors as a trigger to release the drug payload. For example, tumor tissue initially produces high concentrations of lactic acid, lowering the pH of the tumor microenvironment to 5.85–7.68, from a normal mean pH value

of 7.52.<sup>12</sup> Vigorous proliferation of tumor cells tends to cause hypoxia, which leads to the expression of a special transcription factor (HIF-1) to counteract it. Tumor cells also contain a much higher level of glutathione (GSH, 2–10 mM) than normal cells, in order to vanish reactive oxygen species produced by their high metabolic activity.<sup>13</sup> The tumor microenvironment also induces various enzymes including matrix metalloproteases (MMP),  $\beta$ -glucuronidase, hyaluronidase and urokinase plasminogen activator, as well as abnormal activation of some kinases and transcription factors.<sup>1</sup> These proteins are essential to for tumor progression, metastasis, and invasion. Any one of these factors could be used to stimulate of drug release in a tumor selective system. Some examples of such stimuli-responsive systems are described below.

### pH-Responsive System

The lower pH at tumor sites is the most commonly exploited stimuli in tumor-specific drug delivery systems (DDS). In addition to the acidic pH found in tumor tissues, endosomal pH (pH 5.5–6) can also be used to accelerate drug release from carriers. Because nanoparticles are taken up by tumor cells by endocytosis, rapidly decreased endosomal pH can also be used to trigger drug release in the cytosol, causing a rapid increase of drug concentration in the cytosol. Thus, pH-responsive carriers cause a rapid increase of drug concentration near and inside tumor cells.

There are two major strategies used to design pH-responsive carriers. One is the use of pH-responsive cleavage linkers in carrier molecules. Imine, cyclic orthoester, and acetal

bonds are all hydrolysable at mild acidic pH (**Figure 2A**).<sup>15</sup> These cleavable linkers can be incorporated into polymeric nanocarriers, allowing them to degrade and release therapeutic agents in the lower pH environment of the tumor. For example, a triblock copolymer consisting of PEG-oxime-tethered polycaprolactone-PEG triblock copolymer forms a core-shell type polymer micelle<sup>16</sup> in aqueous solution. The hydrophobic core of the nanoparticles rapidly decomposed at low pH in tumor tissue and triggered the release of encapsulated drugs. Another strategy is to use a weak base that can be protonated at lower pH. Chen et al. coated doxorubicin (DOX)-containing mesoporous silica nanoparticles with folic acid-PEG modified polydopamine.<sup>17</sup> Protonation of the coating polymer at acidic pH destabilized the coating layer and induced the release of DOX. Another example is methoxy-PEG-*b*-poly  $\epsilon$ -caprolactone-*b*-poly glutamate triblock copolymers, which form vesicles (polymersomes) in aqueous solution. Structural disintegration occurs at endosomal pH with the protonation of poly glutamate chain.<sup>18</sup> As for gene delivery, the pH buffering effect is commonly adopted for the acceleration of endosomal release of gene cargo (**Figure 2B**). Protonation of the gene delivery carriers inside the endosomes induced the influx of counterions and water, leading to osmotic pressure increase and eventually endosome breakage and content release. This is known as the proton sponge effect.<sup>19</sup> Polyethylenimine (PEI) derivatives are the most common example of such gene carriers.<sup>20</sup>

pH-dependent changes in peptide conformation can also be used to create pH-responsive systems. Bacteriorhodopsin C helix-derived peptides assume cell-penetrating  $\alpha$ -helix conformation at weakly acidic conditions, enhancing cell uptake of the nanoparticles in tumor tissue.<sup>21</sup>

### Redox-Responsive Systems

High glutathione (GSH) concentration at tumor sites is another common signal for redox-responsive DDS (**Figure 3B**). Polymeric carriers containing disulfide linkages have been developed for drug and gene delivery. For example, PEG-*b*-poly-L-lysine-SS-polycaprolactone was designed and used to form polymeric vesicles and encapsulate DOX and Verapamil into its inner aqueous phase and hydrophobic shell, respectively.<sup>23</sup> The disulfide bonds inside vesicles could be reversibly cleaved in a reductive environment, thus triggering the release of the encapsulated drugs. Similarly, researchers have shown that polymersome formed from poly-Z-L-lysine-SS-PEG-SS-poly-Z-L-lysine triblock copolymer selectively released DOX in tumor cells, whereas the release was suppressed in normal cells.<sup>24</sup> This GSH-based redox-responsive strategy has also been adopted for gene delivery systems. Researchers have demonstrated that nanoparticles consisting of PEI-*b*-cyclodextrin, adamantyl-SS-PEG, and adamantyl-PEG-SP94 (anti-CD7 antibody) could preferentially deliver miR34 (microRNA) to LM3HCC cancer cells and suppress their proliferation.<sup>25</sup>

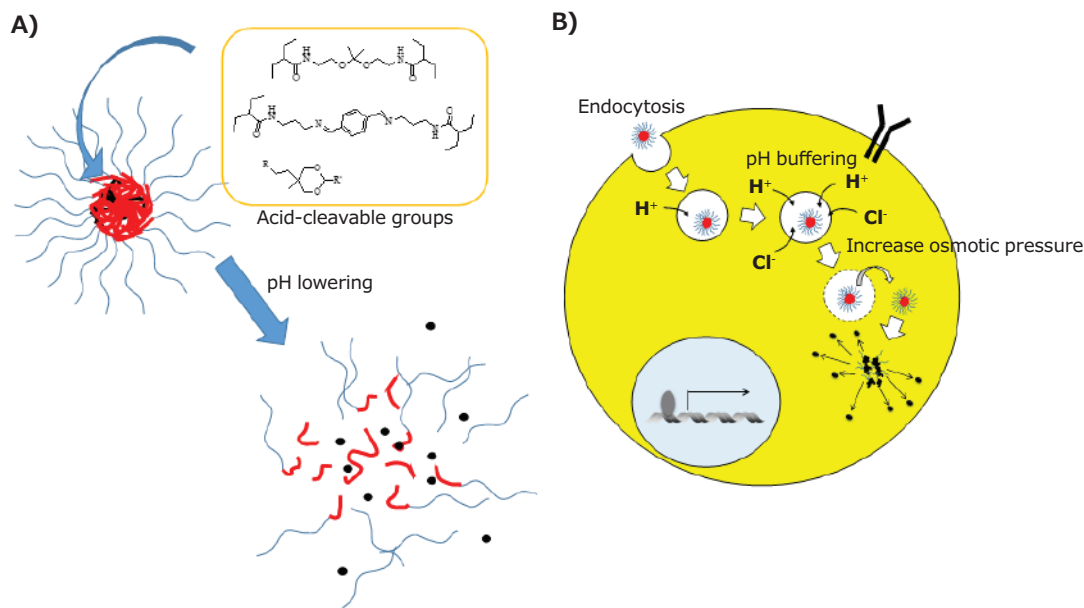


**Figure 2.** pH-responsive carriers. **A)** Acid-sensitive linkage inserted polymer micelle. **B)** Proton sponge effect of drug carriers using weak base units.

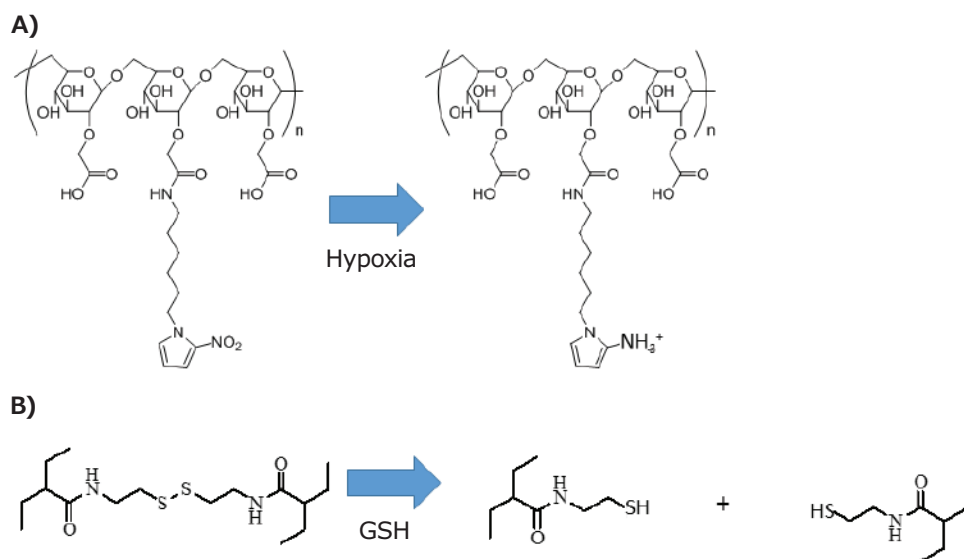


**Figure 3.** Redox-responsive carriers. A) Nitro-imidazol is reduced to amino-imidazol in hypoxic condition in tumor tissue. B) Disulfide linkage is cleaved with reduction by glutathione.

### Enzyme-Responsive systems

Many tumor tissues have high MMP-2/9 activity,<sup>26</sup> which has also been used as a signal for designing enzyme-responsive DDS. Researchers have developed solid lipid nanoparticles consisting of glycerol-monostearate, capric triglyceride, and phosphatidylcholine with a gelatin coating layer for the delivery of drugs.<sup>27</sup> At the tumor site, high MMP level degraded gelatin efficiently and induced the release of encapsulated drugs (Figure 4A), delivering them preferentially to the tumor site over normal tissue. Also, MMP cleavable linkers were used in core-shell type polymer micelles (Figure 4B). Specifically, hydrophilic shells such as PEG or avidin were connected with the core through an MMP substrate peptide linker, which was susceptible to high MMP concentration at the tumor site. At the tumor sites, the cleavage of the hydrophilic shell induced by high MMP concentration disrupted the drug nanocarrier, resulting in localized drug release at tumor tissues.<sup>28,29</sup> In another case, PEG2000-MMP2 substrate-PEI1800-dioleoylphosphatidylethanolamine was capable of co-encapsulating both Paclitaxel and siRNA. The cleavage of PEG by MMP2 was shown to accelerate the siRNA release at cancer sites (Figure 4C).<sup>28</sup> Also, PEG-MMP substrate cell penetrating peptide (CPP)-phospholipid was inserted onto a liposome membrane for improved cellular uptake.<sup>30</sup> The PEG part was cleavable by MMP in tumor tissue and the newly-exposed CPPs contributed to cell uptake of the particles (Figure 4D). Using the same concept, another group designed cationic CPP connecting oligoanionic peptides using an MMP substrate as the delivery vehicle. The electrostatic interaction between the CPP and the anionic sequence shielded the cell penetrating activity. Removal of the anionic sequence in the tumor by MMP cleavage also improved cellular uptake (Figure 4E).<sup>31</sup>

Intracellular enzymatic activity is also useful for cancer cell-specific payload release. Various protein kinases play

essential roles in tumor growth, survival and angiogenesis,<sup>32</sup> and are by definition absent in normal cells, so can be used as drug-releasing stimuli. For example, a cancer targeting gene delivery system has been designed using a protein kinase signal (Figure 4F).<sup>33</sup> Specifically, protein kinase-specific cationic peptide substrates were chosen and used to construct grafted polymers. The cationic peptide grafted polymer formed nanosized polyplexes with genetic materials through electrostatic interactions. At tumor sites, polymer side chains are phosphorylated by the abnormally-activated protein kinase. The negative charges introduced by phosphate groups weakened the interaction between the carrier and DNA, thereby triggering the release of the gene cargo. Furthermore, the kinase specificity of the delivery vehicle can be easily tuned by modifying the pendant peptide sequence. Various gene delivery systems responding to different protein kinases, such as protein kinase A, Src, I-k-kinase, Akt or protein kinase Ca (PKCa) have been developed for different tumor site targeting applications.<sup>34,35</sup>

### Physical Stimuli-Responsive System

Physical stimulations can also be used for stimuli-responsive DDS. Yang et al. reported on photo-responsive liposomes. They developed drug carrier molecules using a CPP peptide and phosphatidylethanolamine, with photo-cleavable linkers. CPP is shielded in blood circulation and normal tissue by its anionic sequence. Localized drug release was achieved by photo-irradiation of the tumor site, which cleaved the 2-nitro-4,5-dimethoxybenzyl group, inducing another intramolecular reaction, causing removal of the anionic peptide moiety and release of the therapeutic agent (Figure 5).<sup>36</sup> Despite the fact that light is a spatially and temporally controllable stimuli, this cleavage reaction requires near UV (usually less than 360 nm) light which cannot penetrate tissue.<sup>37</sup> For penetration into deeper tissue, a photocleavable reaction in near IR (650-900 nm) region is needed.<sup>38</sup>

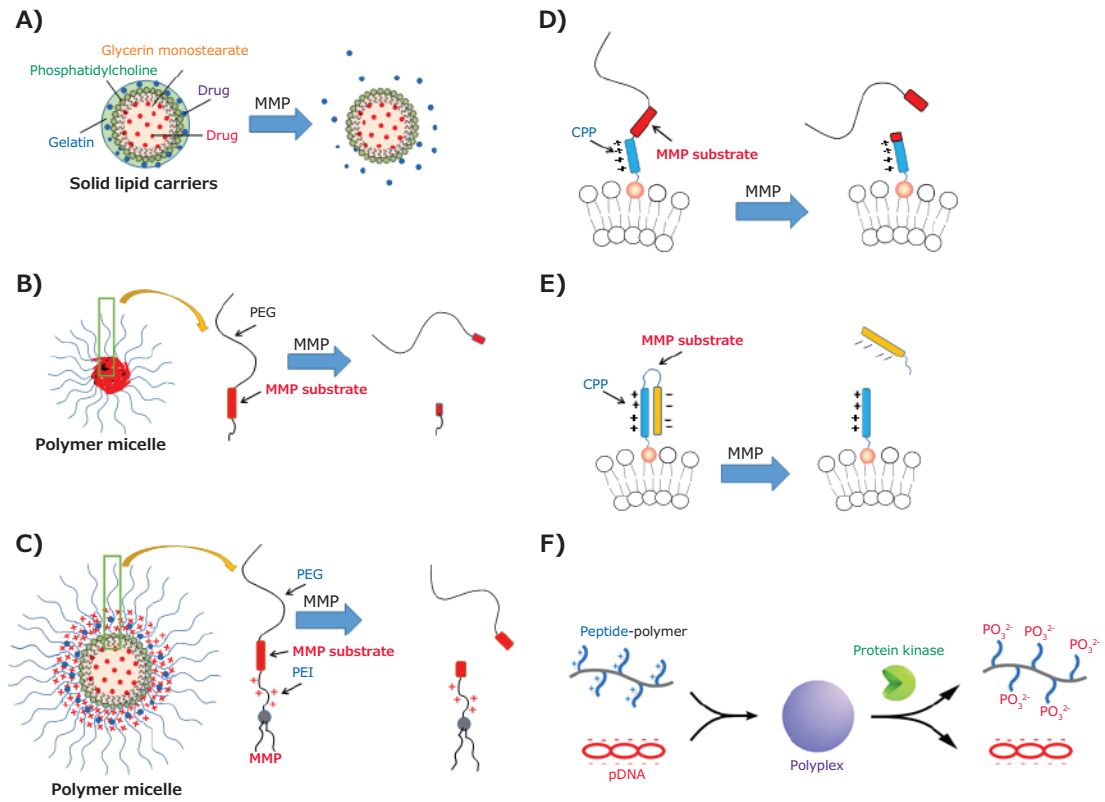


**Figure 4.** Enzyme-responsive carriers. **A)** Gelatin-coated solid lipid nanoparticle. **B)** PEG removal with MMP in polymer micelle. **C)** PEG removal and CCP expose with MMP in lipid coated nanoparticle. **D)** PEG removal with MMP in liposome. **E)** PEG removal and CCP expose with MMP in liposome. **F)** Protein kinase-responsive gene release.

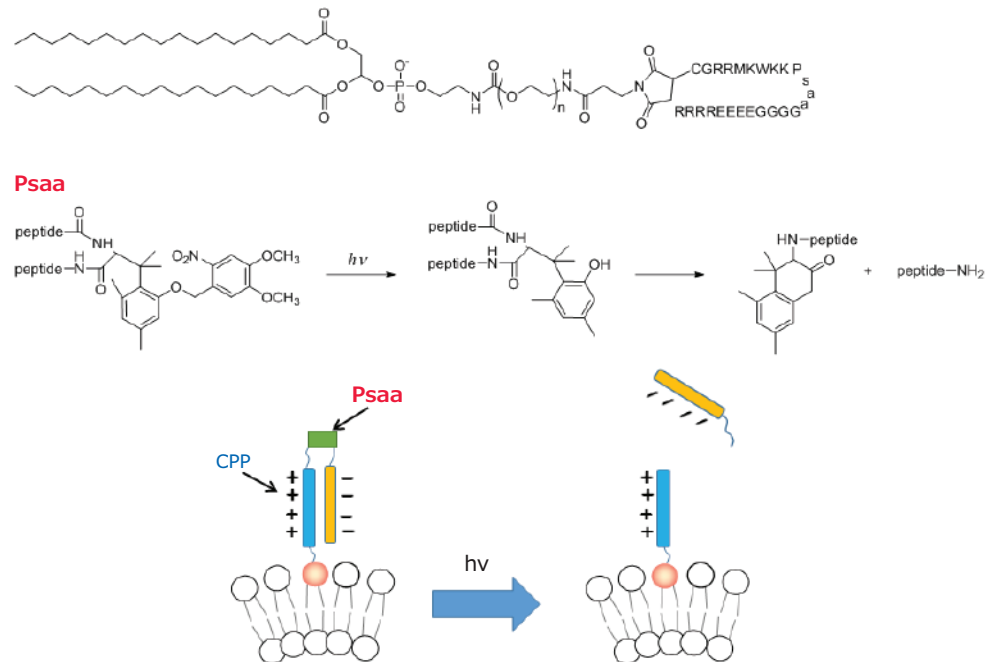


**Figure 5.** Photo-responsive carrier. Photo-irradiation causes the cleaving of oligo-anion peptide and CCP expose in liposome.



## Multi Stimuli-Responsive System

More sophisticated multi stimuli-responsive DDS are also being developed to achieve precise tumor targeting. An et al. proposed pH and redox dual-responsive drug delivery systems (Figure 6A).<sup>39</sup> They designed a novel poly(ethylene glycol)-*block*-poly(disulfide histamine) copolymer as a nanomaterial drug delivery carriers. When the nanocarriers reach the tumor tissue via the EPR effect, the imidazole moieties are protonated at the weakly acidic pH, improving the endocytotic cellular uptake efficiency. The high concentration of GSH reduces the disulfide bonds in the polymer and disrupts the nanoparticle structure, resulting in rapid increase of the drug concentration near the nucleus of tumor cells.

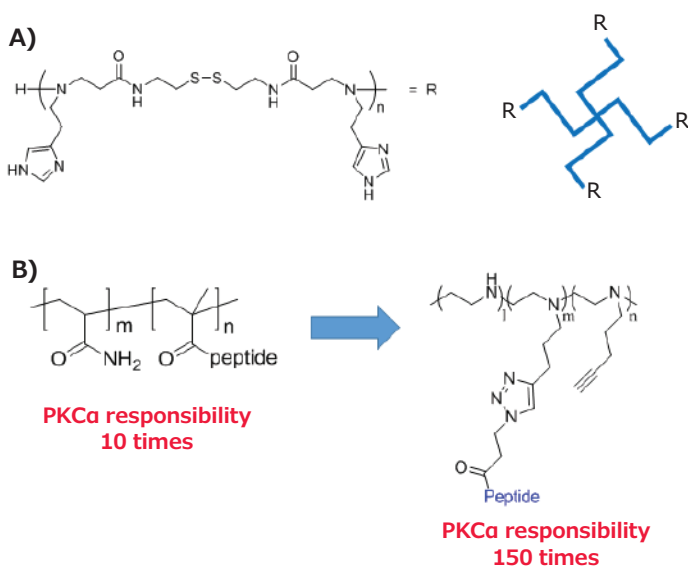


**Figure 6.** Multistimuli-responsive carriers. A) pH and redox responsive carrier. B) pH and protein kinase responsive carrier.

In addition, pH and kinase dual-responsive systems have been designed by simply converting the polymer backbone from a neutral polymer to PEI (Figure 6B).<sup>40</sup> The additional proton sponge effect results in an improved endosome escape efficiency of the polyplex with DNA. Consequently, PKCa delivery increases from 10 to 500 times when compared to the expression level in a non-PKCa responsive system using a control peptide.

## Conclusion

Drug and gene delivery systems using nanoparticles have great potential to target the delivery of therapeutic or diagnostic agents. However, there are still issues in clinical applications because of poor methodology, instability, biocompatibility, degradability, complicated formulations, and lack of standardization. Also, nanoparticle systems sometimes show unexpected toxicity or inefficiency. In fact, some systems have failed clinical trials due to unexpected instability or lack of tumor-specific targeting despite their superiority to ordinary therapeutics in murine models. Developing new materials for drug carriers, as well as new evaluation methods and strategies, are crucial steps for the continued advancement of human tumor targeting.

## References

- Schiller, J. H.; Harrington, D.; Belani, C. P.; Langer, C.; Sandler, A.; Krook, J.; Zhu, J.; Johnson, D. H. *N. Engl. J. Med.* **2002**, *346* (2), 92–98.
- Matsumura, Y.; Maeda, H. *Cancer Res.* **1986**, *46*, 6387–6392.
- Maeda, H. *Adv. Drug Deliv. Rev.* **2015**, *91*, 3–6.
- Greish, K. In: Grobmyer, S.; Moudgil, B. (eds) *Cancer Nanotechnology. Methods in Molecular Biology (Methods and Protocols)*, vol 624. Humana Press.
- Wilhelm, S.; Tavare, A. J.; Dai, Q.; Ohta, S.; Audet, J.; Dvorak, H. F.; Chan, W. C. W. *Nat. Rev. Mater.* **2016**, *1* (5), 16014–16025.
- Omidi, Y.; Barar, J. *Bioimpacts* **2014**, *4*, 55–67.
- Salnikov, A. V.; Iversen, W.; Koisti, M.; Sundberg, C.; Johansson, L.; Stuhr, L. B.; Sjoquist, M.; Ahlstrom, H.; Rees, R. K.; Rubin, K. *FASEB J.* **2003**, *17* (12), 1756–1758.
- Fang, J.; Nakamura, H.; Maeda, H. *Adv. Drug Deliv. Rev.* **2011**, *63* (3), 136–151.
- Lewis, A. B.; Freed, M. D.; Heymann, M. A.; Roehl, S. L.; Keney, R. C. *Circulation* **1981**, *64* (5), 893–898.
- Tahara, Y.; Yoshikawa, T.; Sato, H.; Mori, Y.; Hosain, Z.; Kishimura, A.; Mori, T.; Katayama, Y. *Med. Chem. Comm.* **2017**, *8*, 415–421.
- Kinoshita, R.; Ishima, Y.; Chuang, Y. T. G.; Nakamura, H.; Fang, J.; Watanabe, H.; Shimizu, T.; Okuhira, K.; Ishida, T.; Maeda, H.; Otagiri, M.; Maruyama, T. *Biomaterials* **2017**, *140*, 162–169.
- Wike-Hooley, J. L.; Haveman, J. L.; Reinhold, H. S. *Radiotherapy and Oncology* **1984**, *2*, 343–366.
- Cheng, R.; Feng, F.; Meng, C.; Feijen, J.; Zhong, Z. *J. Control. Release* **2011**, *152* (1), 2–12.
- Huang, S.; Shao, K.; Kuang, Y.; Liu, Y.; Li, J.; An, S.; Guo, Y.; Ma, H.; He, X.; Jiang, C. *Biomaterials* **2013**, *34*, 5294–5302.
- Binauld, S.; Stenzel, M. H.; *Chem. Commun.* **2013**, *49*, 2082–2102.
- Jin, Y.; Song, L.; Su, Y.; Zhu, L.; Pang, Y.; Qiu, F.; Tomg, G.; Yan, D.; Zhu, B.; Zhu, X. *Biomacromolecules* **2011**, *12*, 3460–3465.
- Cheng, W.; Nie, J.; Xu L., Liang, C., Peng, Y., Liu, G., Wang, T., Mei L., Huang L., Zeng X. *ACS Appl. Mater. Interfaces* **2017**, *9* (22), 18462–18473.
- Zhao, L.; Zhang, X.; Liu, X.; Luan, Y. *Polym. Int.* **2017**, *66*, 1579–1586.
- Benjaminsen, R. V.; Matthebjerg, M. A.; Henriksen, J. R.; Moghimi, S. M.; Andresen, T. L. *Mol. Ther.* **2013**, *21* (1), 149–157.
- Benjaminsen, R. V.; Matthebjerg, M. A.; Henriksen, J. R.; Moghimi, S. M.; Andresen, T. L. *Mol Ther.* **2013**, *21* (1), 149–157.
- Andreev, O. A.; Dupuy, A. D.; Segala, M.; Sandugu, S.; Serra, D. A.; Chichester, C. O.; Engelman, D. M.; Reshetnyak, Y. K. *Proc. Natl. Acad. Sci. USA* **2007**, *104*, 7893–7898.
- Thambi, T.; Deepagan, V. J.; Yoon, H. Y.; Han, H. S.; Kim, S.-H.; Son, S.; Jo, D.-G.; Ahn, C.-H.; Suh, Y. D.; Kim, K.; Kwon, I.-C.; Lee, D. S.; Park, J. H. *Biomaterials* **2014**, *35* (5), 1735–1743.
- Thambi, T.; Deepagan, V. J.; Ko, H.; Lee, D. S.; Park, J. H. *Mater. Chem.* **2012**, *22*, 22028–22036.
- Ren, T.; Wu, W.; Jia, M.; Dong, H.; Li, Y.; Ou, Z. *ACS Appl. Mater. Interfaces* **2013**, 10721–10730.
- Hu, Q.; Wang, K.; Sun, X.; Li, Y.; Fu, Q.; Liang, T.; Tang, G. *Biomaterials* **2016**, *104*, 192–200.
- Waas, E. T.; Lomme, R. M. L. M.; DeGroot, J.; Wobbes, T.; Hendriks, T. *Br. J. Cancer* **2002**, *86* (12), 1876–1883.
- Gao, X.; Zhang, J.; Huang, Z.; Zuo, T.; Lu, Q.; Wu, G.; Shen, Q. *ACS Appl. Mater. Interfaces* **2017**, *9* (35), 29457–29468.
- van Rijt, S. H.; Böllükbass, D. A.; Argyo, C.; Datz, S.; Lindner, M.; Eickelberg, O.; Königshoff, M.; Bein, T.; Meiners, S. *ACS Nano* **2015**, *9* (3), 2377–2389.
- Zhu, L.; Perche, F.; Wang, T.; Torchilin, V. P. *Biomaterials* **2014**, *35*, 4213–4222.
- Smith, S. R.; Sewell, S. L.; Giorgio, T. D. *Int. J. Nanomed.* **2008**, *3*, 95–103.
- Goun, E. A.; Shinde, R.; Dehnert, K. W.; Adam-Bond, A.; Wender, P. A.; Contag, C. H.; Frans, B. L.; *Bioconjugate Chem.* **2006**, *17*, 787–796.
- Shchemelinin, I.; Sefc, L.; Necas, E. *Folia Biol (Praha)* **2006**, *52* (3), 81–100.
- Kang, J.-H.; Asai, D.; Kim, J.-H.; Mori, T.; Toita, R.; Tomiyama, T.; Asami, Y.; Oishi, J.; Sato, Y. T.; Niidome, T.; Jun, B.; Nakashima, H.; Katayama, Y. *J. Am. Chem. Soc.* **2008**, *130*, 14906–14907.
- Katayama, Y. *Bull. Chem. Soc. Jpn.* **2018**, *90* (1), 12–21.
- Kang, J.-H.; Asai, D.; Kim, J.-H.; Mori, T.; Toita, R.; Tomiyama, T.; Asami, Y.; Oishi, J.; Sato, Y. T.; Niidome, T.; Jun, B.; Nakashima, H.; Katayama, Y. *J. Am. Chem. Soc.* **2008**, *130*, 14906–14907.
- Yang, Y.; Xie, X.; Yang, Y.; Li, Z.; Yu, F.; Gong, W.; Li, Y.; Zhang, H.; Wang, Z.; Mei, X. *Mol. Pharm.* **2016**, *13*, 1508–1519.
- Furuta, T. *J. Synth. Org. Chem., Jpn.* **2012**, *70* (11), 1164–1169.
- Smith, A. M.; Mancini, M. C.; Nie, S. *Nat Nanotechnol.* **2009**, *4* (11), 710–711.
- An, K.; Zhao, P.; Lin, C.; Liu, H. *Int. Mol. Sci.* **2014**, *15*, 9067–9081.
- Toita, R.; Kang, J.-H.; Tomiyama, T.; Kim, C.-W.; Shiosaki, S.; Niidome, T.; Mori, T.; Katayama, Y. *J. Am. Chem. Soc.* **2012**, *134*, 1540–15417.

## Polyethyleneimine

### Polyethyleneimine, Branched

Name	Structure	Molecular Weight	Cat. No.
Polyethylenimine, branched		average $M_n \sim 10,000$ by GPC average $M_w \sim 25,000$ by LS	408727-100ML 408727-250ML 408727-1L
Poly(ethyleneimine) solution		$M_f$ 600,000-1,000,000 average $M_n \sim 1,200$ average $M_w \sim 1300$ by LS average $M_n \sim 60,000$ by GPC average $M_w \sim 750,000$ by LS	03880-100ML 03880-500ML 482595-100ML 482595-250ML 181978-5G 181978-100G 181978-250G 181978-18KG
Polyethylenimine, branched		average $M_w \sim 270,000$ by LS $\sim 90$ kDa by LS	904759-100G 904759-250G 904759-1KG

### Polyethyleneimine, Linear

Name	Structure	Molecular Weight	Cat. No.
Polyethylenimine, linear		average $M_n$ 5,000 average $M_n$ 2,500 average $M_n$ 10,000	764582-1G 764604-1G 765090-1G

### Polyethyleneimine Derivatives

Name	Structure	Molecular Weight	Cat. No.
Branched PEI-g-PEG		PEG $M_n$ 550	900926-1G
Stearic acid-modified branched polyethylenimine		-	900946-1G
Branched PEI-g-PEG		PEG $M_n$ 5,000	900743-1G

# THE FUTURE OF BIOIMAGING

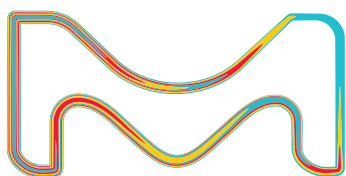
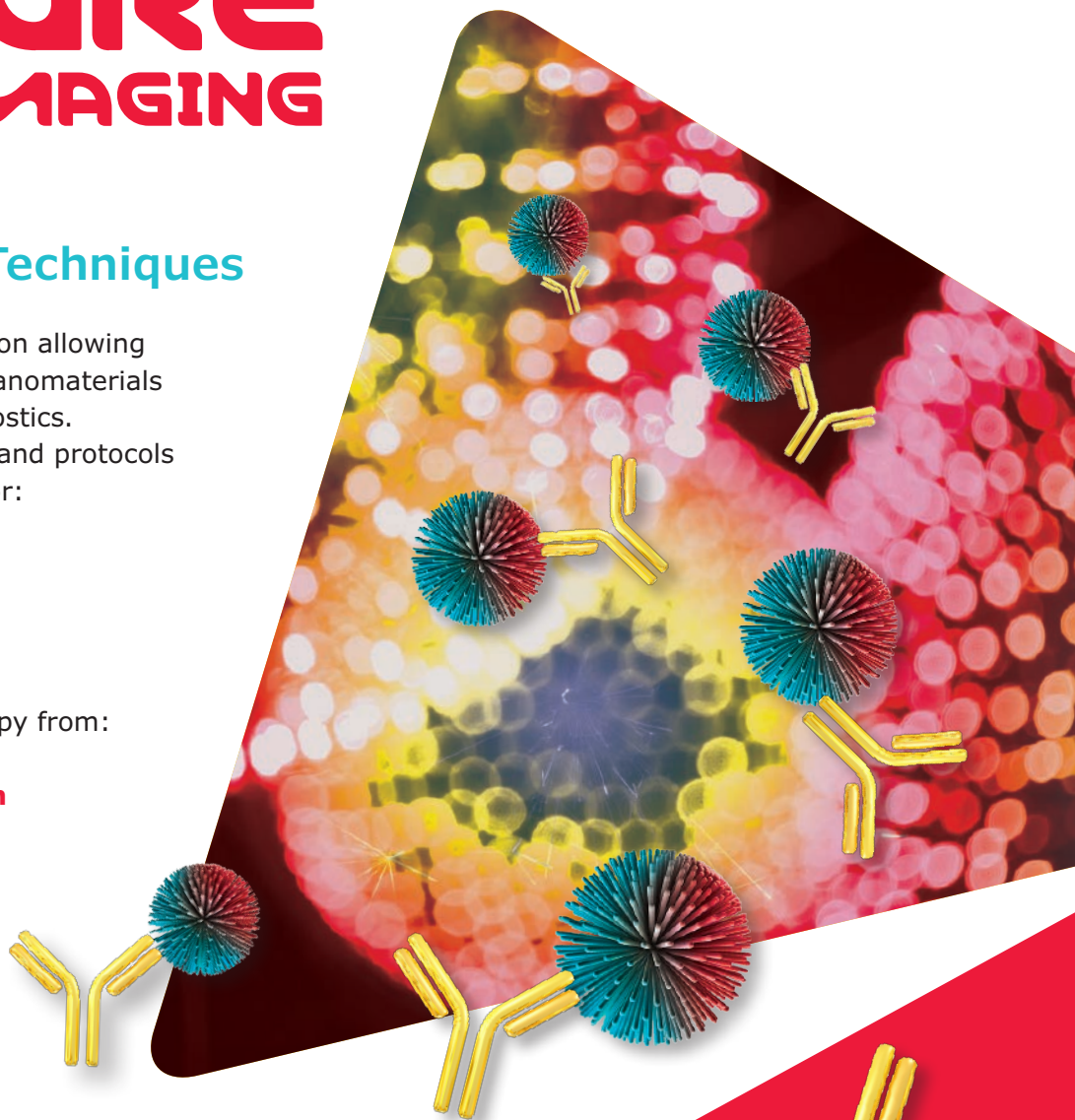
## Nanomaterial Bioconjugation Techniques

A guide for surface modification allowing bioconjugation of inorganic nanomaterials having applications in theranostics. Discover the latest advances and protocols in nanoparticle conjugation for:

- Magnetic Imaging
- Fluorescence Imaging
- Optical-based Imaging

Order your complimentary copy from:

[SigmaAldrich.com/  
nanomaterials-conjugation](http://SigmaAldrich.com/nanomaterials-conjugation)



The life science  
business of Merck  
KGaA, Darmstadt,  
Germany operates as  
MilliporeSigma in the  
U.S. and Canada.

**Sigma-Aldrich®**  
Lab & Production Materials

# Smart Oligonucleotide Delivery by Multifunctional Block Copolymers



Kotaro Hayashi,<sup>1</sup> Kanjiro Miyata<sup>2\*</sup>

<sup>1</sup>Innovation Center of NanoMedicine, Kawasaki Institute of Industrial Promotion, Tonomachi, Kawasaki-ku, Kawasaki, Japan.

<sup>2</sup>Department of Materials Engineering, Graduate School of Engineering, The University of Tokyo, Hongo, Bunkyo-ku, Tokyo, Japan

\*E-mail: miyata@bmw.t.u-tokyo.ac.jp

## Introduction

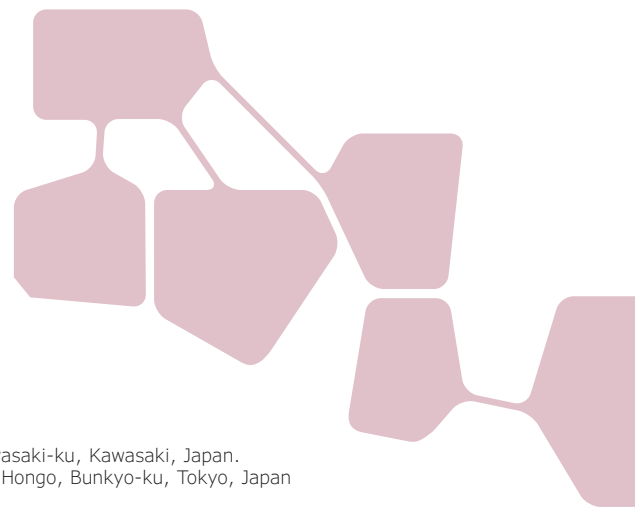
Over the past two decades, polymeric materials have been extensively developed for use as delivery vehicles for small nucleic acids or oligonucleotides such as antisense oligonucleotides (ASO) or small interfering RNA (siRNA).<sup>1,2</sup> This application of polymeric materials was made possible by the tendency of polycations to electrostatically associate with anionic oligonucleotides in aqueous media to form a nanocomplex, called polyion complexes (PICs) or polyplexes. These PICs protect oligonucleotides from enzymatic degradation and promote their cellular uptake (or adsorptive endocytosis), because the positively charged PIC domain binds to the negatively charged cellular membrane. Notably, chemical modifications of the component polycations can dramatically affect the performance of PICs, which has motivated polymer chemists and engineers to create and test a wide variety of polymers by focusing on biological-environment-responsive chemistry and biocompatibility.<sup>3</sup> This work highlights the main features of oligonucleotide-loaded PICs and the current chemical approaches for multifunctionalization of PICs, with the aim of “smart” oligonucleotide delivery.

## PIC Formation Between Oligonucleotides and Polycations

Poly(L-lysine) (PLys) is one of the most commonly used polycations for preparing oligonucleotide-loaded PICs, both because it is biodegradable and because its pendent primary amines are easily accessible for chemical modifications. PLys with a degree of polymerization (DP) of ~40 can effectively assemble into PICs with oligonucleotides via charge

neutralization at approximately charge-equivalent mixing ratios, i.e., an  $[\text{NH}_3^+ \text{ in PLys}]$ -to- $[\text{PO}_3^- \text{ in oligonucleotide}]$  ratio of approximately 1:1.<sup>4</sup> A slight excess of PLys can generate positively charged PICs, which is advantageous for adsorptive endocytosis under typical cell culture conditions. However, positively charged nanoparticles often undergo nonspecific protein adsorption, resulting in the formation of larger aggregates. To avoid aggregate formation, nonionic and hydrophilic poly(ethylene glycol) (PEG) is often conjugated to PLys (or to the PIC surface).<sup>5</sup> Typically, diblock copolymers of PEG and PLys (PEG-PLys) are prepared through ring-opening polymerization of Lys(Z) *N*-carboxyanhydride from amine-terminated PEG (PEG-NH<sub>2</sub>) as a macroinitiator, followed by deprotection of the Z group to afford PEG-PLys.<sup>7</sup> The PEG layer sterically stabilizes PICs by attenuating both the interaction with charged biomacromolecules such as albumin, and the interaction with neighboring PICs.<sup>6</sup>

Recently, the PIC formation of PEG-PLys with single-stranded RNA (ssRNA) or double-stranded RNA (dsRNA) was found to follow two-step assembly behavior.<sup>8</sup> The primary association was found to be the formation of minimal charge-neutralized units (or unit PICs) comprised of RNA and PEG-PLys. The secondary association was found to be the multimolecular assembly of unit PICs toward micellar (or vesicular) PICs (**Figure 1A**). The combination of ssRNA (21-mer) and PEG-PLys (molecular weight (MW) of PEG: 2,000–42,000; DP of PLys: ~40) generated unit PICs with a 10 nm hydrodynamic diameter ( $D_{\text{H}}$ ) at concentrations less than 0.01 mg/mL. By contrast, at concentrations greater than the critical association concentration (CAC) of ~0.01 mg/



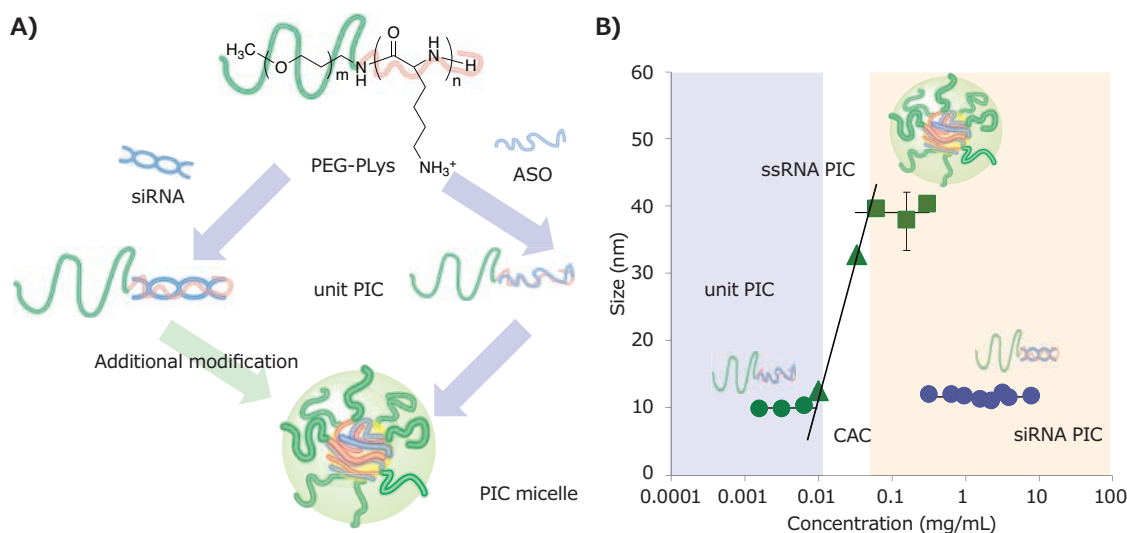


**Figure 1.** A) Schematic of various PIC formation behaviors between ssRNA (or ASO) and dsRNA (or siRNA) with PEG-PLys. B) Change in the hydrodynamic diameter of PICs prepared from ssRNA or dsRNA with PEG-PLys (MW of PEG: 12,000; DP of PLys: ~40) plotted as a function of concentration. Reprinted with permission from reference 8, copyright 2016 Wiley.

mL, 40 nm PICs, i.e., micellar PICs, were clearly observed, as shown in **Figure 1B**. This critical increase in size is similar to the conventional association behavior of amphiphilic macromolecules forming polymeric micelles.<sup>7</sup> However, the secondary association (or multimolecular assembly) was not observed between dsRNA (21-mer/21-mer) and the same PEG-PLys. Unit PICs with a diameter of 10 nm were prepared in a wide range of concentrations between 0.1 and 10 mg/mL (**Figure 1B**). The different PIC formation modes between ssRNA and dsRNA are explained by the difference in their rigidity: dsRNA has a persistence length of 60 nm and is thus considered a rigid cylindrical molecule, which likely hampers the multimolecular association of unit PICs by decreasing the entropic gain that accompanies the multimolecular association.<sup>8</sup>

On the basis of the PIC formation mode, either type of PICs, i.e., unit PICs or micellar PICs, can be used for delivery of oligonucleotide. We recently demonstrated the strong potential of unit PICs for *in vivo* systemic oligonucleotide delivery. A long, two-armed PEG-PLys (MW of PEG:  $2 \times 37$  kDa; DP of PLys: ~20) was designed to form 18 nm unit PICs comprised of a single molecule of siRNA or ASO. The PICs exhibited blood circulation stability and efficiently accumulated in murine models of fibrotic pancreatic cancer, presumably because of the excellent tissue permeability associated with their small size as well as the steric repulsive effect derived from the long, two-armed PEG.<sup>9</sup> Numerous previous studies have focused on micellar PICs, because their relatively larger size ( $40 \text{ nm} \leq D_H \leq 100 \text{ nm}$ ) allows them to avoid rapid renal clearance, which has a size threshold of  $\sim 10 \text{ nm}$ <sup>10</sup> when they are systemically administrated. In this regard, one of the most important criteria for polymer design is stability tuning of the micellar states. As previously discussed, multimolecular PICs are likely to dissociate into

smaller fragments of unit PICs under diluted conditions (or at concentrations below the CAC). Thus, additional stabilization is necessary to avoid micelle dissociation, but the oligonucleotide payloads ultimately need to be released from the PICs in the target cells. Thus, reversible stabilization of PICs is a prime challenge for systemic oligonucleotide delivery.

### Chemical Modifications of PEG-PLys for Reversible Stabilization of PICs

To attain micellar PICs with reversible stability, researchers have integrated biological-environment-responsive linkages into polymeric materials. For example, reduction-environment-responsive micellar PICs have been fabricated using thiolated PEG-PLys, which includes disulfide crosslinking in the micelle core. Disulfide-crosslinked micelles are relatively stable in nonreductive environments such as the bloodstream, but they are destabilized within the reductive cytoplasmic compartment because the disulfide bonds are cleaved, thereby enabling payload release. The thiolated PEG-PLys is synthesized by introducing thiol groups into PLys side chains using succinimidyl 3-(2-pyridyldithio)propionate (SPDP),<sup>11–13</sup> dimethyl-3,3'-dithiobispropionimidate (DTBP),<sup>14</sup> or 2-iminothiolane (IT)<sup>13,14</sup> (**Figure 2A**).

The SPDP-derived PEG-PLys (PEG-PLys(MP)) with 10–30% thiol moieties in the PLys side chains was mixed with single-stranded DNA (or ASO) in a buffer solution to form micellar PICs, followed by aerial oxidation to induce disulfide crosslinking in the micelle core. The disulfide-crosslinked micelles exhibited a  $D_H$  of 40 nm and greater tolerability under nonreductive diluted conditions than noncrosslinked control micelles, and they released the ASO payload under reductive conditions that mimicked the cytoplasm (1 mM glutathione).<sup>12</sup>



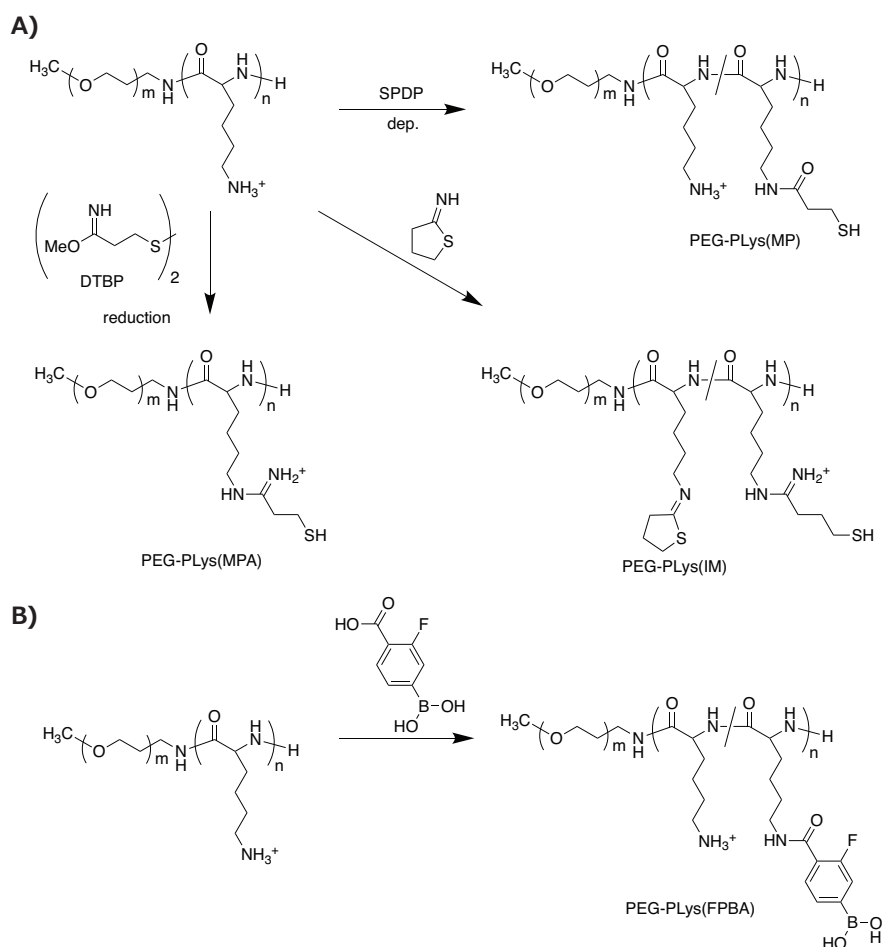


**Figure 2.** Functionalization of PEG-PLys for fabricating biological-environment-responsive micellar PICs. **A)** A series of thiolations of PEG-PLys for preparing disulfide-crosslinked micelles. **B)** Modification of PEG-PLys with phenylboronic acid for ATP-responsive micelle fabrication.

A similar crosslinking strategy was investigated for siRNA-loaded micellar PICs. “Rigid” siRNA-loaded micellar PICs were predicted to be less stable than the ASO-loaded micellar PICs. Thus, more thiol groups (~95% of PLys side chains) or additional stabilizing units were introduced into the PEG-PLys. To this end, DTBP was used instead of SPDP for thiolation of PEG-PLys because it provided a positively charged amidine group and a thiol group (PEG-PLys(MPA)) (**Figure 2A**). Using this method, the positively charged sites in the PLys segment were maintained even after such a high degree of thiolation. By contrast, modification with IT provided a closed-ring structure to the PLys segment with amidine and thiol groups (PEG-PLys(IM)) (**Figure 2A**). This ring structure substantially stabilized the siRNA-loaded micellar PICs, probably because of hydrophobic interactions and/or dipole-dipole interactions. Indeed, the micellar PICs prepared from PEG-PLys(IM) exhibited a substantially longer blood circulation time than those prepared from PEG-PLys(MPA).<sup>14</sup>

Another interesting approach is the direct, reversible conjugation of siRNA into the PIC core. Tetravalent 3-fluorophenylboronic acid (FPBA) formed a phenylboronate ester bond with a *cis*-diol moiety at physiological neutral pH.<sup>15</sup> Thus, FPBA-functionalized

PLys side chains (**Figure 2B**) can be covalently conjugated with the ribose ring at both 3' ends of siRNA.<sup>16</sup> Importantly, this covalent bond is reversible and can be replaced in the presence of a high concentration of *cis*-diol compounds, such as, adenosine triphosphate (ATP). When micellar PICs are prepared with PEG-PLys(FPBA) and siRNA, the siRNA payloads are covalently conjugated to the PLys side chains through the phenylboronate ester moiety in the PIC core, generating an siRNA-mediated crosslinked core. Although the FPBA-crosslinked micellar PIC was stable at low ATP concentrations (<0.3 mM, mimicking the extracellular milieu), it successfully dissociated in the presence of high concentrations of ATP (~3 mM, mimicking the cytoplasmic condition). Thus, reversible stabilization can also be achieved using PEG-PLys with phenylboronate functionality.

### Chemical Modifications of PEG-PLys for Targeted Oligonucleotide Delivery

The PEG layer of a micellar surface can attenuate nonspecific protein adsorption, although it can simultaneously compromise the adsorptive endocytosis (or cellular uptake) of the associated oligonucleotide payloads. To overcome this drawback,

functionalized micellar surfaces with ligand molecules for targeted oligonucleotide delivery have been developed.<sup>17</sup> Various ligand molecules, including small molecules, peptides, and even antibodies, have been coupled to the terminus of PEG to selectively bind to specific proteins or sugars that are overexpressed on the target cellular surface. Notably, the ligand-installed micellar surface enabled multivalent binding between the micellar PIC and the target cellular surface, dramatically amplifying the binding affinity compared to single-molecular binding.<sup>18</sup>

A cyclic RGD peptide (cRGD) was introduced onto the micellar surface (or  $\alpha$ -end of the PEG segment in PEG-PLys) to actively target  $\alpha_v\beta_3$  and  $\alpha_v\beta_5$  integrins, which are overexpressed on the surface of various cancer cells and cancer-associated endothelial cells. The cRGD peptide was conjugated by thiazolidine ring formation between the formyl group in a PEG terminus and a cysteine moiety tethered to a cRGD peptide (**Figure 3A**).<sup>19</sup> The cRGD-conjugated micellar PIC, which was prepared from cRGD-conjugated PEG-PLys(IM), resulted in more efficient cellular uptake of siRNA in cultured cervical cancer cells.<sup>20</sup> When systemically administrated

into subcutaneous-cervical-cancer-bearing mice, the cRGD-conjugated micelle strongly enhanced the tumor accumulation of siRNA payloads as compared to a non-cRGD-conjugated control micelle, resulting in significant antitumor activity.<sup>20,21</sup>

An antibody fragment for human tissue factor (anti-TF Fab') was also installed at the PEG terminus of micellar PICs prepared from azide-functionalized PEG-PLys(IM) through copper-free click chemistry (**Figure 3A**). Notably, TF is overexpressed in various cancer and inflammatory tissues, such as, pancreatic cancer and cancer-surrounding fibroblasts. Thus, anti-TF Fab' is available for cancer and cancer-associated stromal targeting.<sup>22</sup> The anti-TF Fab'-conjugated micelle exhibited stronger binding to the TF-overexpressed pancreatic cancer cells in both monolayer and spheroid cultures. Furthermore, systemic administration of the anti-TF Fab'-conjugated siRNA-loaded micelle significantly suppressed the target gene expression in a subcutaneous model of the pancreatic cancer.<sup>23</sup>

Recently, a targeted PIC micelle conjugated with glucose ligands was reported to transcellularly cross the blood-brain barrier (BBB) and enter the brain parenchyma through recognition

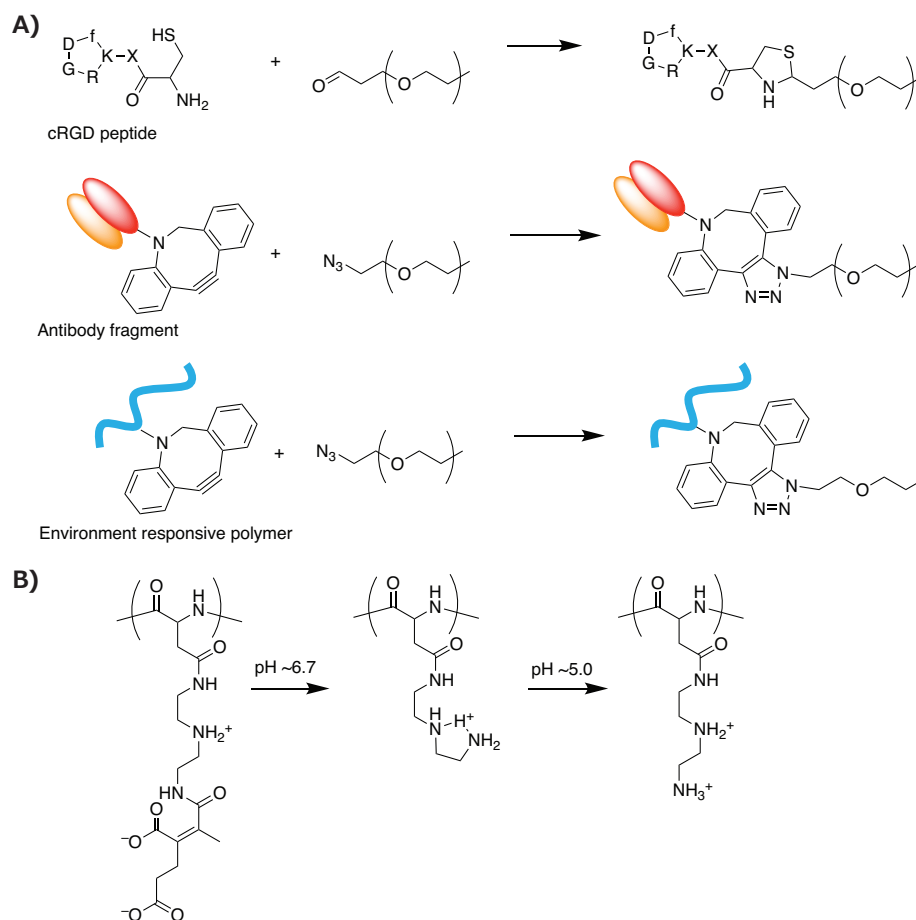


**Figure 3.** A) Synthesis scheme of modified PEG for targeting delivery of oligonucleotide. B) Change in the chemical structure of PAsp(DET-CDM) induced by biological pH change.

by glucose-transporter 1 (GLUT1), which is overexpressed on the brain capillary endothelial cellular surface.<sup>24</sup> To this end, a hetero-bifunctionalized PEG with glucose at the  $\alpha$ -end and a primary amine at the  $\omega$ -end (Glu-PEG-NH<sub>2</sub>) was synthesized by polymerization of ethylene oxide initiated at the 6-position of glucose, and the amination of the other terminus. The systemic administration of the glucose-conjugated micelle led to high PIC accumulation in brain tissue (~6% dose/g brain). This method relies on the GLUT1 recycling mechanism in the brain capillary endothelial cells, which is triggered by a glycemic control method.<sup>24</sup> This type of glucose-mediated brain targeting could be used for the systemic delivery of oligonucleotides into diseased brain or glioblastoma.

The biological-environment-responsive functionalization of PEG-PLys was combined with surface modification of micellar PICs to respond to the slightly acidic tumor microenvironment and more acidic endosomal compartment. To this end, a zwitterionic polyaspartamide derivative (PAsp(DET-CDM)) was synthesized from diethylenetriamine (DET) and carboxydimethyl maleate (CDM) to alter the chemical (or protonated) structure in a stepwise manner according to a biological pH change.<sup>25</sup> Specifically, the CDM moieties were detached from the backbone in response to a slightly acidic tumor microenvironment (pH  $\approx$  6.7). In addition, the DET moieties moved from the monoprotonated state to the diprotonated state in an acidic late endosomal compartment (pH  $\approx$  5.0) (Figure 3B). On the basis of this structural change, a PAsp(DET-CDM)-conjugated micellar PIC, which was prepared via copper-free click conjugation, elicited a substantial change in the surface potential from a negative value at pH 7.4, to a modestly positive value at pH  $\sim$ 6.7, for interaction with the negatively charged cellular membrane in tumor tissues. At pH  $\sim$ 5.0, the surface potential exhibited a highly positive value which destabilize the endosomal membrane in the cancer cells. Compared with a nonconjugated control micelle, the PAsp(DET-CDM)-conjugated micelle induced efficient gene silencing in cultured lung cancer cells, especially under cell culture condition of pH 6.7.<sup>25</sup>

## Summary

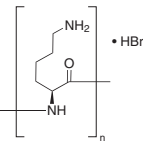
This review described oligonucleotide-loaded PICs prepared from PEG-PLys with or without chemical modifications. The micellar PICs exhibit various functionalities according to their specific chemical modifications, and some of the micellar PICs have demonstrated substantial therapeutic effects in murine cancer models by delivering siRNAs and ASOs that target cancer-related genes. Despite this success *in vivo*, clinical trials for polymeric oligonucleotide delivery systems remain rare. The current hurdles for oligonucleotide therapeutics in clinical trials are typically rapid renal and liver clearance.<sup>26</sup> The stabilization of PIC micelles through chemical modifications could reduce the rate of renal clearance. The liver is considered to preferably

uptake or sequester nanoparticles with high positive/negative charges, lipophilicity, or a large particle size (>100 nm).<sup>27</sup> We predict that the rational design of polymeric materials for reversible stabilization and/or piloting modification, including both previously reported and developing techniques, will bring micellar delivery systems into clinical trials, and ultimately lead to therapeutic success.

## References

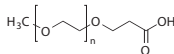
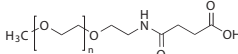
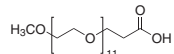
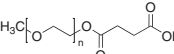
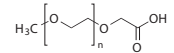
- (1) Kim, H. J.; Kim, A.; Miyata, K.; Kataoka, K. *Adv. Drug Deliv. Rev.* **2016**, *104*, 61–77.
- (2) Kaczmarek, J. C.; Kowalski, P. S.; Anderson, D. G. *Genome Med.* **2017**, *9*, 60.
- (3) Takemoto, H.; Nishiyama, N. *J. Controlled Rel.* **2017**, *267*, 90–99.
- (4) Ferreira, M. G.; Tillman, L.; Hardee, R.; Bodmeier, R. *J. Controlled Rel.* **2001**, *73*, 381–390.
- (5) Kataoka, K.; Togawa, H.; Harada, A.; Yasugi, K.; Matsumoto, T.; Katayose, S. *Macromolecules* **1996**, *29*, 8556–8557.
- (6) Kataoka, K.; Harada, A.; Nagasaki, Y. *Adv. Drug Deliv. Rev.* **2001**, *47*, 113–131.
- (7) Kakizawa, Y.; Kataoka, K. *Adv. Drug Deliv. Rev.* **2002**, *54*, 203–222.
- (8) Hayashi, K.; Chaya, H.; Fukushima, S.; Watanabe, S.; Takemoto, H.; Osada, K.; Nishiyama, N.; Miyata, K.; Kataoka, K. *Macromol. Rapid Commun.* **2016**, *37*, 486–493.
- (9) Watanabe, S.; Hayashi, K.; Toh, K.; Kim, H. J.; Liu, X.; Chaya, H.; Fukushima, S.; Katsushima, K.; Kondo, Y.; Uchida, S.; Ogura, S.; Nomoto, T.; Takemoto, H.; Cabral, H.; Kinoh, H.; Tanaka, H. Y.; Kano, M. R.; Matsumoto, Y.; Fukuhara, H.; Uchida, S.; Nangaku, M.; Osada, K.; Nishiyama, N.; Miyata, K.; Kataoka, K. *Nat. Commun.* **2019**, *10*, 1894.
- (10) Choi, H. S.; Liu, W.; Misra, P.; Tanaka, E.; Zimmer, J. P.; Ipe, I.; Bawendi, M. G.; Frangioni, J. V. *Nat. Biotechnol.* **2007**, *25*, 1165–1170.
- (11) Kakizawa, Y.; Harada, A.; Kataoka, K. *J. Am. Chem. Soc.* **1999**, *121*, 11247–11248.
- (12) Kakizawa, Y.; Harada, A.; Kataoka, K. *Biomacromolecules* **2001**, *2*, 491–497.
- (13) Miyata, K.; Kakizawa, Y.; Nishiyama, N.; Harada, A.; Yamasaki, Y.; Koyama, H.; Kataoka, K. *J. Am. Chem. Soc.* **2004**, *126*, 2355–2361.
- (14) Christie, R. J.; Miyata, K.; Matsumoto, Y.; Nomoto, T.; Menasco, D.; Lai, T. C.; Pennisi, M.; Osada, K.; Fukushima, S.; Nishiyama, N.; Yamasaki, Y.; Kataoka, K. *Biomacromolecules* **2011**, *12*, 3174–3185.
- (15) Springsteen, G.; Wang, B. *Tetrahedron* **2002**, *58*, 5291–5300.
- (16) Naito, M.; Ishii, T.; Matsumoto, A.; Miyata, K.; Miyahara, Y.; Kataoka, K. *Angew. Chem. Int. Ed.* **2012**, *51*, 10751–10755.
- (17) Cabral, H.; Miyata, K.; Osada, K.; Kataoka, K. *Chem. Rev.* **2018**, *118*, 6844–6892.
- (18) Mammen, M.; Choi, S. K.; Whitesides, G. M. *Angew. Chem. Int. Ed.* **1998**, *37*, 2754–2794.
- (19) Oba, M.; Fukushima, S.; Kanayama, N.; Aoyagi, K.; Nishiyama, N.; Koyama, K.; Kataoka, K. *Bioconjugate Chem.* **2007**, *18*, 1415–1423.
- (20) Christie, R. J.; Matsumoto, Y.; Miyata, K.; Nomoto, T.; Fukushima, S.; Osada, K.; Halnaut, J.; Pittella, F.; Kim, H. J.; Nishiyama, N.; Kataoka, K. *ACS Nano* **2012**, *6*, 5174–5189.
- (21) Nishida, H.; Matsumoto, Y.; Kawana, K.; Christie, R. J.; Naito, M.; Kim, B. S.; Toh, K.; Min, H. S.; Yu, Y.; Matsumoto, Y.; Kim, H. J.; Miyata, K.; Taguchi, A.; Tomio, K.; Yamashita, A.; Inoue, T.; Nakamura, H.; Fujimoto, A.; Sato, M.; Yoshida, M.; Adachi, K.; Arimoto, T.; Wada-Hiraike, O.; Oda, K.; Nagamatsu, T.; Nishiyama, N.; Kataoka, K.; Osuga, Y.; Fujii, T. *J. Controlled Rel.* **2016**, *231*, 29–37.
- (22) van den Berg, Y. W.; Osanto, S.; Reisma, P.; Versteeg, H. H. *Blood* **2012**, *119*, 924–932.
- (23) Min, H. S.; Kim, H. J.; Ahn, J.; Naito, M.; Hayashi, K.; Toh, K.; Kim, B. S.; Matsumura, Y.; Kwon, I. C.; Miyata, K.; Kataoka, K. *Biomacromolecules* **2018**, *19*, 2320–2329.
- (24) Anraku, Y.; Kuwahara, H.; Fukusato, Y.; Mizoguchi, A.; Ishii, T.; Nitta, K.; Matsumoto, Y.; Toh, K.; Miyata, K.; Uchida, S.; Nishina, K.; Osada, K.; Itaka, K.; Nishiyama, N.; Mizusawa, H.; Yamasoba, T.; Yokota, T.; Kataoka, K. *Nat. Commun.* **2017**, *8*, 1001.
- (25) Tangsangskri, M.; Takemoto, H.; Naito, M.; Maeda, Y.; Sueyoshi, D.; Kim, H. J.; Miura, Y.; Ahn, J.; Azuma, R.; Nishiyama, N.; Miyata, K.; Kataoka, K. *Biomacromolecules* **2016**, *17*, 246–255.
- (26) Levin, A. A. *New Eng. J. Med.* **2019**, *380*, 57–70.
- (27) Zhang, Y. N.; Poon, W.; Tavares, A. J.; McGilvray, I. D.; Chen, W. C. W. *J. Controlled Rel.* **2016**, *240*, 332–348.

## Poly(L-lysine)

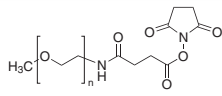
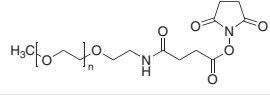
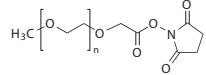
Name	Structure	Avg. $M_n$ (Da)	Cat. No.
Poly-L-lysine hydrobromide		-	L8295-5G
		1,000-5,000	P0879-25MG P0879-100MG P0879-500MG P0879-1G
		4,000-15,000 by viscosity ≤15,000 by MALLS	P6516-25MG P6516-100MG P6516-500MG P6516-1G
		15,000-30,000 by viscosity	P7890-25MG P7890-100MG P7890-500MG P7890-1G
		30,000-70,000	P2636-25MG P2636-100MG P2636-500MG P2636-1G
		40,000-60,000	P3995-1G
		70,000-150,000 by viscosity	P1274-25MG P1274-100MG P1274-500MG P1274-1G
		150,000-300,000	P1399-25MG P1399-100MG P1399-500MG P1399-1G
		≥300,000	P1524-25MG P1524-100MG P1524-500MG P1524-1G

## Poly(ethylene glycol)

## Carboxylic Acid Functionalized PEG

Name	Structure	Avg. $M_n$ (Da)	Cat. No.
Methoxypolyethylene glycol 5,000 propionic acid		-	88908-1G-F 88908-5G-F
O-[2-(3-Succinylamino)ethyl]-O'-methyl-polyethylene glycol		PEG average $M_n$ 20,000	21954-1G
O-(2-Carboxyethyl)-O'-methyl-undecaethylene glycol		-	689556-250MG
O-Methyl-O'-succinylpolyethylene glycol 5'000		$M_n$ ~5100	17929-1G-F 17929-5G-F
Methoxypolyethylene glycol 5,000 acetic acid		-	70718-1G-F 70718-5G-F 70718-25G-F

## NHS Ester Functionalized PEG

Name	Structure	Avg. $M_n$ (Da)	Cat. No.
O-[(N-Succinimidyl)succinyl-aminoethyl]-O'-methylpolyethylene glycol		average $M_n$ 750	712531-250MG
O-[(N-Succinimidyl)succinyl-aminoethyl]-O'-methylpolyethylene glycol 2'000		2,000	41214-1G-F
Methoxypolyethylene glycol 5,000 acetic acid N-succinimidyl ester		PEG average $M_n$ 5,000	85973-1G

## Azide Functionalized PEG

Name	Structure	Avg. $M_n$ (Da)	Cat. No.
Methoxypolyethylene glycol azide		PEG average $M_n$ 20,000	726176-250MG
mPEG12-Azide		average $M_n$ 12,000	JKA13019-500MG
mPEG5-Azide		average $M_n$ 5,000	JKA13016-500MG
mPEG6-Azide		average $M_n$ 6,000	JKA13017-500MG
mPEG7-Azide		average $M_n$ 7,000	JKA13018-500MG
O-(2-Azidoethyl)-O'-methyl-triethylene glycol		average $M_n$ 200	712590-100MG
O-(2-Azidoethyl)-O'-methyl-undecaethylene glycol		-	712604-100MG
O-(2-Azidoethyl)nonadecaethylene glycol		-	726249-250MG
Poly(ethylene glycol) methyl ether azide		PEG average $M_n$ 350 ( $n \sim 8$ ) average $M_n$ 400	767557-1ML
		PEG average $M_n$ 1,000	733407-1G
Methoxypolyethylene glycol azide		PEG average $M_n$ 10,000	726168-250MG

## Aldehyde Functionalized PEG

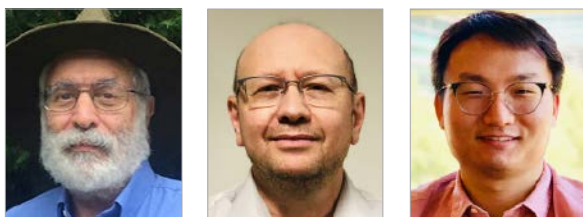
Name	Structure	Avg. $M_n$ (Da)	Cat. No.
O-[2-(6-Oxocaproylamino)ethyl]-O'-methylpolyethylene glycol 5'000		5,000	41964-250MG-F 41964-1G-F
O-[2-(6-Oxocaproylamino)ethyl]-O'-methylpolyethylene glycol 2'000		2,000	54369-250MG-F

## Building Blocks for Poly(L-lysine) Modification

Name	Structure	Purity	Cat. No.
Dimethyl 3,3'-dithiopropionimidate dihydrochloride		-	D2388-100MG
2-Iminothiolane hydrochloride		≥98%, TLC	I6256-100MG I6256-500MG I6256-1G
Diethylenetriamine		99%	D93856-5ML D93856-100ML D93856-4X100ML D93856-1L D93856-2.5L D93856-18L
3-(2-Pyridyldithio)propionic acid N-hydroxysuccinimide ester		≥95%	P3415-5MG P3415-25MG P3415-100MG



# Applications of Glucose Polymers in the Synthesis of Diagnostic and Drug Delivery Nanoparticles



Ernest V. Groman, Dmitri Simberg, and Guankui Wang\*

Colorado Center for Nanomedicine and Nanosafety, Translational Bio-Nanosciences Laboratory, Department of Pharmaceutical Sciences, Skaggs School of Pharmacy and Pharmaceutical Sciences, University of Colorado Anschutz Medical Campus, Aurora, CO 80045, USA

\*Email: Guankui.Wang@cuanschutz.edu

## Introduction

Dextran is a polysaccharide made of many glucose molecules that was first isolated by Louis Pasteur in 1861.<sup>1</sup> Since then, dextran has found many applications in medicine including reducing blood viscosity, preventing blood clot formation, and serving as an iron-dextran nanoparticle (NP) to treat iron deficiency anemia using the carboxymethyl dextran-coated magnetite nanoparticle, Feraheme®. Clinical studies have shown that diethylaminoethyl (DEAE)-dextran can reduce cholesterol and triglyceride levels.<sup>2</sup> Research applications of dextran include its use as an alternative for PEGylation and as a stabilizer of protein structure.<sup>3</sup>

Glucose is a deceptively simple molecule until we consider its use as a building block of homopolymers. Glucans are polysaccharides derived from glucose monomers. The monomers are linked by glycosidic bonds. Four types of glucose-based polysaccharides are possible: 1,6- (starch), 1,4- (cellulose), 1,3- (laminarin), and 1,2-bonded glucans. Theoretically, since the anomeric C1 carbon of glucose can have an up or down configuration, we can multiply the 4 listed glucans by 2. Further, cyclic polyglucose compounds called cyclodextrins add to the list of glucans.

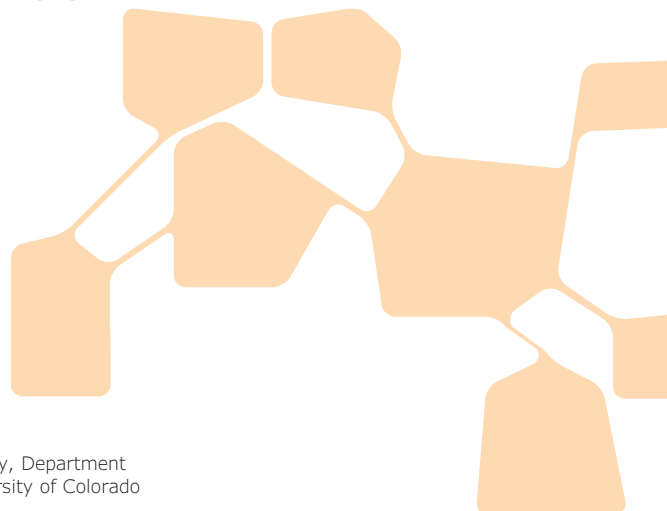
In this short review we first examine the role of dextran in forming NPs with doxorubicin and in the formation and stability of iron oxide NPs. In the second part of this review, we discuss cyclodextrin as a starting material for the preparation of NPs. In these reviews we provide methods for synthesis.

## Dextran Colloids

Dextran is widely used in the synthesis of iron oxide NPs. However, the effect of small changes in the structure of dextran upon the final colloid is not widely recognized. For instance, in an earlier article, Paul et al., found that small changes in the structure of dextran produced profound results in the synthesis of dextran-coated NPs.<sup>4</sup> The reduction of the terminal reducing sugar had a significant effect on particle size, coating stability, and magnetic properties. For low-molecular-weight dextran molecules (MW  $\leq 10$  kDa), reduction resulted in a 10-fold or greater decrease in the carbohydrate-to-iron ratio needed to produce the desired particle size (<20 nm). Particles prepared at the equivalent dextran-to-iron ratio using the equivalent native dextran yielded larger particles. Furthermore, the stability of particle size and coating using 10 kDa native and reduced dextran yielded a colloid that was stable to autoclaving.

**Reduced Dextran T10.** Dextran T10 (10 g) was dissolved in 100 mL of deionized water at 25 °C to which 1 g of sodium borohydride was added, and the mixture was stirred 12 h. The pH was brought to 5.0 using 6 M HCl. The mixture was ultrafiltered against a 3 kDa membrane. The product was lyophilized to produce a white solid in 63% yield. HPLC retention times (min): reduced dextran) 21.6; native dextran) 21.1.

**Preparation of Native and Reduced Dextran T10- Coated Particles.** Native or reduced dextran T10 (2.7 g) was dissolved in 70 mL of deionized water. A mixture of 2.0 g of ferric chloride hexahydrate and 1.0 g of ferrous chloride tetrahydrate dissolved



in 27 g of deionized water was added. The mixture was purged with nitrogen for 30 min and cooled to 5 °C, and 8.5 g of ammonium hydroxide (28%) added with stirring over 2 min. The mixture was heated at 80 °C for 2 h and purified through six cycles of ultrafiltration against deionized water using a 100 kDa membrane. After ultrafiltration, the reduced dextran particles were 0.2 µm filtered and stored at 4 °C.

Feraheme (ferumoxytol) is one of the few dextran-coated NPs that has been approved by the FDA and is indicated for treating anemia. The iron in Feraheme is found in the form of magnetite encapsulated in a dextran coat. The dextran that covers the magnetic core of Feraheme is both reduced and modified with carboxymethyl groups, providing the technological advance that contributed to its approval by the FDA.

The exact details of the synthesis of Feraheme is a trade secret. However, Feraheme is protected by US patents 6599498, 7048907, 7553479, 8501158, 8926947, and 9555133. For those who are interested, a close reading of these patents can provide an understanding of the art and science of making dextran-coated colloids.

Besides iron supplement application, Feraheme has also been widely used as a T2 contrast agent for magnetic resonance imaging (MRI) in both basic research and clinical trials. After intravenous injection, Feraheme is internalized by macrophages. While Kupffer cells in the liver are the primary means of internalization, other tissues such as spleen, lymph nodes, or tumor sites have also been shown to internalize Feraheme.<sup>5</sup> Studies have identified Feraheme as a potential diagnostic contrast agent to detect inflammation sites and tumors, monitor treatment after brain surgery and map out metastatic lymph nodes for certain cancers using MRI.<sup>6</sup>

Wasiak et al. present an alternative method for synthesis of dextran-based colloids using multiple steps beginning with the oxidation of dextran yielding multiple aldehyde groups.<sup>7</sup> In their example the aldehydes are reacted with doxorubicin and hydrophobic amines referred to as coiling agents. The procedure is described below.

**Synthesis of polyaldehydodextran (PAD).** The dextran (10 g) was dissolved in 200 ml distilled water and sodium periodate followed by the addition of sodium metaperiodate. After stirring in the dark at room temperature for 1 h ethylene glycol was added to quench the oxidation by periodate. The solution was dialyzed against distilled water and dried at 50 °C.

**Synthesis of dextran nanoparticles (Dex-NPs) and with doxorubicin (Dox-NPs).** Dried PAD (1 g) was dissolved in 10 ml of water (30 °C) and combined with 0.01 g/ml of doxorubicin aqueous solution. Five minutes later coiling agent (hexylamine, octylamine, dodecylamine, or benzylamine) was added, and the mixture was stirred for 30 min at 30 °C. The pH was increased to pH 10 with 0.5 M sodium hydroxide within 60 min. The pH of the mixture was decreased to 7.4 and the Dex-NPs were dialyzed against water. Dex-NPs were lyophilized using dextran as a cryoprotectant. The schematic representation of the NP synthesis is presented on **Figure 1A**.

**Synthesis of dextran nanoparticles with reduced bonds (rDox-NPs).** Bonds between dextran aldehyde groups and amine groups of doxorubicin were reduced with NaBH<sub>4</sub>. The pH of the mixture was brought to 7.4 and rDox-NPs were dialyzed against distilled water for 24 h (**Figure 1B**). Reduction binds doxorubicin covalently to form rDox-NPs. The rDox-NPs were used for the calculation of the drug encapsulation efficiency.

### Cyclodextrin-Based Nanoparticles

Cyclodextrins consist of a macrocyclic ring of glucose subunits joined by  $\alpha$ -1,4 glycosidic bonds (**Figure 2A**). They find applications in food preparation, pharmaceutical formulation, and drug delivery as well as chemical, industrial, agricultural, and environmental applications.<sup>3</sup> Cyclodextrins are known to the general public since they are commonly used in products designed to control odors in the home. Cyclodextrins can be expensive, but industrial and consumer usage has reduced prices to a range acceptable to academic laboratories. Cyclodextrin are all considered GRAS, or generally recognized as safe, by the U.S. FDA.<sup>8</sup>

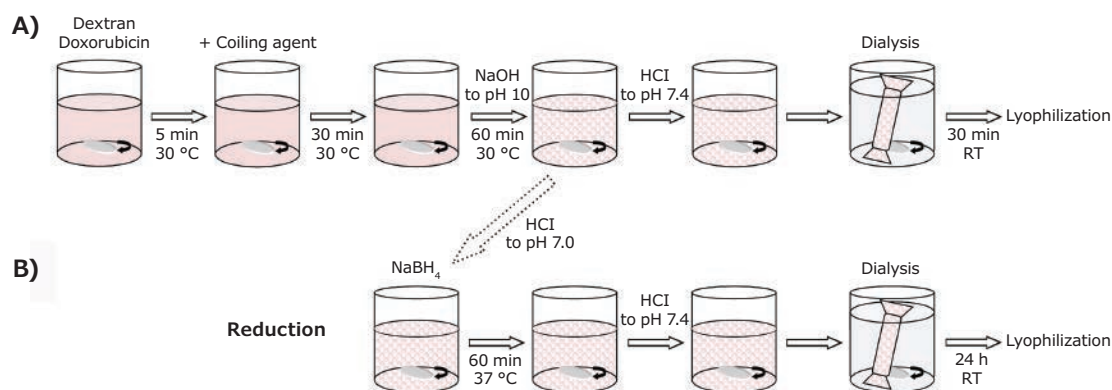


**Figure 1.** Diagram of Nanoparticle Synthesis Strategy using Dextran.

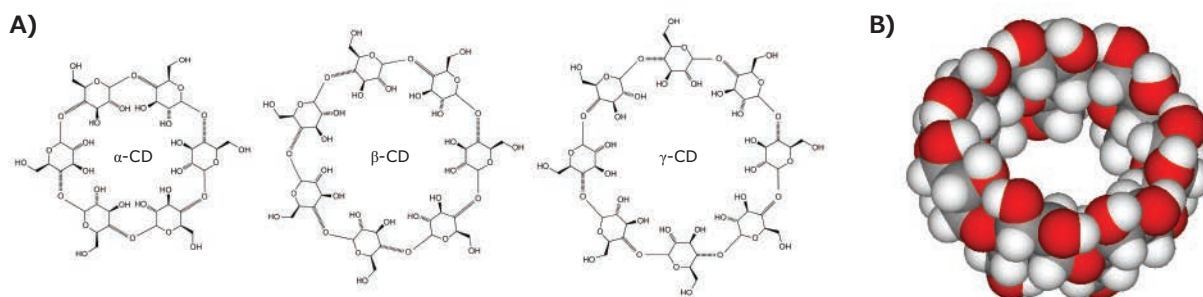


**Figure 2.** A) The three most common cyclodextrins; B) a space-filling model of  $\beta$ -cyclodextrin.

Cyclodextrins bind hydrophobic molecules in the center of the ring (Figure 2B). With a hydrophobic interior and hydrophilic exterior, cyclodextrins form complexes with hydrophobic compounds conferring solubility and stability to hydrophobic compounds. Cyclodextrins form inclusion compounds with hydrophobic molecules, enabling them to penetrate body tissues. The mechanism of ligand release is related to a variety of factors including pH, ionic strength, solvent polarity, temperature, and enzymatic degradation of the ligand and/or cyclodextrin.<sup>3</sup>

### Illustration of Cyclodextrin NPs from the Patent Literature

The affinity/avidity constant between cyclodextrin and bound ligand can be increased considerably by polymerizing cyclodextrin into an NP. This section considers several approaches to the polymerization of cyclodextrins based on the patent and peer-reviewed literature. Examples of forming cyclodextrin NPs from the patent literature are noted for their simplicity and scale, reflecting industrial applications.

Water-insoluble cyclodextrin polymers are produced by polymerizing cyclodextrins with crosslinking agents. Generally, epichlorohydrin or diepoxy derivatives (e.g. diepoxy butane, diepoxypropyl ether, ethylene glycol diepoxypropyl ether) are used as cross-linking agents, with the polymer being produced either by block polymerization (U.S. Patent 3472835), as regular pearls (GB patent 1244990) or as foamed polymerizates (Hungarian patent application 1188/81). The mechanical properties of these rigid materials can be improved significantly by incorporating polyvinyl alcohol (U.S. Patent 4274985) with the crosslinking reagent. This is important when using cyclodextrin polymers as stationary phase in column chromatography.

When using cyclodextrin polymers as stationary phase in chromatography, important attributes are related to the water-absorbing capacity and rate of water absorption. The water-absorbing capacity of the final product is greater when more cross-linking agents or more dilute cyclodextrin solutions are used. An example of the synthesis of a rapid swelling cyclodextrin polymer is found in US Patent 4547572.

In 10 ml of water (60 °C), dissolve 3.0 g NaOH, 5.0 g  $\beta$ -cyclodextrin and then add 2.5 ml of tetraethylene glycol and 5.7 ml of epichlorohydrin. Continue heating for 1.5 hours at 60 °C. The cooled gel is washed salt-free with water, dehydrated with acetone, dried at 105 °C and pulverized. After this process is complete, 6.8 g of a white powdery material are obtained with a cyclodextrin content of 50.6%.

It is desirable to form beads to facilitate flow during chromatography. One example (U.S. Patent 4726905) uses polycyclodextrin beads to remove polychlorinated biphenyl compounds from the environment. US Patent 5075432 illustrates an improved method for forming cyclodextrin polymer beads.

In a 3-liter reaction vessel equipped with a stirrer blade, add 2 liters (1,540 g) of methyl isobutyl ketone (MIBK) and heat to 80 °C. The top of the reaction vessel is covered with a condenser and the stirring blade is run at 300 rpm. To this reaction vessel, add 6 g of polyvinyl butyral (hydroxyl content of about 19% and a molecular weight of about 125,000) and stir until dissolved. In another vessel, a slurry is prepared by mixing 49 g of  $\beta$ -cyclodextrin, 54.5 g of water and 87.3 g of a 30% NaOH solution. The stirring is continued until the solution is murky but transparent. Then, the cyclodextrin slurry is added to the reaction vessel containing the MIBK and polyvinyl butyral. After 5 minutes of stirring, add 136 g of epichlorohydrin and continue stirring at 300 rpm. During the reaction, the temperature is maintained to 80 °C. After 4 hours the particles are recovered and washed. The particle diameter ranged from 30 to 170 nm.

Our last example from the patent literature of forming cyclodextrin polymers (US Patent 7745558) illustrates that polymerizations can be performed at room temperature in contrast to the previous two examples where polymerization occurred at 80 °C.

$\beta$ -cyclodextrin (2.5 g) is dissolved in a NaOH solution (2.5 g / 7.5 ml). Epichlorohydrin (4.4 ml) is gradually added to the solution over 20 minutes. The mixture is stirred at room temperature for 4 hours. The resultant polymer in a gel state is immersed in a 0.3 M  $\text{CaCl}_2$  solution to be cured. The cured polymer is washed with water and ethanol, dried at 70 °C and pulverized.  $\beta$ -cyclodextrin polymers have an average particle diameter of 200 nm.

## Illustration of Cyclodextrin NPs from Peer Reviewed Literature

Please note that for the two peer reviewed reports presented below, the scale and complexity of synthesis are considerably smaller and more complex, respectively, than that found in the patent literature. The sheer complexity of peer reviewed papers in this discipline is reflected in the number of authors and laboratories involved in a single manuscript, indicating the new reality that a variety of technical specialists are required to accomplish particular tasks and resulting in funding agencies expressing interest in supporting collaboration.

In our first peer reviewed example, Kim et al. sought to improve the detection of tumor-associated macrophages (TAMs), which are widely implicated in cancer progression.<sup>9</sup> Since it is difficult to quantify total TAM numbers and their dynamic distribution in a non-invasive manner, they developed a <sup>64</sup>Cu-labeled polyglucose NP for PET imaging which they named Macrin. A simplified summary of their very complex synthesis is presented below and illustrated in **Figure 3**.

**Macrin-NP.** Carboxymethylated polyglucose was activated with EDC and NHS in MES buffer. L-Lysine was added. The reaction mixture was added to ethanol and a white pellet was collected. The pellet was dissolved in H<sub>2</sub>O, filtered dialyzed. Macrin nanoparticle (Macrin-NP) was filtered and lyophilized to give off-white solid particles.

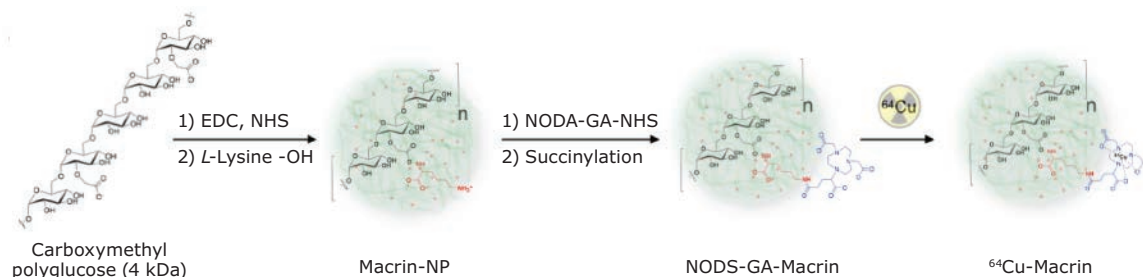


**Figure 3.** Macrin synthetic scheme.

NODA-GA-Macrin. Macrin-NP was dissolved in H<sub>2</sub>O, mixed with NODA-GA-NHS and reacted with succinic anhydride. The crude mixture was purified by dialysis and lyophilized. The hydrodynamic diameter of the NODA-GA-Macrin-NP was 20nm. The NODA-GA-Macrin-NP was ready to be charged with <sup>64</sup>Cu and drug.

In another report, cyclodextrin is conjugated with penynyl chloride and then crosslinked with epichlorohydrin in the presence of a 4 μm sized silica particle (**Figure 4**).<sup>10</sup> The suggested use of the micron sized particle is for water purification. The authors suggest introduction of pentynyl ligands improves the capturing efficiency of the hybrid material. The scale of this reaction is 5 grams.

**PyβCD.** β-cyclodextrin is dissolved in N,N-Dimethylformamide followed by the addition of Li-dimsyl. Pentynyl chloride is added and stirred at room temperature for 24 h (**Figure 4**). After the solvent is removed, the residue is suspended in water and precipitated in acetone. The product was recrystallized and dried.

**Poly-PyβCD.** PyβCD (2 g) is added to 40 ml of water followed by the addition of 6.8 ml of the 20% NaOH. The mixture is stirred at 60 °C. Silica particles (2 g) are added, and 162.84 mg of epichlorohydrin is added and stirred at 60 °C. The product is washed and dried. For comparison, β-cyclodextrin and PyβCD were polymerized without silica particles following the same procedure as described above and precipitated in acetone (**Figure 4**).

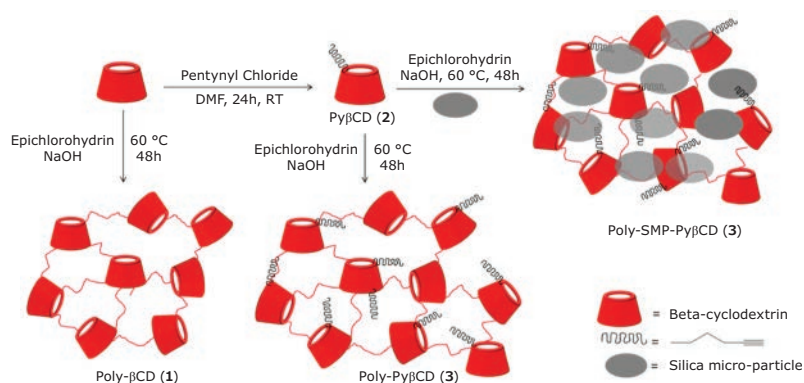


**Figure 4.** Scheme for the synthesis of β-cyclodextrin polymer (Poly-βCD, 1), pentynyl ether of βCD (PyβCD, 2), polymer of PyβCD (Poly-PyβCD, 3), and hybridization with SMP (Poly-SMP- PyβCD, 4).

## Summary

In this review, we briefly discuss the applications of two categories of glucose polymers used in the synthesis of nanoparticles: dextran and cyclodextrin. Dextran-coated iron oxide nanoparticles are clinically approved for treating anemia and are being investigated for use in conducting MRI of specific organs and tissues. Both dextran and cyclodextrin polymers have been used to deliver therapeutics and diagnostic agents in either nanoparticle or microparticle forms. These glucose polymers hold great promise for synthesis of novel biomaterials in the pre-clinical and clinical applications.

## References

- (1) Pasteur, L. *Bull Soc Chim.* **1861**, *11*, 30–31.
- (2) Alhareth, K.; Vauthier, C.; Bourasset, F.; Gueutin, C.; Ponchel, G.; Moussa, F. *Eur. J. Pharm. Biopharm.* **2012**, *81*, 453–457.
- (3) Wimmer T. (2003). Cyclodextrins. Ullmann's Encyclopedia of Industrial Chemistry. Wiley-VCH. doi:10.1002/14356007.e08\_e02. ISBN 978-3527306732.
- (4) Paul, K. G.; Frigo, T. B.; Groman, J. Y.; Groman, E. V. *Bioconjugate Chem.* **2004**, *15* (2), 394–401.
- (5) Vallabani, S. N. V.; Singh, S. *Biotech* **2018**, *8*, 279.
- (6) Toth G. et al. *Kidney Int.* **2017**, *92* (1), 47–66.
- (7) Wasiak, I.; Kulikowska, A.; Janczewska, M.; Michalak, M.; Cymerman, I. A.; Nagalski, A.; Kallinger, P.; Szymanski, W.W.; Ciach, T. *PLOS ONE* **2016**, *11* (1), DOI:10.1371/journal.pone.0146237.
- (8) GRAS Notice No. GRN 000155, alpha-cyclodextrin; GRAS Notice No. GRN 000074, beta-cyclodextrin; GRAS Notice No. GRN 000046, gamma-cyclodextrin.
- (9) Kim, H.Y.; Li, R.; Ng, T. S. C. *ACS Nano* **2018**, *12* (12), 12015–12029.
- (10) Choi, J.M.; Jeong, D.; Cho, E.; Yu, J.H.; Tahir, M. H.; Jung, S. *Polymers* **2017**, *9*, 10.

## Glucose Polymers

### Dextran

Name	Molecular Weight	Cat. No.
Dextran from <i>Leuconostoc</i> spp.	$M_n$ ~6,000	31388-25G 31388-100G 31388-500G
	$M_n$ ~100,000	09184-10G-F 09184-50G-F 09184-250G-F
Dextran from <i>Leuconostoc mesenteroides</i>	average mol wt 15,000-30,000	D4626-1KG
Dextran from <i>Leuconostoc</i> spp.	$M_n$ 15,000-25,000	31387-25G 31387-100G 31387-500G

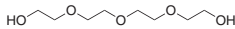
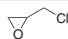
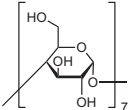
### Maltodextrin

Name	Dextrose Equivalent	Cat. No.
Maltodextrin	4.0-7.0	419672-100G 419672-500G
	13.0-17.0	419680-100G 419680-500G
	16.5-19.5	419699-100G 419699-500G

### $\beta$ -Cyclodextrin Polymer

Name	Molecular Weight	Cat. No.
$\beta$ -Cyclodextrin polymer	average mol wt 2,000-300,000 Da	C2485-1G C2485-5G

## Building Blocks

Name	Structure	Purity	Cat. No.
Iron(II) chloride tetrahydrate	$\text{FeCl}_2 \cdot 4\text{H}_2\text{O}$	99.99% trace metals basis	380024-5G 380024-25G
Tetraethylene glycol		99%	110175-100G 110175-1KG 110175-3KG 110175-20KG
( $\pm$ )-Epichlorohydrin		$\geq 99\%$ , GC	45340-500ML-F 45340-1L-F 45340-2.5L-F 45340-200L-KL-F 45340-400L-KL-F 45340-850L-DW-F
$\beta$ -Cyclodextrin		$\geq 97\%$	C4767-25G C4767-100G C4767-500G



# Polymers with possibilities

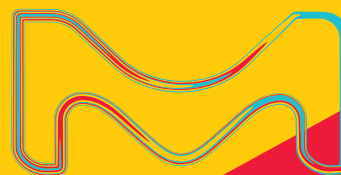
## Functionalized Poly(ethylene glycol)s for Drug Delivery

### Polymer of choice for optimal and reproducible results.

When it comes to drug delivery technologies and solutions, poly(ethylene glycol)s or PEGs are the polymer of choice for optimal and reproducible results. With excellent pharmacokinetic properties, they are ideal materials for bioconjugation, pegylation, crosslinking, and hydrogel formation.

Let us help you transform your work into new therapeutic discoveries with our diverse PEG selection.

For a complete list of available materials, visit:  
**[SigmaAldrich.com/PEG](https://www.sigmaaldrich.com/PEG)**



© 2019 Merck KGaA, Darmstadt, Germany and/or its affiliates. All Rights Reserved. MilliporeSigma, Sigma-Aldrich, Material Matters and the vibrant M are trademarks of Merck KGaA, Darmstadt, Germany or its affiliates. All other trademarks are the property of their respective owners. Detailed information on trademarks is available via publicly accessible resources. All other trademarks are the property of their respective owners. Lit. No. MS\_BR4369EN 2019 - 000000 11/2019

The life science  
business of Merck  
KGaA, Darmstadt,  
Germany operates as  
MilliporeSigma in the  
U.S. and Canada.

**Sigma-Aldrich**<sup>®</sup>  
Lab & Production Materials